

Long-term measurements of mesospheric and lower thermospheric winds using specular meteor radars

Kumulative Dissertation
zur
Erlangung des akademischen Grades
doctor rerum naturalium (Dr. rer. nat.)
der Mathematisch-Naturwissenschaftlichen Fakultät
der Universität Rostock

**Universität
Rostock**



Traditio et Innovatio

vorgelegt von
Sven Wilhelm, geb. am 09.03.1982 in Berlin, Deutschland
Rostock, 20. Juni 2019



Long-term measurements of mesospheric and lower thermospheric winds using specular meteor radars

von
Sven Wilhelm
geb. am 09.03.1982 in Berlin, Deutschland

Dieser Forschungsbericht wurde als Dissertation von der
Mathematisch-Naturwissenschaftlichen Fakultät der Universität Rostock
angenommen.

Betreuer: Prof. Dr. J. L. Chau
Leibniz-Institut für Atmosphärenphysik an der Universität Rostock

Gutachter: Prof. Dr. J. L. Chau
Leibniz-Institut für Atmosphärenphysik an der Universität Rostock
Prof. Dr. C. von Savigny
Universität Greifswald

eingereicht am: 20. Juni 2019
verteidigt am: 15. November 2019

Abstract

Long-term measurements of winds in the mesosphere and lower thermosphere are of fundamental importance to detect global circulation patterns and their effects on the entire atmosphere. However, measurements of winds and atmospheric waves seem to depend on the used instrument and the applied method to infer a decompose of the observed time series. Furthermore, differences in the measurements occur due to the observed location, the season, and the altitude range. The aim of this thesis is a study of horizontal winds and their oscillations at the middle and polar latitudes, in view of their long-term change. Primarily, meteor radars are used for the determination of the winds, which have the advantage to operate independently of the solar radiation and the weather. The resulting winds are determined with the same wind estimation approach, which promises consistency between the measurements. In addition to the investigation of long-term changes, a comparison of the winds of two different radars, as well as a possible connection between the zonal wind and a change in the atmospheric density, is analyzed.

Zusammenfassung

Langzeitmessungen von Winden in der Mesosphäre und unteren Thermosphäre sind von fundamentaler Bedeutung, um globale Zirkulationsmuster und deren Auswirkungen auf die gesamte Atmosphäre zu erkennen. Messungen von Winden und atmosphärische Wellen variieren jedoch stark, je nach dem verwendeten Messinstrument, sowie der generellen Berechnungsmethode. Ferner können auch Unterschiede in den Messungen aufgrund des Beobachtungsortes, der Jahreszeit, sowie dem Höhenbereich auftreten. Das Ziel dieser Arbeit ist eine Studie von horizontalen Winden und deren Oszillationen in mittleren und polaren geografischen Breiten, in Hinblick auf deren langfristige Änderung. Für die Bestimmung der Winde werden hauptsächlich Meteorradare verwendet, welche gegenüber anderen Messinstrumenten den Vorteil haben unabhängig von der Sonneneinstrahlung und dem Wetter zu operieren. Um Konsistenz zwischen den resultierenden Windmessungen zu erhalten wird bei allen Systemen die gleiche Windberechnungsmethode verwendet. Hierbei wird neben der Untersuchung langfristiger Änderungen, ein Vergleich der Winde zweier verschiedener Radargeräte, sowie eine mögliche Verbindung zwischen dem Zonalwind und einer Änderung in der atmosphärischen Dichte analysiert.

Contents

Abstract	v
Zusammenfassung	vi
1 Introduction	1
2 Theoretical principles of wind and temperature in the Earth's atmosphere	3
2.1 Neutral atmosphere	3
2.2 Atmospheric waves	7
2.3 Neutral density variations and its influence on the Earth rotation	11
3 Experimental methods	14
3.1 Instruments for wind measurements in the MLT	14
3.2 Deriving winds from atmospheric remote sensing	19
4 Objectives of the thesis	25
5 Comparison of MR winds and MF winds	27
6 Long-term MLT wind measurements	31
7 Connection between fluctuations in the neutral density and the zonal wind	36
8 Summary and outlook	40
Bibliography	42
Appendix A Wilhelm et al. (2017)	52
Appendix B Wilhelm et al. (2019a)	67
Appendix C Wilhelm et al. (2019b)	93
Acknowledgements	108
Curriculum Vitae	109

Chapter 1 Introduction

In several studies on long-term measurements, it has been reported that global climate change is the result of human activities since the mid-20th century (e.g., *Masson-Delmotte et al.*, 2018). An increase in temperature takes place in the troposphere but also shows dramatic cooling in the mesosphere and lower thermosphere (MLT). The temperature changes are caused by the increasing amount of anthropogenic released greenhouse gases. These gases, such as carbon dioxide (CO_2) or methane (CH_4) lead to a heat up in the troposphere by the absorption of infrared radiation and to a cooling effect above (e.g., *Thomas*, 1996; *Qian et al.*, 2011). Within the mesosphere, any perturbation happens faster due to an exponentially decreased density compared to the layers below, which makes the MLT to an excellent early warning system for physical and chemical future changes in the lower atmosphere. The global climate change does not only affect the temperature, it also influences the wind (e.g., *Laštovička et al.*, 2008). With the use of global climate models, forecast and backcast simulations can be made for several heights to estimate long-term changes.

However, measurements are essential to validate these models, but direct observations in the MLT are quite hard to conduct. The heights of the mesosphere are located between the maximum of aircraft flight level and the minimum range of orbital satellites. Therefore, other methods are required to get measurements for long-term periods. Millions of meteors entering the Earth's atmosphere every day and burn up as a result of collisions with air particles mostly at mesospheric heights. This corresponds to approximately a global input rate of cosmic dust particles between 5 to 300 tons per day (*Plane*, 2012). These numbers are still heavily discussed in science. Nevertheless, the plasma induced by ablating meteoroids include several information of the background atmosphere as winds and temperature in these heights with the use of radar (**radio detection and ranging**) instruments. Within this thesis, long-term measurements of winds in the mesosphere and lower thermosphere are investigated, as well as the main dynamic which influence the whole wind pattern: atmospheric tides, gravity waves, and planetary waves.

The thesis is structured as follow: Chapter 2 gives a brief overview of the thermal structure and wind pattern of the atmosphere, with a particular focus on the latter one in the MLT. Chapter 3 describes the used instruments and wind estimation procedure. The objectives of the thesis are described in Chapter 4. The Chapters 5 to 7 summarize the attached publications. Chapter 5 includes a comparison of winds obtained with the Andenes meteor radar system and the Saura medium frequency system. Both systems are located close by and provide winds in an overlapping altitude range. Chapter 6 includes long-term measurements of three different northern latitude meteor

Chapter 1 Introduction

radar systems and based on their observations climatologies and the long-term changes are estimated for horizontal winds, tides, as well as the kinetic gravity wave energies and planetary wave energies. Further, it includes an investigation of the impact of solar radiation based on an 11-year oscillation in the measurements. Subsequently, a connection of the influence of the solar radiation on the neutral density and further on the winds in the MLT is shown in Chapter 7. In the end, Chapter 8 summarizes the thesis and gives an outlook on future investigations.

Chapter 2 Theoretical principles of wind and temperature in the Earth's atmosphere

2.1 Neutral atmosphere

The Earth's atmosphere is the gaseous film around the Earth, which is divided into several layers. The classification into separate shells is made either based on the electron density and more common on the vertical temperature profile, as shown schematically for mid-latitudes in Figure 2.1. The layers regarding the temperature profile are called troposphere, stratosphere, mesosphere, thermosphere, and exosphere. The heights above the troposphere up to approximately 110 km are called middle atmosphere. Each atmospheric layer is demarcated by a boundary layer which is called with the suffix pause. Each pause denotes a reversal of the temperature gradient between two atmospheric layers. The heights of the pauses vary regarding latitude, due to various physical processes, as e.g., by the absorption of O_3 for sunlit latitudes. Also other effects influence the height of the pauses, as e.g., does gravity wave driven processes affect at high latitude the height of the stratopause (e.g., *France et al.*, 2012).

The troposphere, which contains about 85% of the atmospheric mass, ranges from the Earth's surface up to ~ 12 km. It is characterized by a temperature decrease from ~ 290 K at the Earth's surface to ~ 230 K at the summer tropopause. The temperature increases within the stratosphere (12 - 50 km) and reaches its maximum at about 50 km at the stratopause. Within the mesosphere (50 - 90 km), the temperature decreases to minimum values lower as ~ 130 K during the polar summer. This region, named mesopause, is the coldest place in the whole atmosphere and the source of regularly high-latitude observed phenomena as e.g., polar mesospheric clouds and mesospheric echoes (e.g., *Lübken et al.*, 2008). The thermosphere is the layer directly above the mesosphere in which the temperature rises due to absorption of solar radiation up to 2000K. The outer layer of the atmosphere is called exosphere and marks the transition into the space. In the thesis, dynamical processes in the mesosphere and lower thermosphere (MLT) are investigated.

An alternative classification of atmospheric layers, in the MLT for mid- and high latitudes, can be done by turbulent processes and ionization: 1. The turbopause region, which covers the heights of about 100 - 115 km, describes the transition layer

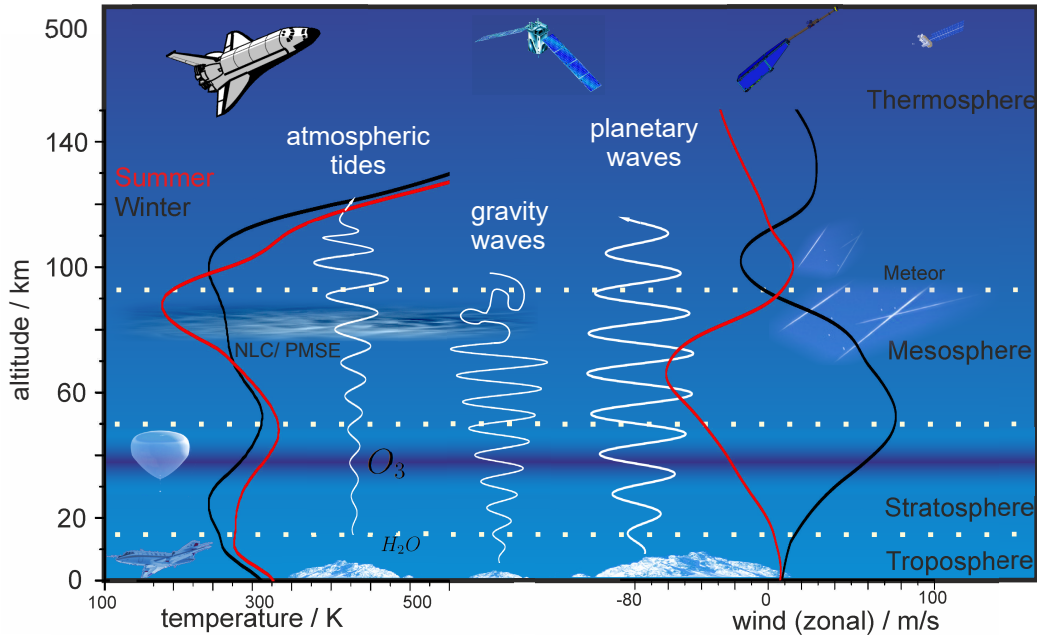


Figure 2.1 Structure of the atmosphere for the northern mid-latitudes, courtesy to G. Stober

between the well-mixed atmosphere below and heights with turbulent mixing. 2. The ionosphere is an ionized shell of electrons, electrically charged atoms and molecules created due to absorption of solar radiation. It covers the mesosphere, thermosphere, and exosphere and can be divided into three layers (D, E, F). All these layers have a similar characteristic of high concentrations of ionized particles. The lowest layer, the D layer between approximately 50 and 100 km and is the result of ionization of NO , N_2 , and O_2 by X-rays (0.1 - 1 nm). Directly above the D layer follows the E layer which covers the altitudes between 100 and approximately 150 km. Only during daylight, air parcels get ionized by extreme ultra violet radiation (80 - 103 nm) or soft X-rays (1 - 20 nm). The layer disappears nearly completely during the absence of daylight (e.g., Kelly, 2009). The F-layer covers the heights of around 150 - 800 km.

Temperature variations occur not only with height, they also change on a seasonal basis. Due to stronger solar radiation in summer higher temperatures are reached in the troposphere and stratosphere. Noticeable is the temperature profile in the mesosphere. The mesopause is $\sim 100K$ colder than the thermal equilibrium suggests (e.g., Holton, 1992; Becker, 2012). The state of a system is in thermal equilibrium if the temperature difference is balanced and in which no heat flow within the heat balance takes place. All closed systems aim for a thermal equilibrium by the exchange of heat by radiation, mass flow or heat conduction. Within the atmosphere the thermal imbalance is maintained by different radiations and heat balances on global, regional and on microscale levels. This temperature deviation in the mesopause by up to 100K is expressed in a

2.1 Neutral atmosphere

warm winter mesosphere and a cold summer mesosphere for high latitudes. A result of this temperature difference is the so called shrinking effect. A further down located mesopause is observed during the summer (~ 86 km) compared to the winter (~ 100 km) for high and mid-latitudes (e.g., *Xu et al.*, 2007; *Lübken et al.*, 2013; *Wilhelm et al.*, 2019b). As a further result, noctilucent clouds, consisting of water-ice crystals, can occur only during summer at mid- and high latitudes at heights of around 83 km as a result of a supersaturated cold atmosphere with temperatures below 150K (e.g., *Schmidt et al.*, 2018).

The phenomena of a comparable colder summer mesopause cannot purely be explained by solar radiation. Additionally, the atmospheric circulation and temperature changes due to chemical processes need to be considered, whereby the latter will not be discussed within this thesis. One theory that describes the temperature differences is the following: Under the assumption of a non-rotating Earth, the Sun lead to an imbalance in temperature with higher values at the summer pole and lower temperatures at the winter pole. Due to the large scale temperature differences in the mesosphere, high-pressure cells are formed over the summer pole and lower pressure cells over the winter pole. Consequently, pressure compensation leads to a meridional flow from the summer pole to the winter pole (e.g., *Holton and Alexander*, 2000), which can be seen in Figure 2.2. Taking the Coriolis force into account, the Earth rotation converts the meridional northward directed flow into an eastward directed wind, which leads to an eastward directed wind regime at the winter hemisphere and a westward directed wind regime at the summer hemisphere. The Coriolis force is defined by $-f_c v = \vec{\nabla} F$, where v the meridional wind and F the momentum flux and f_c is the Coriolis frequency which can further be divided into $f_c = 2\omega \sin(\theta)$, with ω the angular velocity of the Earth and the latitude θ .

Additionally, above the mesopause a vertical wind reversal occurs with westward directed wind below to eastward directed wind above a certain transition height. This wind reversal varies regarding latitude and is the result of the increasing temperature gradient in combination with the thermal wind, which describes the vertical wind shear and rotation (e.g., *Gudadze et al.*, 2019). The thermal wind is defined, according to e.g., *Holton* (1992); *Malberg* (2007); *Matthias and Ern* (2018), as the differential vector in the geostrophic wind between two pressure levels (p_0, p_1 , where $p_0 > p_1$). To derive this shear, first, the geostrophic wind components u_g and v_g , for the zonal and the meridional component, can be expressed by:

$$u_g = -\frac{1}{f_c} \frac{\partial \Phi}{\partial y} \quad (2.1)$$

$$v_g = \frac{1}{f_c} \frac{\partial \Phi}{\partial x} \quad (2.2)$$

where Φ is the geopotential. Under the use of the hydrostatic equation $dp = -g\rho dz$ and ideal gas law $p = \rho RT_v$, the thermal wind u_T, v_T between two pressure levels is received by:

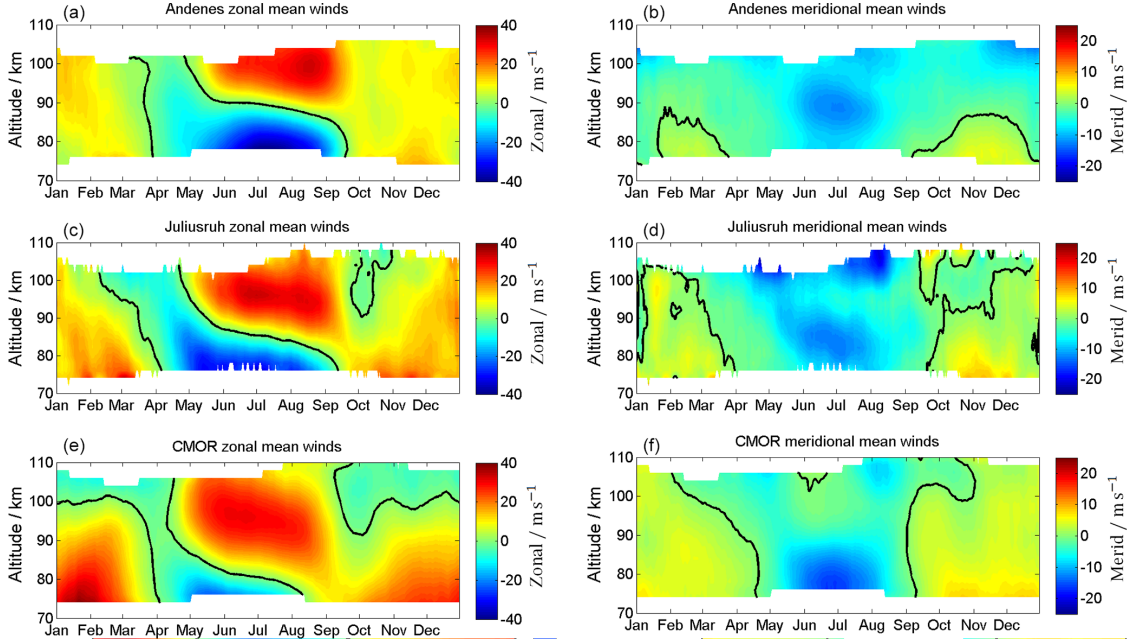


Figure 2.2 Composite of zonal (left) and meridional (right) wind component for the Andenes (top), Juliusruh (middle), and the CMOR (bottom). The black line corresponds to the wind reversal. Note the different labels of the colorbar. Figure taken from *Wilhelm et al. (2019a)*, Figure 2.

$$u_T = u_g(p_1) - u_g(p_0) = -\frac{R}{f_c} \frac{\partial \bar{T}_v}{\partial y} \ln \left(\frac{p_0}{p_1} \right) \quad (2.3)$$

$$v_T = v_g(p_1) - v_g(p_0) = \frac{R}{f_c} \frac{\partial \bar{T}_v}{\partial x} \ln \left(\frac{p_0}{p_1} \right) \quad (2.4)$$

where \bar{T}_v is the layer mean temperature between the layers (p_0 and p_1). It is shown that the change in the geostrophic wind between two pressure levels is directly related to the layer mean temperature. According to the equations 2.3 and 2.4, the meridional component of the thermal wind is a function of the zonal gradient of the layer mean temperature, and the zonal part of the thermal wind is a function of the meridional gradient of the layer mean temperature. Similarities occur in equations 2.1 and 2.2, the meridional component of the geopotential wind is a function of the zonal geopotential height gradient, and the zonal component of the geopotential wind is a function of the meridional geopotential height gradient. Summarized, a change of the meridional temperature gradient leads to a change in the zonal wind and a change in the zonal temperature gradient to a change in the meridional wind. In contrast to some models (e.g., *Fomichev et al., 2002*; *Schmidt et al., 2006*), during the winter the wind reversal for high latitudes is not visible in the meteor radar observations (Figure 2.2), which means that it most likely occurs above the maximum height of the MR observations. Beside the general circulation, short time wind fluctuations as gravity waves play an

important role for the seasonal wind and temperature pattern, which will be explained in Section 2.2.

2.2 Atmospheric waves

Winds and temperatures differences occur not only on seasonal basis, they also vary on much shorter time scales. For a full understanding of the atmospheric temperature and wind regime wave activities needs to be considered. The basic characteristics of atmospheric waves are described by the classical linear theory. Motions of waves are considered by linear perturbations on a spherical isothermal atmosphere. According to *Forbes* (1995), these are described by the basic equations for the horizontal momentum (2.5, 2.6), the conservation of energy (2.7), and the equation for continuity (2.8).

$$\frac{\partial u}{\partial t} - 2\omega \sin\theta v + \frac{1}{a \cos\theta} \frac{\partial \Phi}{\partial \phi} = 0 \quad (2.5)$$

$$\frac{\partial v}{\partial t} + 2\omega \sin\theta u + \frac{1}{a} \frac{\partial \Phi}{\partial \theta} = 0 \quad (2.6)$$

$$\frac{\partial}{\partial t} \Phi_z + N^2 w = \frac{\kappa J}{H} \quad (2.7)$$

$$\frac{1}{a \cos\theta} \left(\frac{\partial u}{\partial \phi} + \frac{\partial}{\partial \theta} (v \cos\theta) \right) + \frac{1}{\rho_0} \frac{\partial}{\partial z} (\rho_0 w) = 0 \quad (2.8)$$

where

Chapter 2 Theoretical principles of wind and temperature in the Earth's atmosphere

u	zonal velocity
v	meridional velocity
w	vertical velocity
t	time
ω	angular velocity of the Earth
θ	latitude
Φ	geopotential
λ	longitude
z	altitude
N^2	Brunt-Väisälä frequency squared
κ	$R/c_p \approx 2/7$
J	heating per unit mass
H	constant scale height
a	radius of the Earth
ρ_0	basic state density

Atmospheric waves are present in nearly all measurements as periodic perturbation of the mean flow and can be classified according to their temporal and spatial characteristics into planetary waves, tidal waves, and gravity waves. Figure 2.3 shows the separation of each of these waves for the year 2009, measured with a meteor radar.

- Large scale planetary waves are primarily the result of large scale air motions over orography, geographic land-sea differences and by baroclinic instabilities. They have global extensions and remain between 2 and 30 days in the atmosphere. Due to their restoring force, the Coriolis force, they are transporting warm air from the equator to the pole and return cold air to the equator to keep the atmosphere in balance. Furthermore, they play an important role in coupling processes between atmospheric layers (e.g., *Forbes, 1995; Holton and Alexander, 2000; Matthias et al., 2013*). Beside the global comprehensive horizontal movement, planetary waves are also able to propagate vertically under the condition of a not too strong, but prevailing, eastward directed mean wind (*Charney and Drazin, 1961*). The eastward directed mean wind prevails in the stratosphere during the winter, allowing planetary waves to propagate from the troposphere up to the mesosphere. One exception of this propagation is visible during sudden stratospheric warmings when a wind reversal towards westward directed wind takes place.
- Atmospheric tidal waves, or tides, are essential to explain dynamical coupling in

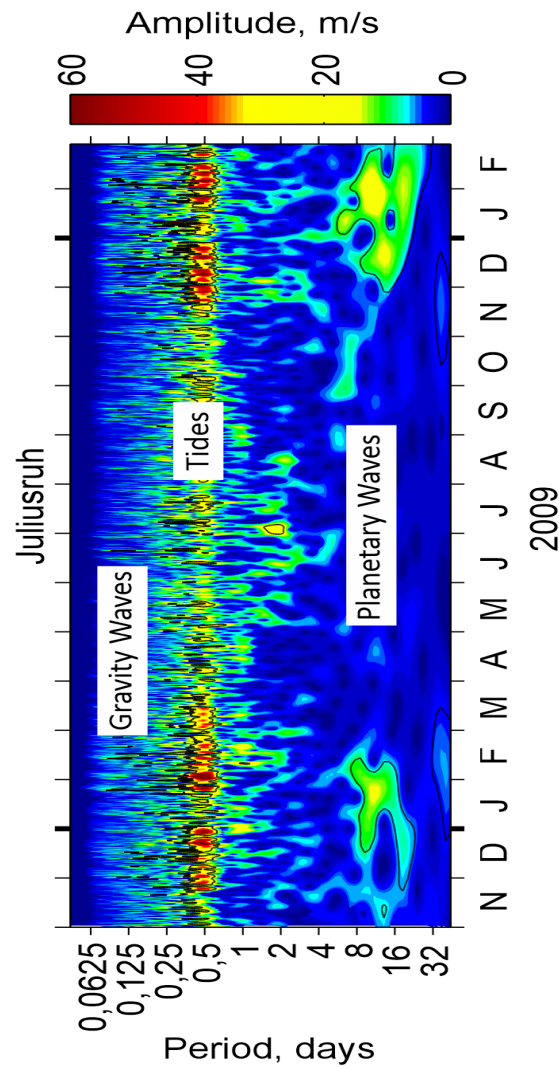


Figure 2.3 Wavelet of the zonal wind component of a meteor radar for the year 2009 for the Juliusruh, extracted planetary waves, tides and gravity waves.

the atmosphere by transporting momentum from their source region up into thermospheric heights. Tides can be distinguished into migrating and non-migrating tides. Migrating waves, which propagate synchronous to the movement of the Sun, are created due to periodic absorption of solar infrared and ultraviolet radiation by chemical components, as tropospheric water vapor, stratospheric ozone, and thermospheric Oxygen/Nitrogen (e.g., *Lindzen and Chapman, 1969*). Furthermore, they can be generated due to a release of latent heat in deep tropospheric convections (e.g., *Hagan and Forbes, 2002*).

Non-migrating or non-sun-synchronous tides are generated by several mechanisms

as longitudinal differences in the release of latent tropospheric heat or due to radiative heating (e.g., *Davis et al.*, 2013). According to *Oberheide et al.* (2002), they can further be generated by non-linear interaction between planetary waves and migrating tides.

Tides, in general, have a period of a solar day or a lunar day and their harmonics (e.g, *Fiedler and Baumgarten*, 2018). The amount of solar radiation differs regarding latitude, therefore for equatorial latitudes, the most dominant tide is the diurnal (24h) component, but at middle and high latitudes the semidiurnal (12h) components are more pronounced (*Lindzen and Chapman*, 1969; *Hoffmann et al.*, 2010; *Jacobi*, 2012; *Conte et al.*, 2018; *Pokhotelov et al.*, 2018; *Wilhelm et al.*, 2019a). Furthermore, also other integral subharmonics of a solar day occur, but these will not be considered in this thesis.

- The third wave type which is of enormous importance for the atmosphere are gravity or buoyancy waves. The restoring force of these waves is gravity, and they have characteristic periods of minutes up to some hours in the atmosphere. The horizontal extension ranges between a few km and up to several 100 km. The primary cause of gravity waves is located in the troposphere when air flows over orographic irregularities as mountains. Furthermore, they can be generated due to vertical movements in convection cells and due to strong wind shears (e.g., *Baumgarten et al.*, 2018). Gravity waves can also be generated in the stratosphere and lower mesosphere (*Becker and Vadas*, 2018). While traveling upwards up to the mesosphere, propagating gravity waves show an exponential growth in amplitude to compensate the decrease of the atmospheric density. Large wave amplitudes break as they reach a critical level which is defined by the background wind speed or as the amplitude of the wave is so large that they become unstable and dissipate their stored transported energy and momentum onto the mean flow. This transfer of momentum onto the mean wind, which is called gravity wave drag, can accelerate or decelerate the mean flow (e.g., *Fritts and Alexander*, 2003; *Smith*, 2012). It further also reverse the whole wind regime. The gravity wave interaction with the mean flow influences the residual summer-to-winter pole circulation in the mesosphere.

The typical horizontal phase speed of gravity waves is in the same order as the background mean flow. Gravity waves can get filtered by the mean wind, if the phase speed of the waves is in range of the background mean flow. Therefore, only wave who move against the background mean flow are able to reach higher altitudes. Under typical summer conditions the background mean wind reaches westward wind values of around 20 m/s for the stratosphere at mid-latitudes. Gravity waves with an eastward directed phase speed or a westward phase slower than 20 m/s are able to propagate up the the mesosphere (*Placke*, 2014). Gravity waves with phase speeds larger than the background mean flow are hindered to pass the stratosphere. During the winter, the prevailing eastward directed wind with values of around 5 m/s at mid-latitudes allows only gravity waves with eastward directed phase speeds below 5 m/s and westward directed phase speeds to move upward to mesospheric heights. A detailed description of the characteristics

2.3 Neutral density variations and its influence on the Earth rotation

and dynamics of gravity waves is provided by e.g., *Fritts and Alexander (2003)*. Gravity waves play also an essential role in the mesospheric temperature. Due to the back and forth between the upward propagating wave and their restoring force arises oscillations of air parcels which oscillate in a stable atmosphere with a frequency called Brunt-Väisälä frequency N (e.g., *Andrews et al., 1987*). This frequency is defined by:

$$N = \sqrt{\frac{g}{T} \left(\frac{\partial T}{\partial z} + \frac{g}{c_p} \right)}, \quad (2.9)$$

where T is the background temperature, g the acceleration of the Earth, c_p the specific heat capacity at a constant pressure level.

Furthermore, a vertical displacement of such an air parcel lead to an adiabatic cooling for upward displacements and an adiabatic heating for descent movements, which explains the decrease of the mesospheric temperature for the summer hemisphere and increase in the winter hemisphere, respectively. An air parcel, which adiabatically displace upwards/downwards, cools/warms at a rate of $9.8K$ per km under the assumption of a dry atmosphere (*Shepherd, 2007; Hocking et al., 2016*). Based on this adiabatic heating/cooling associated with the vertical displacement of the air parcels, the residual-mean circulation maintains the thermal structure of the middle atmosphere (e.g., *Sato et al., 2013*).

The activity of gravity waves can mathematically be expressed in terms of wave numbers and wave frequencies, which is usually not directly observable. Therefore, according to *Tsuda et al. (2000)* the total wave energy provides a good approximation to describe the gravity waves activity. This total wave energy E_{total} is defined as the sum of the potential energy E_p and kinetic energy E_k per unit mass and is given by:

$$E_{total} = E_p + E_k = \frac{1}{2} \frac{g^2}{N^2} \left(\frac{\rho'}{\bar{\rho}} \right)^2 + \frac{1}{2} (u'^2 + v'^2 + w'^2), \quad (2.10)$$

where u' and v' are the perturbation of the horizontal wind velocity and w' is the vertical wind perturbation to the wave propagation direction. Even with exact measurements w' is much smaller than the horizontal perturbations and is very often neglected. $\bar{\rho}$ and ρ' are the background density and its perturbation. The kinetic part of the total energy can be estimated the from MR wind observations, while the estimation of the potential energy is more challenging due to the lack of direct density measurements.

2.3 Neutral density variations and its influence on the Earth rotation

Within one year the Earth revolves once around the Sun. According to the first Kepler law, this happens in a reasonable approximation on an elliptical trajectory. During the

Chapter 2 Theoretical principles of wind and temperature in the Earth's atmosphere

northern hemispheric winter, the distance between both celestial bodies is approximately 3.29% shorter than during the northern hemispheric summer. Based on the inverse square law

$$intensity \propto \frac{1}{distance^2}, \quad (2.11)$$

this leads to an increased heating of the MLT, resulting in an expansion of the neutral density compared to the annual mean. On longer periods, as e.g., the 11-year solar cycle, the effect on the neutral density is stronger than within a year. Previous studies, as e.g., *Walterscheid (1989)*, *Marsh et al. (2007)* and *Emmert (2015)* showed the influence of the solar cycle oscillation on the atmospheric density, temperature, chemical compositions, and winds. Especially the height between mesosphere and ionosphere is affected. *Emmert et al. (2010)* showed, based on satellite measurements at about 400 km height, that a reduction of the solar radiation by 3.7% lead to a decrease in the neutral density of approximately 28%. Later, *Stober et al. (2014)* showed a connection between the neutral density and the expansion/shrinking of the MLT using meteor radar measurements. Additionally, they mentioned a correlation between the neutral density and the zonal wind.

The Earth's atmosphere is permanently in motion. Even under the consideration of a stationary atmosphere above the ground, the atmosphere is still moving due to the rotation of the Earth. Therefore, the absolute velocity v_a of an air parcel in the atmosphere can be described as:

$$v_a = v_{rel} + \omega x r, \quad (2.12)$$

where $\omega x r$ is the velocity due to the rotation of the Earth (e.g., *Driscoll, 2010*). r is the distance from the center of the Earth towards the air parcel. Further, the angular momentum m of an air parcel of unit volume in the atmosphere is described as:

$$m = \rho x (v_{rel} + \omega x r), \quad (2.13)$$

where ρ is the density of the air parcel. The global angular momentum M describes the rotation of the Earth system, which includes the rotation of the solid Earth and the rotation of the atmosphere. It is described according to e.g., *Egger et al. (2007)* by:

$$M = \int_V m dV = \int_V \rho x (v_{rel} + \omega x r) dV \quad (2.14)$$

and can further be separated into a mass part M_ω and a relative part M_r (e.g., *Madden and Speth, 1995*; *Wilhelm et al., 2019b*). The mass part represents the value of the angular momentum would take if the atmosphere is stationary to the ground. The relative part describes the part of the angular momentum which results due to the motion of the atmosphere relative to the Earth's rotation. Under the use of the spherical coordinate system, these parts of the angular momentum can be written as:

2.3 Neutral density variations and its influence on the Earth rotation

$$M = M_\omega + M_r = \frac{r^4 \omega}{g} \int_0^{2\pi} \int_{-\pi/2}^{\pi/2} p_s \cos^3 \theta \, d\theta \, d\lambda + \frac{r^3}{g} \int_0^\infty \int_0^{2\pi} \int_{-\pi/2}^{\pi/2} v_{rel} \cos^2 \theta \, d\theta \, d\lambda \, dp. \quad (2.15)$$

Here, p_s is the surface pressure, λ is the longitude, and θ is the latitude, and g is the acceleration due to gravity. Furthermore, the surface pressure is given by:

$$p_s = \int_0^\infty \rho(z) g(z) \, dz. \quad (2.16)$$

To list here a full derivation of the angular momentum would be beyond the scope of this thesis. However, a more detailed description and derivation of the underlying physics is given in e.g., *Trenberth and Guillemot (1994)*; *Madden and Speth (1995)* and *Egger et al. (2007)*.

The rotation speed of the Earth is not constant. Any changes on seasonal time scales are connected mainly with variations in the tropospheric zonal wind. These wind changes are accompanied with a transfer on their angular momentum on the Earth's surface and these fluctuations results in changes in the duration of a day. Since the early 1960s, these fluctuations are measured using very long baseline interferometry networks. The detection of far distance quasi-stationary light sources, like quasars, lead to daily Earth rotation speed measurements. Based on these measurements the duration of a day is estimated. The difference between 84600s and a measured day is called length of day (LOD). Large scale geophysical processes as e.g., El Niño (e.g., *Dickey et al., 1994*) and the stratospheric quasi-biennial oscillation (QBO) also affects the LOD (e.g., *Volland, 1988*; *Eubanks et al., 1988*).

Chapter 3 Experimental methods

3.1 Instruments for wind measurements in the MLT

For atmospheric studies, a variety of different radars are used and they operate at different frequencies. Table 3.1 gives an overview of the classification of radio bands, including their frequencies and wavelengths. In this thesis, two types of radars are used; the specular meteor radar (MR) and the high/medium frequency radar (MF). Here, the MF is mainly used to fill existing data gaps at a single location, as described in Chapter 5. The following part describes the characteristics of each radar system, as well as the wind estimation approach. A general overview of the system parameters for each radar is listed in Table 3.2.

Name	Frequency	Wavelength
Low frequency (LF)	30 - 300 kHz	10 - 1 km
Medium frequency (MF)	0.3 - 3 MHz	1000 - 100 m
High frequency (HF)	3 - 30 MHz	100 - 10 m
Very high frequency (VHF)	30 - 300 MHz	10 - 1 m
Ultra-high frequency (UHF)	300 - 3000 MHz	1 m - 10 cm
Microwave region	> 3000 MHz	< 10 cm

Table 3.1 Classification of radio bands.

3.1.1 Meteor Radar

When a meteoroid enters the Earth's atmosphere its velocity gets strongly decelerated due to friction with the increasing density of the atmosphere. The impinging atmospheric molecules lead to the formation of plasma around the meteoroid. The released meteoric material further collides with atmospheric molecules and causes an ambipolar

3.1 Instruments for wind measurements in the MLT

	geographical coordinates	Frequency (MHz)	Peak pulse power(kW)
Andenes	69.3°N, 16.0°E	32.55	15
Juliusruh	54.6°N, 13.4°E	32.55, 53.5	30
Collm	51.3°N, 13.0°E	36.2	6
CMOR	43.3°N, 80.8°W	17.45,29.85,38.15	6-12
Davis	68.6°S, 78.0°E	33.2	7.5
SAURA	69.1°N, 16.0°E	3.17	120

Table 3.2 System

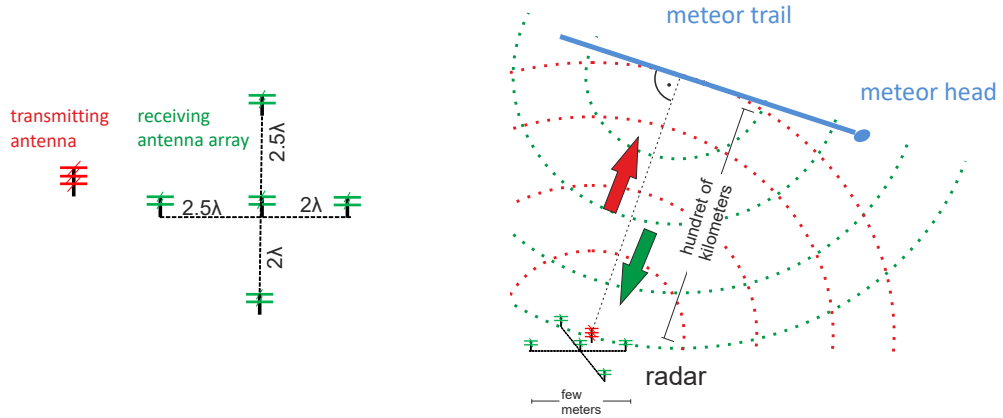


Figure 3.1 Antenna setup for a specular meteor radar, with one transmitting antenna (red) and 5 receiving antennas (green), arranged in a Jones configuration. The transmitted signal (red dotted) gets reflected perpendicular from the meteor trail (blue) and travels back the receiving antenna array (green dotted). The dark blue and light blue waves correspond to a change of doppler velocity.

diffusing plasma trail or an ionized column of gas along its flight path.

From the meteor radar transmitted radio waves are reflected, under specular conditions, at heights between of approximately 75 and 110 km. The all-sky MRs operate between the HF and VHF band. In this thesis, the MR consist of one circular polarized

Chapter 3 Experimental methods

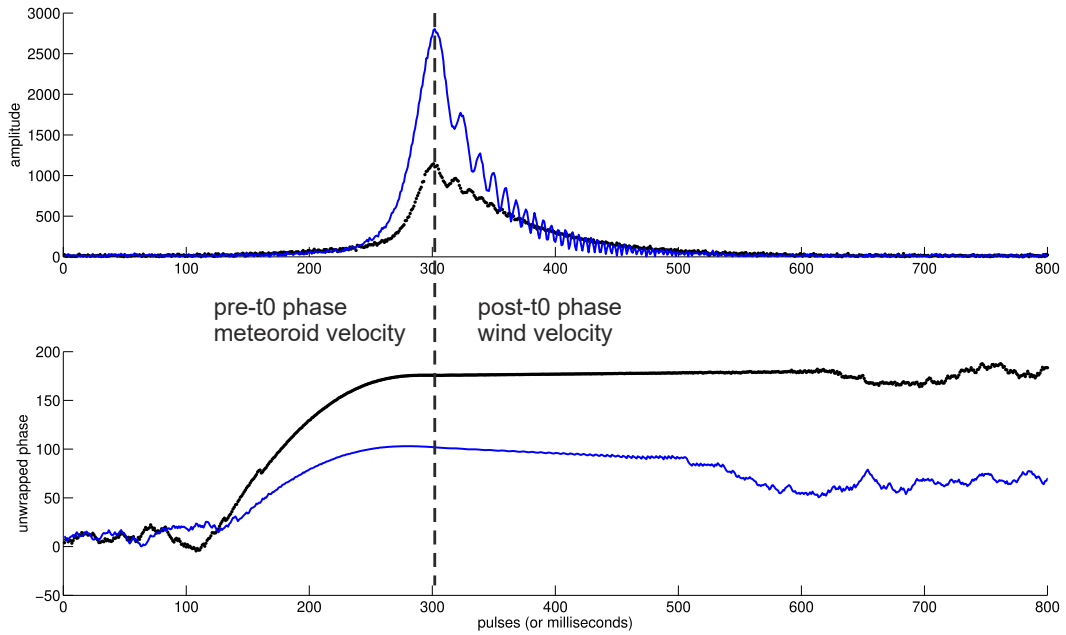


Figure 3.2 Amplitude (top) and phase (bottom) of two different specular meteors, measured with the radar system MAARSY. Figure provided by C. Schult

transmitting and five circular polarized receiving antennas (see Figure 3.1). The receiving antennas are arranged in an asymmetric Jones array with distances of 2 and 2.5 λ . Under the assumption of only one observable meteor trail per time at a specific range, it is possible to use the phase differences between all five antenna pairs to determine its position in the sky.

Based from the backscattered signal, it is possible to determine winds and temperatures of the neutral atmosphere. The received signal can be split into an amplitude and phase, as shown for two examples of the VHF radar MAARSY in Figure 3.2. The upper part shows the amplitude of the measured meteor trail and the lower part the time evolution of the phase.

The atmospheric temperature T is determined by estimating the exponential decay of the signal amplitude, which corresponds to the ambipolar diffusion coefficient D_a . The temperature can then be inferred from equation $D_a = K \frac{T^2}{p}$ either assuming a pressure or by replacing the pressure or density by a empirical temperature gradient model. K is a theoretically derived constant and p the atmospheric pressure, which turned out to be untrustworthy documented (*Hocking et al.*, 2001). The main focus of this thesis relies on the determined winds and the estimation of these will be described in more detail in Section 3.2, but basically the radial velocity of each meteor trail is used to estimate the atmospheric wind.

In this thesis the used MR systems are from five different locations: Andenes (69.3°N, 16°E; Norway), Juliusruh (54.6°N, 13.4°E; Germany), Collm (51.3°N, 13.0°E; Germany), Tavistock, named CMOR (43.3°N, 80.8°W; Canada), and Davis (68.6°S, 78.0°E; Antarctica). Figure 3.3 displays the geographical positions of each radar.

3.1 Instruments for wind measurements in the MLT

The high latitude locations Andenes and Davis are located within the polar vortex, a large rotation area of low pressure and cold air which surrounds the poles. During the winter the polar vortex can become unstable and allows the transport of cold air from the poles towards the mid-latitudes. Furthermore, the location of Andenes at northern Scandinavia as well as the location of Davis in the Antarctica are highly influenced by mountain waves, which is not the case for the other locations. The geographical location is rather important to understand potential effects due to orographic mountain waves or secondary wave generation, which can significantly alter the observed gravity waves energies or mean wind climatologies.



Figure 3.3 Geographical positions of the used radar instruments.

3.1.2 Medium Frequency Radar

The second radar used in this thesis is the MF radar Saura (69.1°N , 16.0°E ; Norway). Historically build as a MF radar, it is operating nowadays in the HF band at a frequency of 3.17 MHz. The transmitting and receiving antenna array is formed by 29 halfwave cross-dipole antennas, with a distance of 0.7λ to the neighbor, arranged in a so-called Mills Cross array, complemented by two additional antennas close by (see Figure 3.4). The system has in total an extension of $1 \times 1 \text{ km}^2$ and is able to operate in spaced antenna mode, as well as to conduct Doppler beam swinging experiments, which requires to tilt the beam towards off-zenith angles between 6.8° and 7.3° . The system observes changes in the electron density at heights between 60 to 100 km. In this work, the measurements of the MF radar are mainly used for MR data optimization. Furthermore, this is only done at the location of Andenes, simply due to the lack of MF capabilities at the other MR locations. More information about the Saura radar and its measurements possibilities can be found in *Singer et al. (2008)*; *Wilhelm et al. (2017)* and *Renkowitz et al. (2018)*.

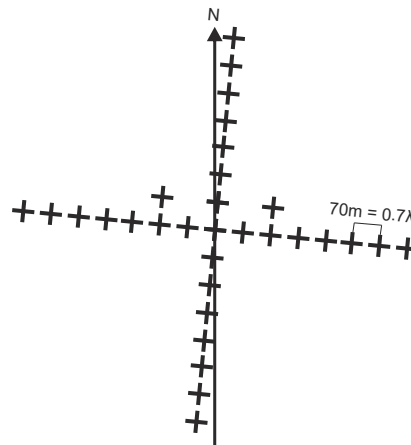


Figure 3.4 Antenna setup of the MF Saura radar, consisting of 29 antennas in a Mills Cross arrangement with two additional transmission antennas.

3.1.3 Other instruments

Further instruments can be used to investigate the MLT region, whereby all of these systems have their strengths and weaknesses. Beside meteor radar other instruments exist, with partly higher spatial and temporal resolution, but are limited to measure continuously, simply due to weather conditions or due to the occurrence of their scatterer. Below are few examples, which are used to determine winds in the MLT altitudes.

- Fabry-Perot Interferometer: By the detection of airglow emissions of several chemical components as OH (892 nm at 87 km); OI (557.7 nm at 98km) winds can be estimated on specific height levels (*Yuan et al.*, 2010).
- lidar: With the use of a metal resonance lidar, wind measurements can be obtained at MLT heights (*Kawahara et al.*, 2017; *Li et al.*, 2018). The system is able to measure during night and day, but is limited on clear sky conditions.
- Other radars: Depending on the frequency, also other radar systems are able to measure atmospheric winds, as e.g., the very high frequency (VHF) Middle Atmosphere Alomar Radar System (MAARSY), which is able to derive winds by using e.g., polar mesospheric echoes (*Stober et al.*, 2012, 2018; *Gudadze et al.*, 2019), or as low frequency systems LF D1, which detect the reflection of transmitted waves in the D-layer and therefore can be used to interpret wind measurements (*Jacobi et al.*, 2001).
- Satellite: Based on geopotential height measurements, the Microwave Limb Sounder (MLS) on board of the Aura satellite can derive horizontal wind components

3.2 Deriving winds from atmospheric remote sensing

(*Matthias and Ern, 2018*).

- Sounding rocket: Measurements of the neutral winds in the mesosphere and lower thermosphere can be done by releases of chemical components (*Larsen, 2002*), or by the use of falling spheres (*Müllemann and Lübken, 2004*).

3.2 Deriving winds from atmospheric remote sensing

Atmospheric radar observations require some understanding of the underlying backscatter processes. As a result radars operating at different frequencies are more or less capable to observe specific atmospheric altitude regions. An overview of the main frequencies is summarized in Table 3.1. Shorter wavelengths are in general used to detect scatterers like raindrops or ice clouds, while longer lengths are more suitable to observe the clear neutral or ionized atmosphere as just turbulence driven perturbations of the refractive index n are required to backscatter the radio waves. These changes in n are defined in terms of the following components:

$$n = 1 + 3.73 \cdot 10^{-1} \frac{e}{T^2} + 7.76 \cdot 10^{-5} \frac{p}{T} - 40.3 \frac{N_e}{f^2} \quad (3.1)$$

where T is atmospheric temperature, e is partial pressure of water vapor, p is atmospheric pressure, N_e is the density of free electrons, and f the radar frequency. The second term on the right side of the equation is the contribution of the permanent dipole moment of water vapor which is only significant in the lower troposphere. In the middle troposphere and the stratosphere, the third term takes into account, which is the contribution from the dipole moment due to the polarization field of neutral molecules. The fourth term is relevant in the mesosphere and describes the contribution of the change of the refractive index due to free electrons (*Fukao and Hamazu, 2014*). Changes in the electron density are caused for example by e.g., energetic particles from the sun or diffusing meteors. Furthermore, changes in the gradient of the electron density can be induced by turbulence.

As described in section 3.1.1 an ionized meteor trail is formed when a meteoroid is entering the Earth's atmosphere. Coherent reflection from meteor plasma provide a sufficient radar target. For the case of a meteor scatter, two geometries are involved: the specular (90° backscatter) reflection from the linear column of ionization scattering from a long cylinder of plasma; and the reflection from the spheroidal plasma generated around the ablating meteoroid, called head-echo. Within this thesis the latter one will be neglected, but more information can be found in e.g., *Westman et al. (2004)*; *Schult et al. (2013, 2018)*.

For the interpretation of the meteor trail echo some premisses need to be done: Each individual electron oscillates freely within the cylindric column without colliding with other particles (coherent scattering). Further, the geometry of the ionized trail is important and the reflection of the signal is described by Fresnel scattering. Under these assumptions, the received echo power from a target can be estimated considering

Chapter 3 Experimental methods

the gain of transmitter and receiver antennas G_T and G_R (McKinley, 1961; Baggaley, 2002) by:

$$P_R = \frac{P_T G_T G_R \lambda^3 \sigma_e}{128 \pi^3 r^3} q^2 \left(\frac{C^2 + S^2}{2} \right) \quad (3.2)$$

where P_R and P_T are the received and transmitted power, λ is the radar wavelength, σ_e is the electron scattering cross section, r is the range between the radar and the meteor trail, and q is the electron line density. C and S are conventional Fresnel integrals of optical diffraction theory and are further defined as:

$$C = \int_{-\infty}^x \left(\cos \frac{\pi x^2}{2} \right) dx \quad \text{and} \quad S = \int_{-\infty}^x \left(\sin \frac{\pi x^2}{2} \right) dx \quad (3.3)$$

Based on C and S , the echo amplitude diffraction can be estimated by $V_r = (C^2 + S^2)^{\frac{1}{2}}$ and its phase by $\tan(\phi) = S/C$. The numerical solution of the integrals is not trivial. Therefore, Baggaley (2002) described that the behavior of the complex diffraction of the Fresnel integrals can be displayed in a good approximation by the Cornu-spiral (Figure 3.6). The relative amplitude is given by the length of the vector from $C = -0.5$ and $S = -0.5$ ($x = -\infty$) to a point along the curve. This expresses the length of the meteor trail in the atmosphere, which is assumed to be infinitely long along the direction of motion of the trail. As the meteor approaches the coordinate $(0,0)$, a strong increase of the signal power occurs, which is visible at around pulse 250 in the amplitude in Figure 3.2. At pulse 300 the t0-point is reached, where the meteoroid is passing the specular condition (Stober and Jacobi, 2007). The receiving information of the Cornu spiral is used to separate the receiving power into S and C . Further, the meteor velocity in the Fresnel interval can be estimated by:

$$v = \frac{\sqrt{r\lambda} dx}{2 dt}. \quad (3.4)$$

During the detection time, the range of the meteor trail to the radar changes very slowly, so fluctuations in the trail position results directly in changes of the radial velocity and can be assigned to movement of the neutral wind. Any change in the post-t0 phase (3.2, right side of the dashed line) apart from a constant phase will show fluctuations of the neutral wind. The phase shift is derived according to the Doppler effect by:

$$f_t = \left(\frac{c}{c \pm v_s} \right) f_r \quad (3.5)$$

where f_t and f_r are the transmitted and received frequencies. c is the speed of light and v_s is the velocity of the meteor trail motion relative to the radar. The radial velocity v_{rad} is the velocity component in the direction of the source is given by $v_{rad} = v_s \cos \epsilon$ (see Figure 3.5). If the trail moves towards the radar v_{rad} get negative, and positive if the trail moves away from the radar. ϵ is the angle between the direction of the transmitted signal and the direction of the movement of the trail.

For the meteor observations within this thesis an arrangement of several receiving antennas were used to estimate the spatial position of the detected meteor tails. This

3.2 Deriving winds from atmospheric remote sensing

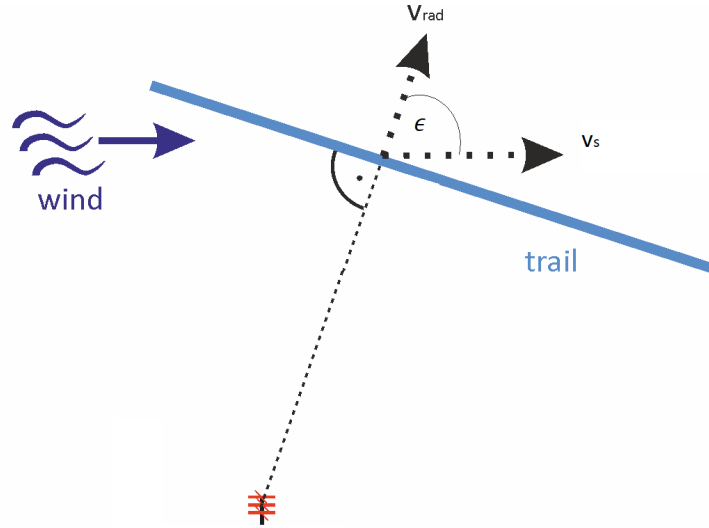


Figure 3.5 Illustration of the radial velocity component in respect to the background wind.

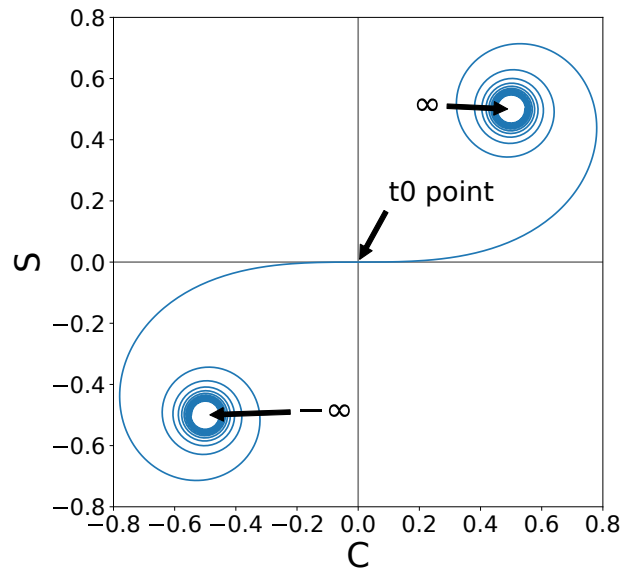


Figure 3.6 Cornu spiral representation as a function of the Fresnel integrals C and S. The coordinate (0,0) shows the specular condition.

array is arranged in an asymmetric cross which is used to determine the azimuth and zenith angle of the scatterer. Based on the time t between the transmitted and the received radio wave the distance r between the MR and the scatterer is estimated using

Chapter 3 Experimental methods

$r = ct/2$. The wind measurements from the meteor radar are obtained using a modified version of the all-sky approach by *Hocking et al. (2001)*, which needs within a given time and altitude bin at least four randomly distributed meteors. Beside the MR, also winds by the MF radar are used. The MF radar derives winds by detecting changes in the electron density, using a Doppler beam swinging method. Hereby, it combines radial velocities of four oblique beams using trigonometry by taking the zenith angle into account (see Figure 3.7). More information about the capability of the MF radar and its wind estimation can be found in e.g., *Singer et al. (2008)*. For both radar systems, the wind vector (u, v, w) for each observed meteor target is obtained according to *Stober et al. (2018)* by:

$$v_{rad}(\theta, \phi) = u \cos\phi \sin\theta + v \sin\phi \sin\theta + w \cos\theta \quad (3.6)$$

where v_{rad} is the radial velocity of each target, θ and ϕ are the zenith and azimuth angle (mathematical convention with reference to East and counterclockwise rotation). The radial velocity refers to the velocity component along the track that points from the radar to the e.g., meteor trail. The coefficients u, v, w are the zonal, meridional and vertical wind components for each single meteor trail. In earlier studies the vertical winds were set to 0 m/s, which lead to a simpler estimation of the horizontal winds. In the current version of the fit approach, the vertical velocity is estimated, but is only used for quality control of the horizontal winds. To obtain an usable hourly wind pattern, a time window of 2 hours shifted by 1 hour and an altitude window of a 3 km kernel centered at the referenced altitude shifted by 2 km is used. Further, each meteor that enters the fitting is weighted with a Gaussian retrieval kernel to account for potential differences in the time and altitude of occurrence compared to the reference bin center. Also considered in the wind estimation is the curvature of the Earth, as described in detail in *Stober et al. (2018)*. The conversion of each spatial meteor position into geodetic position increases the accuracy of the height and angle estimation of each meteor.

Following *Stober et al. (2017)*, *Baumgarten and Stober (2019)* and *Wilhelm et al. (2019a)*, the mean winds and its harmonics are obtained using an adaptive spectral filter. This allows the decomposition of the observed wind and its harmonic oscillations by adapting the window length for each tidal component by using the classical harmonic approach:

$$u, v = u_0, v_0 + \sum_{i=1}^3 a_n \sin(2\pi/T_n \cdot t) + b_n \cos(2\pi/T_n \cdot t). \quad (3.7)$$

u_0, v_0 corresponds to the mean winds and T_n takes the values of 24 hours and 12 hours for the diurnal and semidiurnal tidal component of each wind direction. a_n, b_n are coefficients of the relevant wind. The residuum oscillations corresponds to the gravity wave activity on hourly basis. To visualize the separation into its subharmonic Figure 3.8 shows for a time series of a few days the approach with the observed zonal wind data (top) into the the mean zonal wind including the tides (middle), and the gravity waves residuum (bottom). The adaptive spectral filter method is based on least squares and therefore robust against data gaps shorter than the used window length. Additionally, restrictions are implemented for the calculation of the mean winds and

3.2 Deriving winds from atmospheric remote sensing

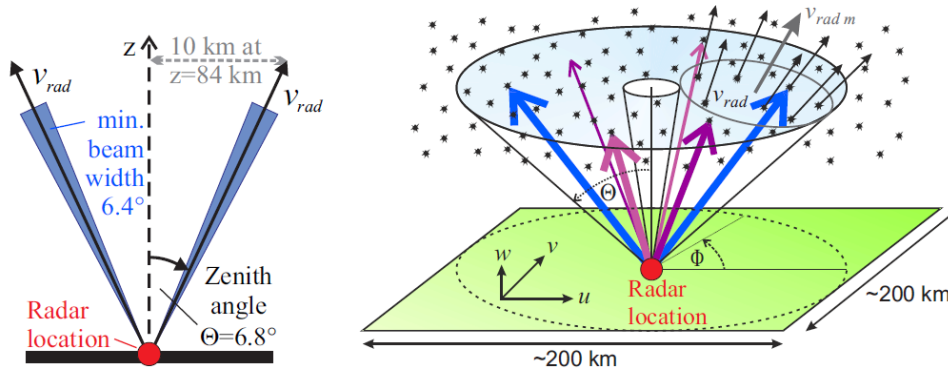


Figure 3.7 Schematic of the dual beam method for the MF SAURA radar (left) and for the all-sky meteor radars (right). Colored arrows corresponds for several meteor positions. Figure adopted from *Placke (2014)*. The radial velocity (v_{rad}) of a target to the radar is that part of the trail velocity that is directed toward or away from the radar.

tides, which implies vertical information. The vertical wavelength is assumed to show only small changes within a vertical kernel function of 8 km for the mean winds and 10 km for the tidal phases.

The resulting daily mean winds can further be used to derive planetary wave activities. The activity of these waves include oscillations which have a period of at least one season. For the estimation of the planetary wave activity winds, first, seasonal background winds (u_m, v_m) are estimated using the daily mean time series of u_0, v_0 by:

$$u_0, v_0 = u_m, v_m + \sum_{i=1}^2 a_n \sin(2\pi/T_n \cdot t) + b_n \cos(2\pi/T_n \cdot t). \quad (3.8)$$

a_n, b_n are coefficients for the subharmonics on seasonal basis with periods of $T_n = 365.25/n$ days ($n = 1, 2$). The background wind field for every month is derived by fitting the seasonal model to the daily mean wind time series. The sliding window length is 2 years centered at the 15th of the respective month. The planetary wave activities are then derived by subtracting the daily mean winds from the seasonal background winds. Based on the derived monthly values, short time events as e.g., sudden stratospheric warmings are not affecting the monthly mean values. The benefit of the ASF compared to the classical wavelet analysis is that the ASF can handle unevenly sample data and data gaps. Further implemented is a full error propagation to all derived parameters. Another benefit of the ASF, a regularization constrain for the mean winds and the tides is implemented, which make use of vertical wavelength information. Additional information about the adaptive spectral filter can be found in *Stober et al. (2017)*, *Baumgarten and Stober (2019)* and *Wilhelm et al. (2019a)*.

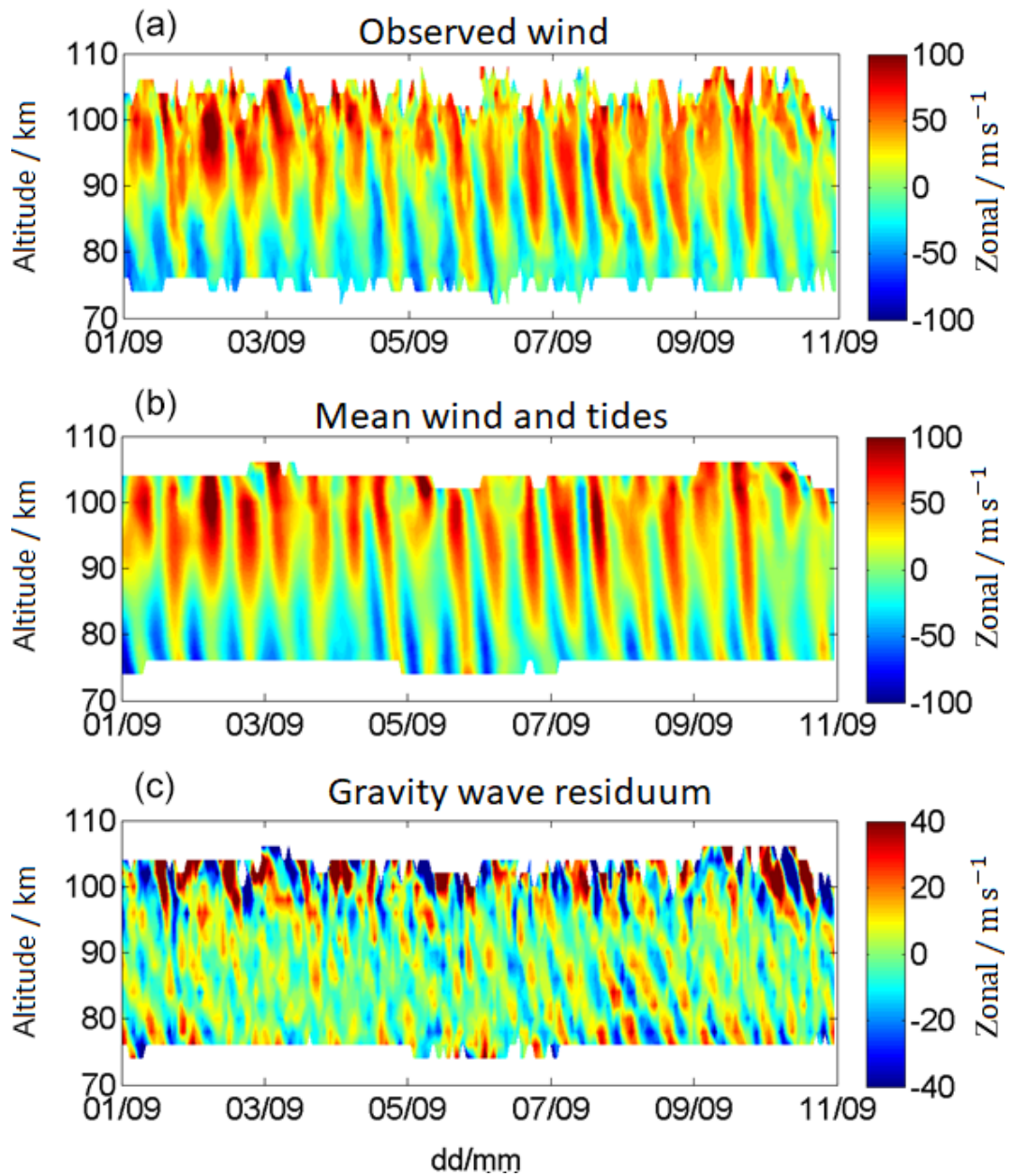


Figure 3.8 Decomposition of the observed wind (top) into the mean wind and tidal component (middle), and the gravity wave residuum (bottom) for Andenes 01/09/2017 - 11/09/2017. Note the different labels of the colorbar. Figure adopted from *Wilhelm et al. (2019a)*, Figure 1.

Chapter 4 Objectives of the thesis

During the past decade, there were many studies investigating long-term wind measurements to obtain and infer changes at the MLT of anthropogenic or solar origin. In general, many of these studies showed similarities in the observations and tendencies in the winds and atmospheric waves, exhibiting the high quality and advances of instruments. Nevertheless, also differences between several observations occur, which among other things, are the result of the usage of different observational devices, as e.g., lidars, radars, microwave radiometers, or satellites. All these systems have their advantages and disadvantages. Some have a higher temporal and spatial resolution, but require specific weather conditions, others are only stationary, but measure nearly continuously at a specific location. Regarding their technical design all instruments are restricted to a certain altitude range and resolution.

To overcome discrepancies in the measurements, comparisons between several instruments were made at the same location e.g., between lidar and radar system as shown in e.g., *Liu et al.* (2002), or between different radar types as presented in e.g., *Jacobi et al.* (2008). In general, different systems show similar mean wind climatologies, but differ distinctly in the magnitude, e.g., in a study by *Franke et al.* (2005) by up to 17 m/s. Furthermore, some clear atmospheric structures occur at different heights as shown e.g., in a survey by *Jacobi* (2011). Different altitudes used along the summerly zonal transition height between radar and LF measurements. One goal of this thesis is to compare two separate radar systems, which are located close by to find a potential bias between the systems and to estimate a correction factor, which allows merging the measurements of both systems to one homogeneous data set. The advantage of a correction factor is that prospective measurement losses of one system can be compensated.

Beside the instrumental discrepancies, long-term observation of similar systems can also differ, regarding the evaluation method, the used temporal and spatial sampling, or by physical reasons as geographical location or measurement periods. Therefore, it is complicated and not straight forward to compare long continuous measurements with each other. Additionally, models can be used to capture a global picture of wind climatologies and help to explain long-term changes, but they also come with different results compared to instruments or different model types. Nevertheless, long-term observations are essential to improve our understanding of on-going atmospheric dynamical changes. Within this thesis, the benefit of meteor radar observations are used to estimate horizontal winds in the upper mesosphere and lower thermosphere. Compared to other radar systems, meteor radars have the immense advantage of a nearly time

Chapter 4 Objectives of the thesis

independent and continuous flow of measurable targets, which allowed for the second part of the thesis to determine nearly continuous long-term measurements and tendencies of winds and wave activities for several locations over the extended period. For an optimal comparison of several measurement locations, it is beneficial to use the same analysis scheme or wind retrieval method to avoid other systematic effects that might be related to the analysis (as described in Section 3.2).

The long-term behavior of the mesosphere-lower thermosphere and its physical parameters underlies the influence of several factors. On a long time scale, it was found among other things, that an enhancement of CO_2 leads to cooling in the mesosphere (Lübken *et al.*, 2013). Furthermore, several studies show the connection between changes of atmospheric mass density in combination with temperature fluctuations in the thermosphere (e.g., Emmert *et al.*, 2004; Marcos *et al.*, 2005) or long-term changes electron density (e.g., Akmaev *et al.*, 2006; Laštovička *et al.*, 2012). Within the thermosphere, Emmert *et al.* (2010) showed, based on satellite measurements, that the neutral density decreases strongly between the minima of the solar cycle 22/23. Changes in the neutral density also occur in the MLT region, and affect the detection altitude of meteor measurements, as well as the behavior of the prevailing horizontal wind, as shown in a study by Stober *et al.* (2012) for the winter season 2009/10. Within the third part of this thesis, a connection between density changes due to variations in the solar radiation and changes in the zonal wind pattern, on seasonal time scales, is investigated to improve the understanding of long-term dynamical processes in the MLT region.

Chapter 5 Comparison of MR winds and MF winds

Summary of :

Wilhelm, S., G. Stober, and J. L. Chau, A comparison of 11-year mesospheric and lower thermospheric winds determined by meteor and MF radar at 69°N, *Annales Geophysicae*, 35, 893-906, doi:10.5194/angeo-35-893-2017, 2017.

The comparison of wind measurements by different instruments usually shows a difference in wind values. While the mean wind pattern for an extended period results to be in a good agreement, the magnitude of the amplitudes differ. In the study of *Wilhelm et al.* (2017), two different radar systems, which are located close by, are compared to estimate a factor which allows to correct this magnitude difference regarding height and season. Additionally, does the estimation of this correction factor allows to merge both data sets. This combination is useful to fill data gaps in the observations of system, which are created due to e.g., maintenance.

The two radar systems, located at 69°N, 16°E, can observe wind speeds in an enhanced altitudinal coverage from 60 to 110 km. The two systems are the Andenes specular meteor radar (MR, 32.55 MHz, 30 kW Power) and the medium frequency radar SAURA (MF, 3.17 MHz, 116 kW Power). The MR can obtain the radial velocities of ionized meteor trails, and the MF uses its capability of oblique beams to observed changes in the electron density in several directions. While both systems are technically different, the hourly horizontal winds which are obtained were computed with the same modified approach of the so-called all-sky-fit method (*Hocking and Thayaparan, 1997; Hocking et al., 2001; Stober et al., 2017*). Furthermore, the tidal components are obtained from the observed wind by estimating the diurnal (24h) and semidiurnal (12h) components using a decomposition, as described in *Stober et al. (2017)*. The resulting winds and tides of the MR cover the heights between 78 and 110 km, and for the MF in the range between 60 and 100 km, resulting in a comparable altitude coverage between 78 and 100 km. The comparison was made for the years 2004 - 2014.

In the first step, the horizontal winds of both radar systems were compared by estimating an annual composite. While both radars showed the typical mesospheric seasonal zonal wind climatology, it figured out that the winds of the MF radar compared to the MR radar are in general weaker, and that the meridional component above

Chapter 5 Comparison of MR winds and MF winds

~92 km show opposite directions between both systems. Earlier studies also found differences in the wind amplitudes, so *Hall et al.* (2005) determined an offset of 20% in the meridional wind below 90 km, and in a study by *Manson et al.* (2004), occurred a difference during the winter between 20 and 50%. In the current study, a difference of 10-60% for the meridional component below 92 km was estimated which varies regarding season and altitude. Regarding the zonal values, the MF radar underestimates the MR winds for nearly every season and every altitude.

Furthermore, a comparison between the diurnal and semidiurnal tidal components of both systems was done, resulting in an amplitude differences and a phase offset. The phase difference corresponds to a time offset of the apparent tidal wave between both systems. Below 90 km the amplitudes and the phases of both radar are in a good agreement. Above 90 km the phase difference of the daily phase increases with increasing altitude and reaches an offset of up to ~12h for the summer and of up to ~6h for the winter.

Mainly two reasons can be named to describe differences in the wind, and therefore the tidal measurements between both systems. The first is based on the MF measurement volume for the oblique beams. Assuming an homogenous mesosphere means that electron density decreases exponentially even within a horizontal area. In this case, a vertical measurement volume beam will show the same electron density value at every position within the beam, for the same distance between the radar and the measurement height. The angular pointing of the beam is determined by taking the average of the horizontal beam volume. This results that for the vertical beam the angular pointing of the beam is equal to the averaged beam. By the use of a oblique beam, the volume beam doesn't show anymore the same electron density for every point within the beam. This leads to small pointing differences between the actual beam pointing and the nominal direction and therefore results in not correct estimated heights. Later, *Renkowitz et al.* (2018) optimize this inconsistency by implementing a mean angular correction, similar to proposed in the present study. The second reason which causes differences of the MF winds to the MR winds is based on the different scattering processes. According to *Singer et al.* (2008), differences for the MF radar of up to 10 dB occur between the main lobe of a vertical beam and the corresponding side lobes. The dynamic range of scattering in the D layer is about 35 dB. Therefore, a side lobe contamination can affect the measurement itself, which can result in incorrect wind values.

Based on the different winds and tides and on the aim to combine both data sets, the estimation of a correction factor has been done to receive similar monthly mean values. To achieve this correction factor in a first approach a correlation coefficient R^2 between the winds of both radars were determined. In Figure 5.1 is shown R^2 as a composite to point on inter-annual features. The highest correlation with values of larger than ~0.6 was found at heights between 80 and 92 km for the months May until February. Above 92 km for the zonal, and 94 km for the meridional wind R^2 drops below 0.5 and decreases further with increasing heights.

Furthermore, a second minimum occurred during the spring and summer below ~80 km. Comparable results were found for the tidal components. Taking these results into account and add one another approach to remove potential biases, the correction factor was determined, for each season and each altitude (Figure 5.2). It figured out

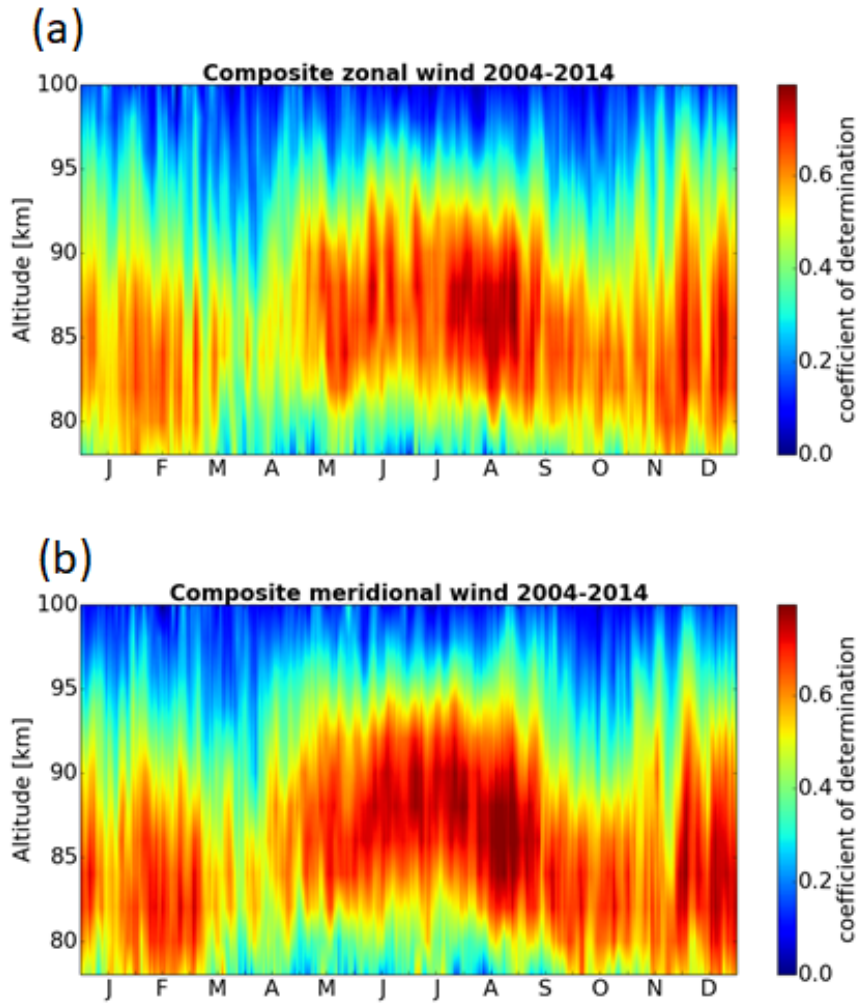


Figure 5.1 Composite of R^2 for the zonal (a) and meridional (b) wind component of the overlap altitude of MF radar and meteor radar for the years 2004 - 2014. The data have been smoothed by a 5-day running mean. Figure taken from *Wilhelm et al.* (2017), Fig. 7.

that the correction factor can be described well by a polynomial function to a second degree with the minimal values during the months June, July, and August.

With the use of the correction factor, it was possible to combine both data sets. Therefore, the correction factor was applied as a weighting function to the MF data for the heights between 78 and 92 km to fill existing MR data gaps. Above 92 km, only meteor data were used for the combined data set, due to increasing discrepancies between both systems. Below 78 km only MF data were used without any correction, due to lack of MR data. Figure 5.3 shows the combination of both data sets for the randomly chosen year 2006 (a) and as a composite for the complete data set (b).

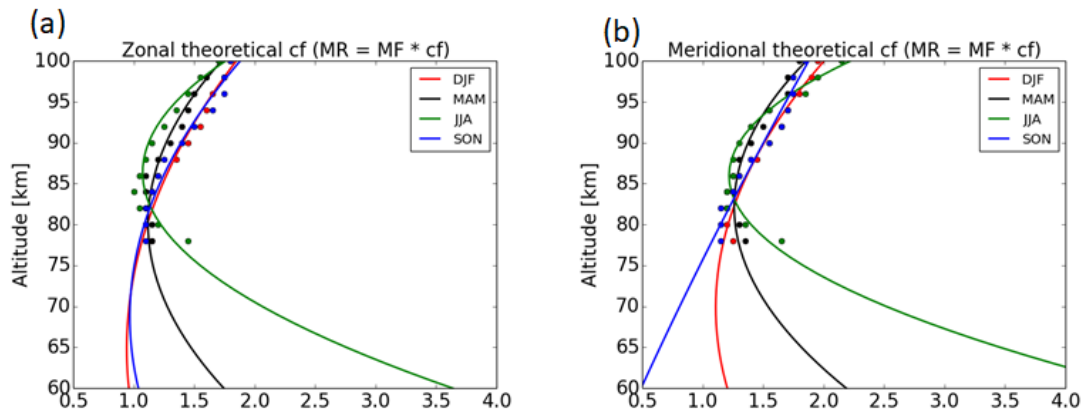


Figure 5.2 Theoretical seasonal correction factor for the zonal (a) and meridional (b) wind component of the MF radar. The points between 78 and 100 km are based on a comparison between two radars and fitted curves are polynomial functions of second degree. Figure taken from *Wilhelm et al. (2017)*, Fig. 10.

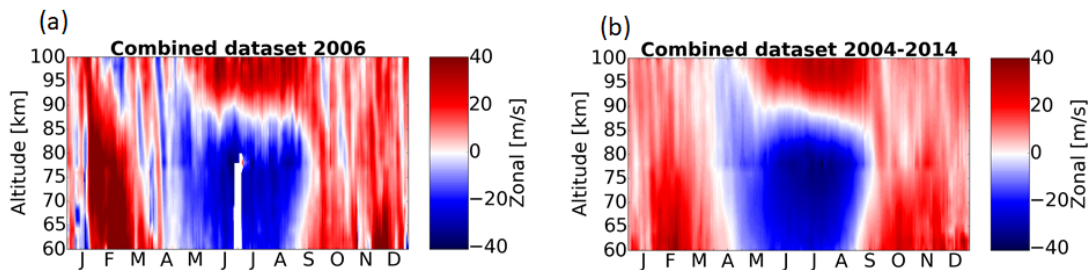


Figure 5.3 Zonal wind component for the year 2006 (a) and the composite for the years 2004 - 2014 (b). Below 78 km the data are based on the MF system, and above 92 km they are based on the MR radar. The overlapping area is based on the MR and the gaps within this area are filled with weighted MF radar. The white areas during June 2006 are missing values. Figure taken from *Wilhelm et al. (2017)*, Fig. 14.

Chapter 6 Long-term MLT wind measurements

Summary of :

Wilhelm, S., G. Stober, and P. Brown, Climatologies and long-term changes of mesospheric wind and wave measurements based on radar observations at high and mid latitudes, *Annales Geophysicae*, 37, 851-875, doi:10.5194/angeo-37-851-2019.

Long-term observations of mesospheric and lower thermospheric winds, tides and the kinetic energy of planetary and gravity waves are reported in the study of *Wilhelm et al.* (2019a). The parameters were estimated based on meteor radar measurements between the years 2002 and 2018 for the high-latitude location Andenes (69.3°N, 16°E; Norway) and the mid-latitude locations Juliusruh (54.6°N, 13.4°E; Germany) and the CMOR radar at Tavistock (43.3°N, 80.8°W; Canada). The setup of all meteor radars is similar and the winds are derived with the same wind fit approach. The observations cover the heights partly between 70 and 110 km, with a vertical resolution of 2 km and an hourly temporal resolution. The statistical uncertainties are based on a full error propagation of the radial wind errors and the number of detected meteors per altitude and time bin. The resulting wind velocity uncertainties vary between 2 and 16 m/s, whereby larger errors mainly occur due to a smaller count rate at the upper and lower edge of the meteor observation layer.

The observed wind consist of a superposition of several waves. A decomposition into the spectral components requires a good knowledge for data handling and interpretation. Over the last years, several studies address this issue in different ways (e.g, *Eckermann et al.*, 2016; *Hysell et al.*, 2017). Within this study, the decomposition of the observed wind into its harmonics was done according to *Stober et al.* (2017), by applying an adaptive spectral filter technique on the classical harmonic approach. The adaptive spectral filter allows the decomposition the original wind series into a mean wind, a diurnal and a semidiurnal tidal component, and a gravity wave residuum. After removing the tides and the gravity waves from the daily mean wind, it is further possible, to obtain planetary wave activity. By handling wind measurements which exceeding a period longer than a solar cycle, the influence of the Sun on the observations need to be considered.

The resulting long-term measurements of winds and waves were used in combination

Chapter 6 Long-term MLT wind measurements

with a linear trend model, which includes an 11-year oscillation, to estimate climatologies and long-term changes for each location. Comparing tendencies with other studies results to be difficult due to different prerequisite as e.g., observed time series, filter processes, location, and instruments. Nevertheless, the main specific conclusions of *Wilhelm et al. (2019a)* are:

- The climatologies of the mean wind of the three radar systems indicate a similar pattern for the high and mid-latitude locations, but it occurs a latitudinal dependence of the summer zonal mesospheric transition height between eastward and westward winds (see Chapter 2, Figure 2.2). This transition height increases in altitude towards higher latitudes. Also, there are latitudinal differences in the eastward directed wind during winter (December - February), which results in westward winds above 100 km for the lowest mid-latitude location CMOR, and oppositely directed winds for Juliusruh and Andenes. The meridional wind climatologies also show a typical summer and winter wind pattern which vary with latitude. During the winter, a jet reversal from northward to southward winds is confirmed, which is located lower at heights towards high latitudes. Furthermore, the altitude of the directed southward wind decreases in height for lower latitudes and corresponds to the behavior of the summer zonal wind reversal. The general pattern of the climatologies fit previous measurements and model studies but differs partly in the magnitude due to disparities in period and in different window fit length (e.g., *Schminder and Kürschner, 1994*; *Yuan et al., 2008*; *Lukianova et al., 2018*).
- Long-term tendencies (Figure 6.1) of the horizontal seasonal winds differ regarding latitude, height and component for each month. The most apparent linear response is an enhancement of the southward directed wind at Andenes and a southward directed weakening at Juliusruh from June to September. For CMOR, an overall eastward acceleration takes place during the months April - June, which corresponds to a weakening of the westward directed wind jet below 84 km and a strengthening of the eastward winds above. Concordant and contradictory tendencies were found in earlier studies, which underlines the importance of continuous long-term observations and the use of similar filter methods (e.g., *Hoffmann et al., 2011*; *Geißler and Jacobi, 2017*).
- Annual mean winds show nearly no linear changes for the mid-latitude locations, only the yearly mean wind of Andenes shows an intensification of the winds towards south-west increasing with higher altitudes.
- The diurnal tidal component shows a similar pattern for the zonal and for the meridional component, with an increase of the amplitudes above 100 km for Andenes and Juliusruh. The magnitudes of meridional tide also exceeds the values of the zonal tides for these two locations. Furthermore occurs a second, but weaker enhancement around the summerly eastward jet. At CMOR a significant increase of the zonal amplitude takes place, but at all locations almost no significant linear long-term changes arise.

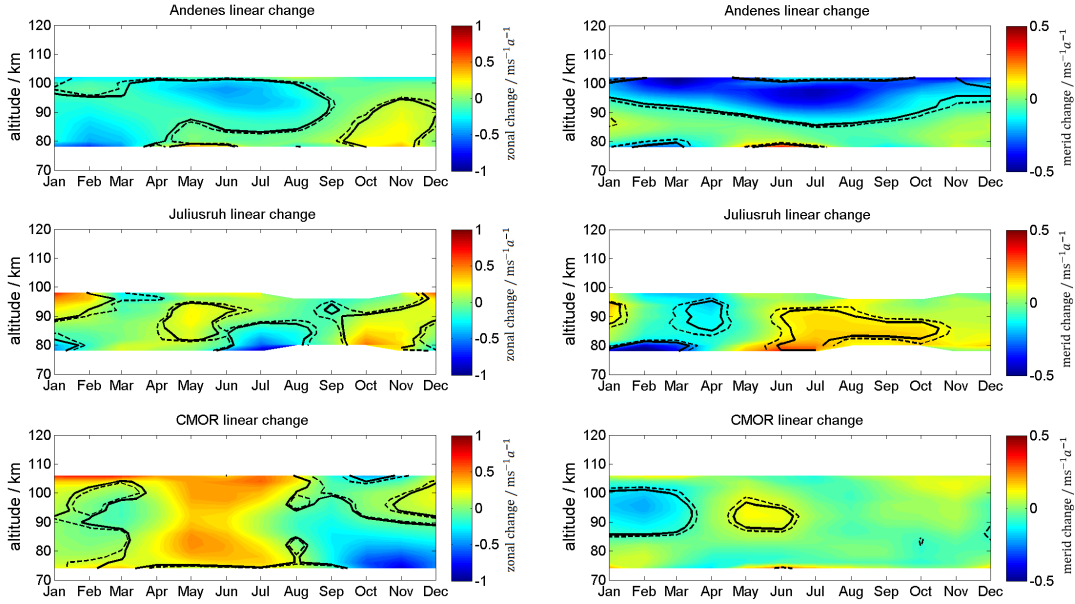


Figure 6.1 Linear long-term changes of zonal (left) and meridional (right) wind for Andenes (top), Juliusruh (middle), and CMOR (bottom). Note the different labels of the colorbar. The solid black lines corresponds to 95% significance, the dashed black lines to the 90% significance. The changes of the wind are presented in m/s per year. Figure taken from *Wilhelm et al. (2019a)*, Fig 5.

- The dominant semidiurnal tide (Figure 6.2) shows similar values for amplitudes and occurrence for the zonal and the meridional component. Only during the fall transition, the semidiurnal tide at CMOR appears to differ in magnitude with higher values for the zonal part. In contrast to the diurnal tides, significant long-term changes occur for the semidiurnal tides, which alter regarding latitude. While at Andenes during November and December the tidal amplitude above 90 km weakens by ~ 1 m/s/year, nearly no changes arises for Juliusruh. CMOR shows a strengthening of the semidiurnal tides of ~ 0.5 m/s/year. Additionally during the fall transition, a decrease in the linear tendency occurs at CMOR.
- Latitudinal dependent year-to-year variabilities occur for the planetary wave activity, with enhanced energies during winter with major sudden stratospheric warmings. In general, the mid-latitude locations show weaker mean activity than Andenes.
- Climatologies of gravity wave activities indicate a similar pattern for all three locations, which strongly varies on seasonal timescales. During the months December until February and September enhanced gravity wave energies occur at each location above 90 km. Additionally, a second but weaker enhancement arises below 80 km at the sites of Andenes and Juliusruh.
- The feedback of an 11-year oscillation on the mean winds (Figure 6.3) shows a

Chapter 6 Long-term MLT wind measurements

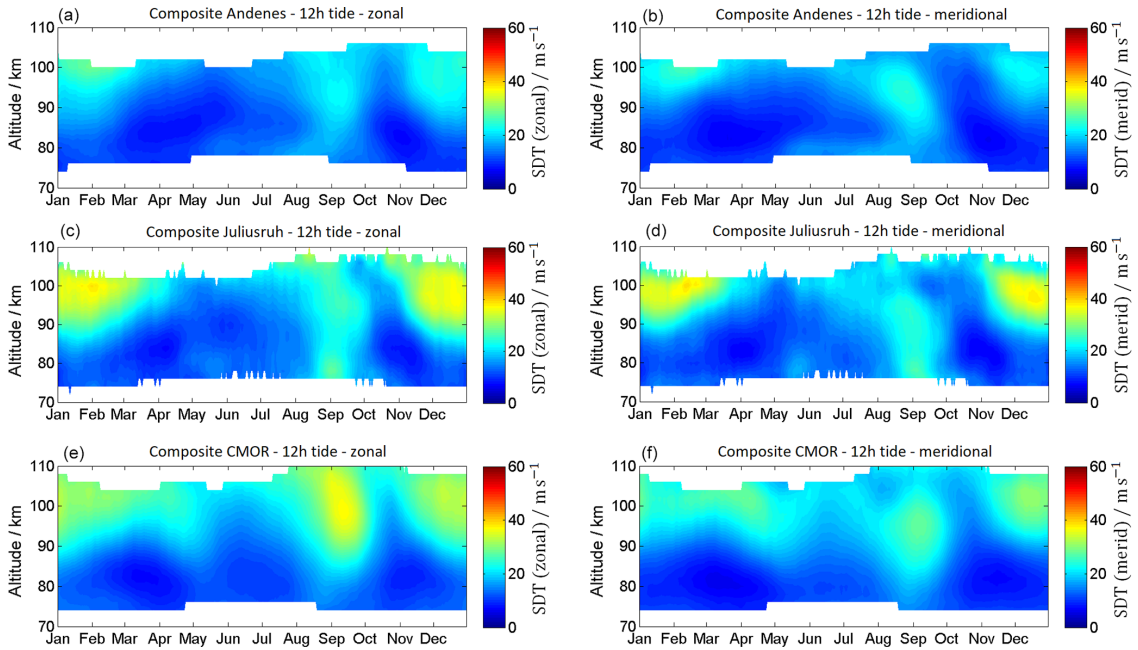


Figure 6.2 Composite for the semidiurnal tidal components. Figure taken from *Wilhelm et al. (2019a)*, Fig. 11.

characteristic seasonal cycle effect for the zonal component. During the summertime, at all locations an 11-year oscillation occurs below 82 km with amplitudes of 3 - 5 m/s. During the winter a response between the heights 84 to 95 km for Andenes and CMOR is shown.

- For the diurnal tidal component, almost no responses of the 11-year oscillation for the locations of Andenes and Juliusruh are pronounced. Only a weak amplitude modulation for Andenes is indicated for the meridional component above 90 km. Overall, at CMOR the oscillation does the most forceful response above 95 km for both diurnal tidal parts. These amplitude modulations arise during summer and for the zonal component from January to April.
- The feedback of the 11-year oscillation for the semidiurnal tides is clearly shown at all three locations. An amplitude of 5 - 8 m/s from October until November in the heights between 84 and 100 km arises at each location. Additionally, a significant response occurs for CMOR for the months January until March above 100 km.

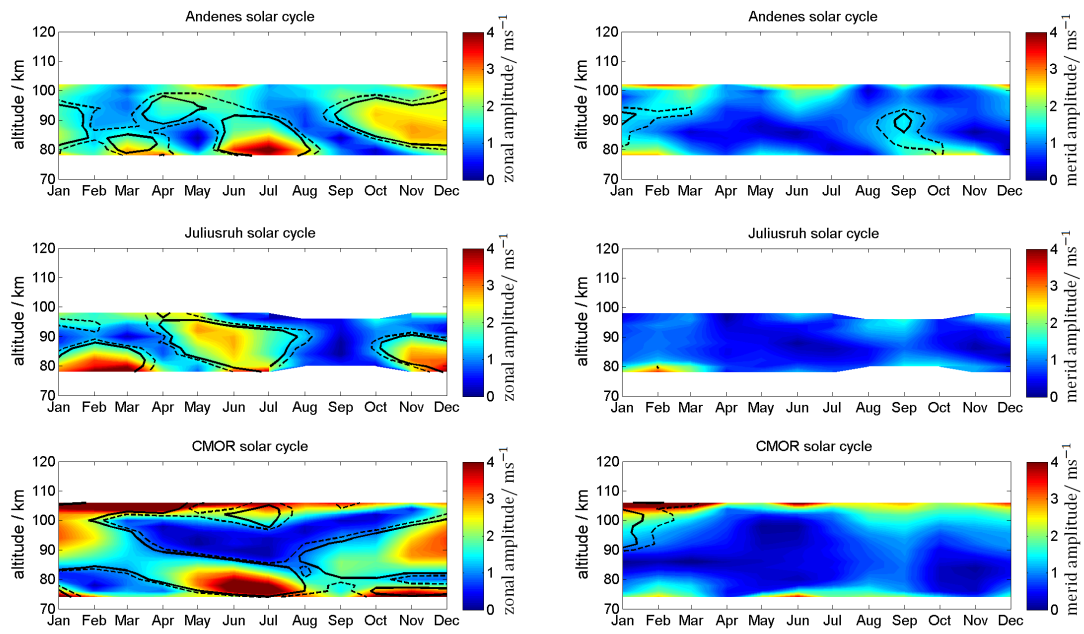


Figure 6.3 Linear change of the solar radiation on the zonal (left) and meridional (right) wind for Andenes (top), Juliusruh (middle), and CMOR (bottom). The solid black lines corresponds to 95% significance, the dashed black lines to the 90% significance. Figure taken from *Wilhelm et al. (2019a)*, Fig 16.

Chapter 7 Connection between fluctuations in the neutral density and the zonal wind

Summary of :

Wilhelm, S., G. Stober, V. Matthias, C. Jacobi, and D. J. Murphy, Connection between the length of day and wind measurements in the mesosphere and lower thermosphere at mid- and high latitudes, *Annales Geophysicae*, 37 (1), 1-14, doi:10.5194/angeo-37-1-2019, 2019

The aim of the study by *Wilhelm et al.* (2019b) was to investigate a connection between changes in the intensity of the solar radiation and the zonal wind, which occurs together with variations in the neutral density. Within a year, the Earth travels around the Sun on an elliptical trajectory which is shown schematically in Figure 7.1. During the northern hemispheric winter, the distance between both celestial bodies is $\sim 3.29\%$ closer than during the northern hemispheric summer. This difference in distance leads according to the inverse square law, to a decreased amount of solar energy entering the Earth's atmosphere during the summer compared to the winter. According to previous studies, as (e.g., *Emmert et al.*, 2010) does an increase of the intensity of solar radiation lead to a rise of the neutral density. This enhancement of the transmitted radiation results in an expansion of the atmosphere. The expansion effect mainly takes place in the thermosphere, where the amount of mass is comparable small and sensitive enough towards changes in the intensity of solar radiation, as well as temperature changes. Later on, *Stober et al.* (2012) showed a connection between changes in the neutral air density to an expansion/shrinking of the atmosphere, and furthermore a strong anti-correlation of neutral air density changes and the zonal wind on short timescales.

Within the present study, a simplified approach concerning the conservation of the angular momentum L was used to describe the connection between changes in the neutral density and the Earth's rotation speed. The conservation of angular momentum includes the atmospheric mass and consequently the atmospheric density. As a result, a theoretical decrease of the rotation speed of up to 4 m/s was estimated for a density increase of 1% between the heights of 70 to 100 km. Due to lack of mesospheric density

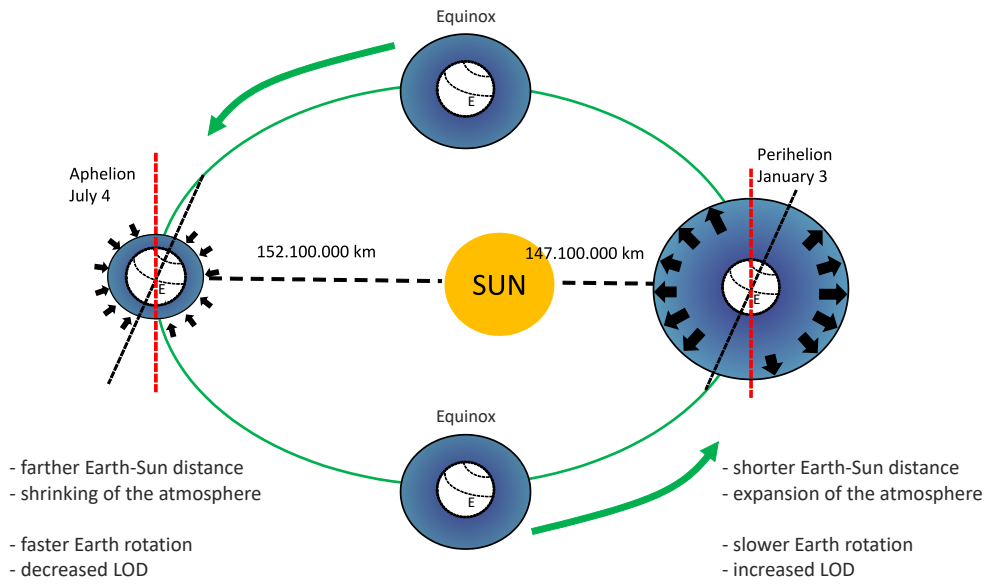


Figure 7.1 Schema of Earth and Sun correlation and the resulting effects on the thickness of the atmosphere and the Earth's rotation velocity. Figure taken from *Wilhelm et al. (2019b)*, Fig. 1.

measurements, direct proof of the effect turns out to be difficult. Therefore, another method was chosen to estimate variations in the rotation speed of the solid Earth, the so-called fluctuation in the length of day (LOD). The LOD is defined as the time difference between 24 h and the measured real time the Earth need for one turnaround. On time scales less than a few years the dominant driver for changes in the Earth's rotation speed is the momentum exchange between the Earth and its atmosphere. The LOD gets measured by the use of a very large baseline interferometry network which determines the rotation speed of the Earth in respect to the stars. The LOD varies in a range of milliseconds per day. An increase of the LOD corresponds to a slower Earth rotation speed.

Additionally on seasonal scales, the influence of the Earth-Sun constellation on mesospheric winds was investigated using wind measurements from four locations. Two of these are located at similar high latitudes for the northern and the southern hemispheres and the other two locations are at northern mid-latitudes. Based on winter and summer mean values, it figured out that during the northern hemispheric winter, where the MLT expands, an increase in the LOD occurs together with a decrease in the zonal wind and that during the northern hemispheric summer the opposite behavior is visible. Figure 7.2 shows the oscillation of the zonal wind and the LOD for two northern (69.3°N, 51.3°N) and one southern (68.6°S) hemispheric locations at 96 km height, with strikingly opposite peaks of both parameters during the northern hemispheric summer,

Chapter 7 Connection between fluctuations in the neutral density and the zonal wind

which occurs due to the typical seasonal wind pattern at these heights.

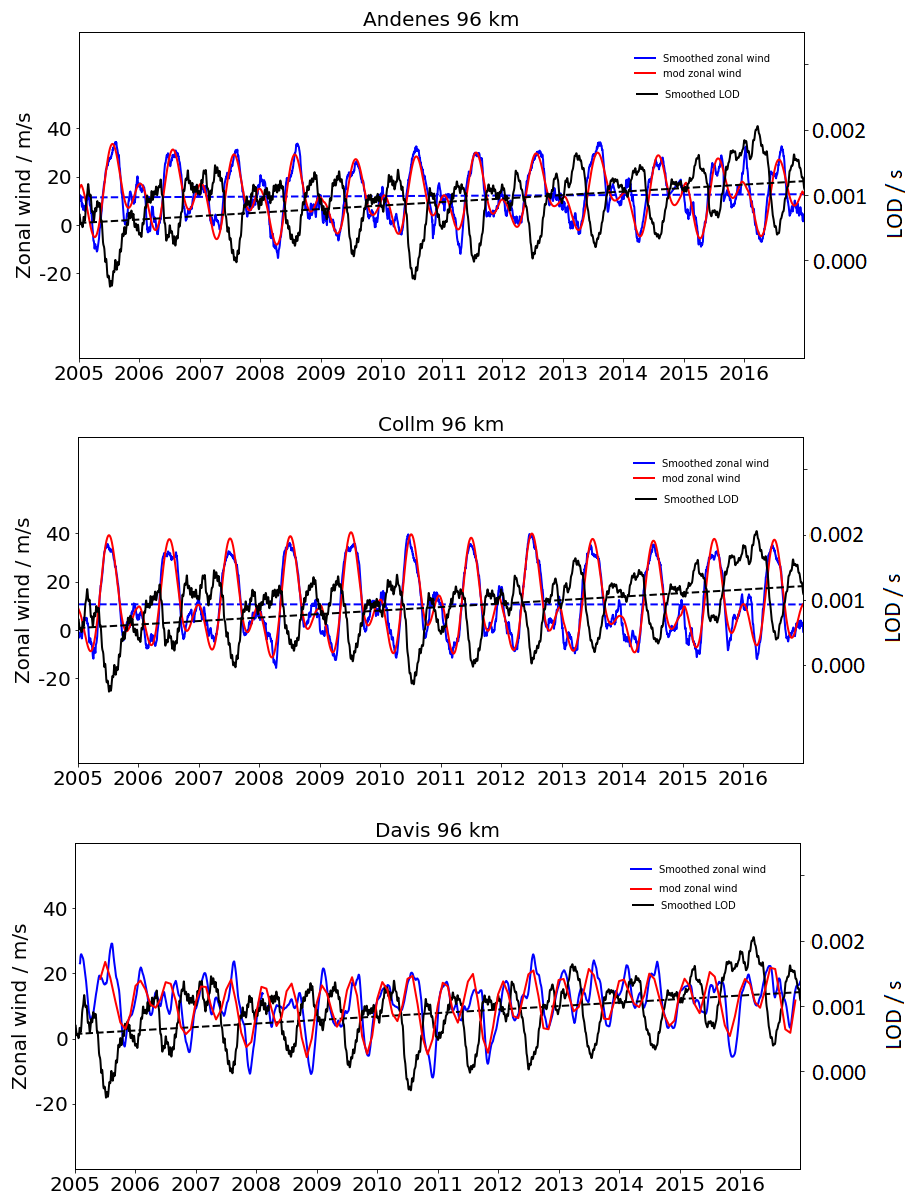


Figure 7.2 Smoothed zonal wind (blue) values based on meteor radar wind data at 96 km and smoothed LOD (black) values. The modulation of the smoothed zonal wind is displayed in red after removing the impact of the solar cycle, whereby the smoothing is stronger as in blue. The dashed lines corresponds to the tendency of the wind/LOD based on linear regression. Figure taken from *Wilhelm et al. (2019b)*, Fig. 7.

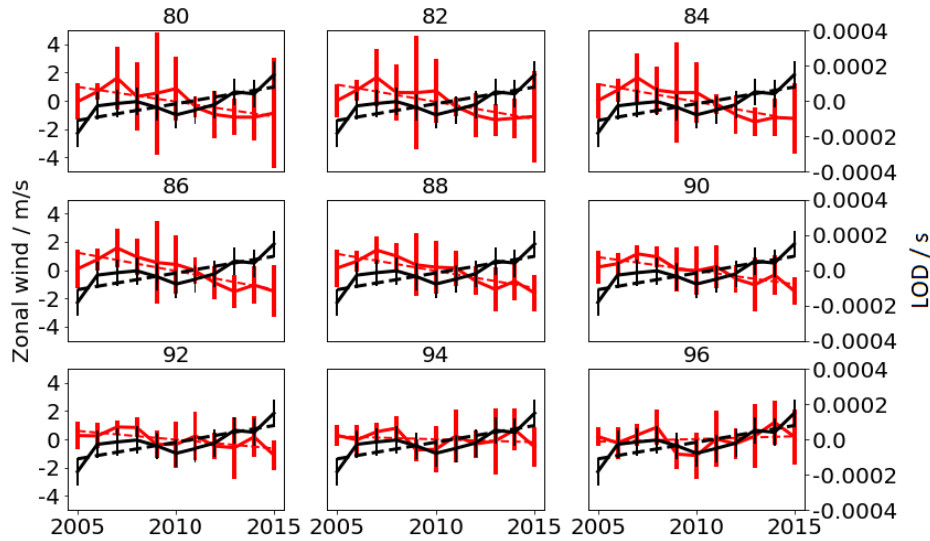


Figure 7.3 Annual mean values for the LOD (black) and the zonal wind (red), for the station Collm (51.3°N), after removing seasonal variations and the solar cycle for the altitudes between 80 and 100 km. The errorbars corresponds to the standard deviation. The dashed lines represents the tendency. Figure taken from *Wilhelm et al. (2019b)*, Fig. 9.

Further, after removing seasonal fluctuations and the influence of the 11-year solar cycle, the zonal wind and the LOD still show a connection. Figure 7.3 displays, based on annual timescales, the occurrence of an increase in the LOD together with an enhancement of the westward directed wind between the years 2005 until 2015. It needs to be mentioned that, based on the findings within this study, a connection between the LOD and the zonal wind exists, which can be explained due to the variability of the atmospheric density, but within the MLT stronger geophysical effects exists, which are responsible for the typical wind pattern, as e.g., gravity waves. Furthermore, on shorter time scales a connection between the wind and the LOD cannot be figured out, because the LOD consists of oscillations with at least a 6-month period, which needs further studies to resolve the superpositions of both parameters.

Chapter 8 Summary and outlook

In this cumulative thesis, measurements of mesospheric and lower thermospheric winds and waves with the focus on long-term changes are analyzed. Primary, meteor radars are used within this study. These systems use for the wind determination ionized plasma of meteor trails. Additionally, for one part of the thesis winds from the medium frequency radar SAURA are used, which are based on changes of the atmospheric electron density.

Comparing measurements of the same periods, but based on different instruments, often result in a similar seasonal pattern, but can differ strongly in magnitude. To overcome the issue, in the study of *Wilhelm et al.* (2017), a comparison for the very high-frequency specular meteor radar system (MR, 32.55 MHz) and the medium frequency radar (MF, 3.17 MHz) was done. The aim of this study was on the one side to find potential biases between the systems, and on the other side to combine both data sets. These radar systems are located close by and can measure winds at comparable heights, allowing only a comparison at this location. Another additional prerequisite for the estimation of both radar system is that the wind determination was done with the same approach, a modified version of the so-called all-sky-fit method (*Hocking and Thayaparan, 1997; Hocking et al., 2001; Stober et al., 2017*). The comparison between both systems was made for the period 2004 - 2014, in an altitude range (78 - 100 km) that both systems can cover. It results that below 92 km the wind and tides of the MF radar show a difference in the magnitude of 10 - 60%. Above 92 km opposite mean wind pattern occur during the summer in the meridional component and a significant difference for the zonal component is recognized. Similar results were shown in earlier studies. Based on the mean wind value, a correction factor was estimated which allows adapting mean wind values of one system to the other. Further, it was figured out that the mean values for the whole year differ significantly above 92 km. As a possible reason for the bias between both systems is an a difference between the nominal and true beam pointing for the MF system due to the layering of electron density with altitude. This pointing difference varies regarding season and increases in value with height. Based on this result, *Renkowitz et al.* (2018) implemented an angular correction for the MF system to overcome this issue. Even if the values of the correction factor can only be used for these two systems, the method for the determination is also applicable for other measuring instruments.

Not only the use of different instruments can lead to various geophysical measurements, but they are also highly dependent on their measurement time, region and position. In the study of *Wilhelm et al.* (2019a), three meteor radars at different locati-

ons provide long-term observations between the years 2002 and 2018. The observations were done for winds, tides, kinetic gravity wave energy, and kinetic planetary wave energy. For the locations Andenes (Norway), Juliusruh (Germany) and Tavistock (Canada) the parameters were determined using the same wind retrieval approach. The result is shortly summarized by: The climatologies of the mean wind show, in general, a similar pattern for each location. Nevertheless, latitudinal dependencies are visible for several features. The locations differ concerning altitude, and season for long-term changes of several parameters. Annual winds for Andenes show an overall tendency towards the south-west with variations of up to 3 m/s, while at the mid-latitude locations nearly no changes are observed. The seasonal pattern of the diurnal tide shows almost no significant tendency, while the long-term measurements of the dominant semidiurnal tide show latitudinally dependent changes. Furthermore, kinetic energies of planetary waves and gravity waves were estimated. During the winter, strong planetary wave activities taking place for years with a major stratospheric warming. Gravity wave activities show a distinct seasonal pattern with maximum energies during the winter and later summer above 90 km and a second, but weaker, maximum during summer below 80 km. Finally, the influence of an 11-year oscillation on the winds and tides was investigated. Our results reveal that the mean winds and the semidiurnal tides exhibit a clear 11-year response at the mid- and high latitudes. It turns out that long-term measurements and tendencies of several parameters differ strongly regarding the observed altitude, the season, and the location. It also shows the complexity of tendency estimations and the resulting need to investigate and compare the results with global models.

Several reasons can be named to describe variations in the MLT seasonal wind pattern. In this thesis, seasonal variations of the zonal wind due to changes in the neutral density are investigated. Within a year, the neutral density of the MLT is highly influenced by the Earth's movement around the Sun. During northern hemispheric winter, the distance between the Earth and the Sun is closer than during the northern hemispheric summer. This leads, on a global scale, to an enhancement of incoming solar radiation and therefore to an expansion of radiative sensitive heights (mesosphere, thermosphere, ionosphere). With the background of the conservation of angular momentum, this further leads to a slower angular rotation of these atmospheric heights. Within the MLT, direct long-term density measurements over several years are scarce goods. Therefore, daily data of the Earth's rotation velocity is taken to find a long-term connection between the prevailing zonal wind and density fluctuations in the MLT. The time, the Earth needs for one full turnaround, also varies within a year. It takes longer during the northern hemispheric winter, and it goes faster during the northern hemispheric summer, which fits the expansion/shrinking of the atmosphere. In the study of *Wilhelm et al. (2019b)*, a connection between the winds above 90 km and the length of a day is found. It is essential to mention that these findings only show a connection between the length of a day and the zonal wind, based on the variations of the neutral density. These results do not explain on how strong a possible effect is between the parameters. Other physical processes have a much stronger impact on the typical seasonal wind pattern, as e.g., the chemical composition of the atmosphere, the propagation of gravity waves. Nevertheless, higher eastward directed wind values

Chapter 8 Summary and outlook

occur during the summer together with a faster Earth's rotation. This connection is taking place in the upper atmosphere, where the amount of mass is small to be sensitive enough to changes in solar radiation, as well as to temperature changes. A connection between the length of a day and the zonal wind is found on time scales of at least 1 year.

In future the results presented in this thesis can be used to improve the understanding of long-term observations in the MLT. This includes the spatial distribution of winds and waves in the MLT, but also coupling processes to higher and lower atmospheric layers. A first good way in that direction is the further technical development of the radar network system MMARIA, which allows to observe a larger horizontal area by using several meteor radars (e.g., *Stober and Chau, 2015; Stober et al., 2018; Chau et al., 2019*). In general, the outcome of this thesis can be used to improve the quality of models, which partly struggle with the estimation of the seasonal wind pattern in the lower thermosphere and also with the long-term estimations. An intense research with the use of global models, regarding geophysical differences, needs to be done to explain the latitudinal/height/seasonal difference in the long-term changes. During each parts of this thesis questions occur, which can be addressed in the future:

- *Wilhelm et al. (2017)* :
 - * Comparison of MF and MR wind data, after optimizing the MF winds by correcting the angle of arrival *Renkowitz et al. (2018)*.
 - * The method of data set merging can be used for other instruments, which are located at the same station.
- *Wilhelm et al. (2019a)* :
 - * For the long-term changes occur some strong latitudinal differences, which needs to be investigated.
 - * In the climatology of the semidiurnal zonal tide occur for the location CMOR a strong enhancement during the spring, which is not seen in the semidiurnal component, neither in the meridional diurnal tidal component.
 - * Spatial connection of the long-term changes between each location.
 - * Comparison of the observations with global circulation models.
- *Wilhelm et al. (2019b)* :
 - * Closer investigation of the connection between the length of a day and the zonal wind when global long-term density data are available.
 - * Dissolve the superposition of the length of day into oscillations shorter than a year and compare connection on global basis.

Bibliography

- Akmaev, A., R., V. I. Fomichev, and X. Zhu, Impact of middle-atmospheric composition changes on greenhouse cooling in the upper atmosphere, *Journal of Atmospheric and Solar-Terrestrial Physics*, 68(17), doi:10.1016/j.jastp.2006.03.008, 2006.
- Andrews, D. G., J. R. Holton, and C. B. Leovy, *Middle atmosphere dynamics*, Academic Press, New York, NY, USA, doi:doi.org/10.1002/qj.49711548612, 489 pp, 1987.
- Baggaley, J., W., *Meteors in the Earth's Atmosphere*, chap. Radar Observations, Cambridge University Press, 2002.
- Baumgarten, K., and G. Stober, On the evaluation of the phase relation between temperature and wind tides based on ground-based measurements and reanalysis data in the middle atmosphere, *Ann. Geophys. Discuss.*, doi:10.5194/angeo-2019-25, 2019.
- Baumgarten, K., M. Gerding, G. Baumgarten, and F.-J. Lübken, Temporal variability of tidal and gravity waves during a record long 10-day continuous lidar sounding, *Atmospheric Chemistry and Physics*, 18, 371–384, doi:10.5194/acp-18-371-2018, 2018.
- Becker, E., Dynamical control of the middle atmosphere, *Space Science Review*, pp. 283–314, doi:10.1007/s11214-011-9841-5, 2012.
- Becker, E., and S. L. Vadas, Secondary gravity waves in the winter mesosphere: results from a high-resolution global circulation model, *Journal of Geophysical Research*, 123, doi:10.1002/2017JD027460, 2018.
- Charney, G., J., and G. Drazin, P., Propagation of planetary scale disturbances from the lower into the upper atmosphere, *Journal of Geophysical Research*, 66(1), doi:10.1029/JZ066i001p00083, 1961.
- Chau, L., J., M. Urco, J., P. Vierinen, J., A. Volz, R., M. Clahsen, N. Pfeffer, and J. Trautner, Novel specular meteor radar system using coherent MIMO techniques to study the mesosphere and lower thermosphere, *Atmospheric Measurements Techniques*, 12, 2113–2127, doi:10.5194/amt-12-2113-2019, 2019.
- Conte, F., J., L. Chau, J., I. Laskar, F., G. Stober, H. Schmidt, and P. Brown, Semidiurnal solar tide differences between fall and spring transition time in the northern hemisphere, *Annales Geophysicae*, 36, 999–1008, doi:10.5194/angeo-36-999-2018, 2018.

Bibliography

- Davis, R. N., J. Du, A. K. Smith, W. E. Ward, and N. J. Mitchell, The diurnal and semidiurnal tides over Ascension Island (8°S, 14°W) and their interaction with the stratospheric quasi-biennial oscillation: studies with meteor radar, eCMAM and WACCM, *Atmospheric Chemistry and Physics*, 13(18), 9543–9564, doi:10.5194/acp-13-9543-2013, 2013.
- Dickey, O., J., L. Marcus, S., R. Hide, M. Eubanks, T., and H. Boggs, D., Angular momentum exchange among the solid Earth, atmosphere, and oceans: A case study of the 1982 - 1983 El Nino event., *Journal of geophysical research*, 99(812), 23, 921–23,937, 1994.
- Driscoll, S., The Earth's Atmospheric Angular Momentum budget and its representation in reanalysis observation data and climate models, Ph.D. thesis, University of Reading, 2010.
- Eckermann, S. D., D. Broutman, J. Ma, J. D. Doyle, P. D. Pautet, M. J. Taylor, K. Bosser, B. P. Williams, D. C. Fritts, and R. B. Smith, Dynamics of orographic gravity waves observed in the mesosphere over the Auckland Islands during the Deep Propagation Gravity Wave Experiment (DEEPWAVE), *Journal of Atmospheric Science*, 73, 3855–3876, doi:10.1175/JAS-D-16-0059.1, 2016.
- Egger, J., K. Weickmann, and K.-P. Hoinka, Angular momentum in the global atmospheric circulation, *Reviews of Geophysics*, 45(4), doi:10.1029/2006RG000213, rG4007, 2007.
- Emmert, J. T., Altitude and solar activity dependence of 1967-2005 thermospheric density trends derived from orbital drag, *Journal of geophysical research: space physics*, 120, 2940–2950, doi:10.1002/2015JA021047., 2015.
- Emmert, J. T., J. L. Lean, and J. M. Picone, Record-low thermospheric density during the 2008 solar minimum, *Geophysical Research Letters*, 37(12), doi:10.1029/2010GL043671, 112102, 2010.
- Emmert, T., J., M. Picone, J., L. Lean, J., and H. Knowles, S., Global change in the thermosphere: Compelling evidence of a secular decrease in density, *Journal of geophysical research*, 109(A02301), doi:10.1029/2003JA010176, 2004.
- Eubanks, T., J. Steppe, and J. Dickey, *The Earth's Rotation and Reference Frame for Geodesy and Geodynamics*, chap. The atmospheric excitation of rapid polar motions., Springer, 1988.
- Fiedler, J., and G. Baumgarten, Solar and lunar tides in noctilucent clouds as determined by ground-based lidar, *Atmospheric Chemistry and Physics*, 18, 16,051–16,061, doi:10.5194/acp-18-16051-2018, 2018.
- Fomichev, I., V., E. Ward, W., R. Beagley, S., C. McLandress, C. McConnel, J., A. McFarlane, N., and G. Shepherd, T., Extended Canadian Middle Atmosphere Model: Zonal-mean climatology and physical parametrizations, *Journal of Geophysical Research*, 107(D10), doi:10.1029/2001JD000479, 2002.

- Forbes, J., *Tidal and Planetary Waves, Geophysical Monograph Series*, vol. 87, The Upper Mesosphere and Lower Thermosphere: A Review of Experiment and Theory ed., American Geophysical Union, doi:10.1029/GM087p0067, 1995.
- France, A., J. L. Harvey, V. E. Randall, C. M. H. Hitchmann, and J. Schwatz, M., A climatology of stratopause temperature and height in the polar vortex and anticyclones, *Journal of Geophysical Research*, 117, D06,116, doi:10.1029/2011JD016893, 2012.
- Franke, S. J., X. Chu, Z. Liu, A., and K. Hocking, W., Comparison of meteor radar and Na doppler lidar measurements of winds in the mesopause region above Maui, Hawaii, *Journal of Geophysical Research*, 110, doi:10.1029/2003JD004486, 2005.
- Fritts, C., D., and J. Alexander, M., Gravity wave dynamics and effects in the middle atmosphere, *Reviews of Geophysics*, 41(1)(1003), doi:10.1029/2001RG000106, 2003.
- Fukao, S., and K. Hamazu, *Radar for Meteorological and Atmospheric Observations*, 1 ed., Springer Japan, doi:10.1007/978-4-431-54334-3, ISBN 978-4-431-54334-3, 2014.
- Geißler, C., and C. Jacobi, Mesospheric wind and temperature trends simulated with MUAM, *Meteorologische Arbeiten aus Leipzig*, 22(55.2017 = 22.2017), ISBN: 978-3-9814401-3-3, 2017.
- Gudadze, N., G. Stober, and J. L. Chau, Can VHF radars at polar latitudes measure mean vertical winds in the presence of PMSE?, *Atmospheric Chemistry and Physics*, 19, 4485–4497, doi:10.5194/acp-19-4485-2019, 2019.
- Hagan, M. E., and J. M. Forbes, Migrating and nonmigrating diurnal tides in the middle and upper atmosphere excited by tropospheric latent heat release, *Journal of geophysical research*, 107(D24), doi:10.1029/2001JD001236, 2002.
- Hall, C. M., T. Aso, M. Tsutsumi, S. Nozawa, A. H. Manson, and C. E. Meek, A comparison of mesosphere and lower thermosphere neutral winds as determined by meteor and medium-frequency radar at 70°N, *Radio Science*, 40(4), doi:10.1029/2004RS003102, rS4001, 2005.
- Hocking, K., W., J. Röttger, D. Palmer, R., T. Sato, and B. Chilson, P., *Atmospheric Radar: Application and Science of MST Radars in the Earth's Mesosphere, Stratosphere, Troposphere, and Weakly Ionized Regions*, Cambridge University Press, doi:10.1017/9781316556115, 2016.
- Hocking, W. K., and T. Thayaparan, Simultaneous and colocated observation of winds and tides by MF and meteor radars over London, Canada (43°N, 81°W), during 1994–1996, *Radio Science*, 32(2), 833–865, doi:10.1029/96RS03467, 1997.
- Hocking, W. K., B. Fuller, and B. Vandeeper, Realtime determination of meteor-related parameters utilizing modern digital technology, *Journal of Atmospheric and Solar-Terrestrial Physics*, 69(2-3), 155–169, doi:10.1016/S1364-6826(00)00138-3, 2001.

Bibliography

- Hoffmann, P., E. Becker, W. Singer, and M. Placke, Seasonal variation of mesospheric waves at northern middle and high latitudes, *Journal of Atmospheric and Solar-Terrestrial Physics*, 72(14-15), 1068–1079, doi:10.1016/j.jastp.2010.07.002, 2010.
- Hoffmann, P., M. Rapp, W. Singer, and D. Keuer, Trends of mesospheric gravity waves at northern middle latitudes during summer, *Journal of geophysical research*, 116, doi:10.1029/2011JD015717, 2011.
- Holton, J. R., and J. Alexander, M., *The Role of Waves in the Transport Circulation of the Middle Atmosphere, Geophysical Monograph Series*, vol. 123, Atmospheric Science Across the Stratopause ed., American Geophysical Union, doi:10.1029/GM123p0021, 2000.
- Holton, R., J., *An introduction to dynamic meteorology, International Geophysics*, vol. 88, 4. ed., Elsevier Academic Press, iISBN: 0-12-354015-1, 1992.
- Hysell, D., D. Fritts, B. Laughman, and J. L. Chau, Gravity wave-induced ionospheric irregularities in the postsunset equatorial valley region, *Journal of Geophysical Research*, 122(11), 579–590, doi:doi.org/10.1002/2017JA024514, 2017.
- Jacobi, C., Meteor radar measurements of mean winds and tides over Collm (51.3°N, 13°E) and comparison with LF drift measurements 2005–2007, *Adv. Radio Sci.*, 9, 335–341, doi:10.5194/ars-9-335-2011, 2011.
- Jacobi, C., 6 year mean prevailing winds and tides measured by VHF meteor radar over Collm (51.3°N, 13.0°E), *Journal of Atmospheric and Solar-Terrestrial Physics*, 78-79, 8 – 18, doi:10.1016/j.jastp.2011.04.010, structure and Dynamics of Mesosphere and Lower Thermosphere, 2012.
- Jacobi, C., M. Lange, D. Kürschner, H. Manson, A., and E. Meek, C., A Long-Term Comparison of Saskatoon MF Radar and Collm LF D1 Mesosphere-Lower Thermosphere Wind Measurements, *Phys. Chem. Earth*, 26(6), 419–424, doi:10.1016/S1464-1917(01)00023-X, 2001.
- Jacobi, C., P. Hoffmann, and D. Kürschner, Trends in MLT region winds and planetary waves, Collm (52°N, 15°E), *Annales Geophysicae*, 26, 1221–1232, doi:10.5194/angeo-26-1221-2008, 2008.
- Kawahara, D., T., S. Nozawa, N. Saito, T. Kawabata, T. Tsuda, T., and S. Wada, Sodium temperature/wind lidar based on laser-diode-pumped Nd:YAG laser deployed at Tromsø, Norway (69.6°N, 19.2°E), *Optics express*, 25(12), doi:10.1364/OE.25.00A491, 2017.
- Kelly, M., *The Earth's Ionosphere*, vol. 96, 2nd ed., Academic Press, iISBN: 9780120884254, 2009.
- Larsen, M. F., Wind and shears in the mesosphere and lower thermosphere: Results from four decades of chemical release wind measurements, *Journal of Geophysical Research*, 107(A8), 1215, doi:10.1029/2001JA000218, 2002.

- Laštovička, J., A. Akmaev, R., G. Beig, J. Bremer, J. T. Emmert, C. Jacobi, J. Jarvis, M., G. Nedoluha, I. Portnyagin, Y., and T. Ulich, Emerging pattern of global change in the upper atmosphere and ionosphere, *Annales Geophysicae*, *26*, 1255–1268, doi:10.5194/angeo-26-1255-2008, 2008.
- Laštovička, J., C. Solomon, S., and L. Qian, Trends in the neutral and ionized upper atmosphere, *Space Science Review*, *168*, 113–145, doi:10.1007/s11214-011-9799-3, 2012.
- Li, T., C. Ban, X. Fang, J. Li, Z. Wu, W. Feng, M. C. Plane, J., J. Xiong, R. Marsh, D., J. Mills, M., and X. Dou, Climatology of mesopause region nocturnal temperature, zonal wind and sodium density observed by sodium lidar over Hefei, China (32°N,117°E), *Atmospheric Chemistry and Physics*, *18*, doi:10.5194/acp-18-11683-2018, 2018.
- Lindzen, R. S., and S. Chapman, Atmospheric tides, *Space Science Review*, *10*(1), 3–188, 1969.
- Liu, Z., A., K. Hocking, W., S. J. Franke, and T. Thayaparan, Comparison of Na lidar and meteor wind measurements at Starfire Optical Range, NM, USA, *Journal of Atmospheric and Solar-Terrestrial Physics*, *64*, 31–40, 2002.
- Lübken, F.-J., G. Baumgarten, J. Fiedler, M. Gerding, J. Höffner, and U. Berger, Seasonal and latitudinal variation of noctilucent cloud altitudes, *Geophysical Research Letters*, *35*, doi:10.1029/2007GL032281, 2008.
- Lübken, F.-J., U. Berger, and G. Baumgarten, Temperature trends in the midlatitude summer mesosphere, *Journal of geophysical research*, *118*(13), doi:10.1002/2013JD020576, 2013.
- Lukianova, R., A. Kozlovsky, and M. Lester, Climatology and inter-annual variability of the polar mesospheric winds inferred from meteor radar observations over Sodankylä (67N, 23E) during solar cycle 24, *Journal of atmospheric and solar-terrestrial physics*, *171*, 241–249, doi:10.1016/j.jastp.2017.06.005, 2018.
- Madden, A., R., and P. Speth, Estimates of atmospheric angular momentum, friction, and mountain torques during 1987-1988, *Journal of the atmospheric sciences*, *52*(21), doi:10.1175/1520-0469(1995)052<3681:EOAAMF>2.0.CO;2, 1995.
- Malberg, H., *Meteorologie und Klimatologie*, 5. ed., Springer, doi:10.1007/978-3-540-37222-6, ISBN: 9783540372196, 2007.
- Manson, A. H., C. E. Meek, C. M. Hall, S. Nozawa, N. J. Mitchell, D. Pancheva, W. Singer, and P. Hoffmann, Mesopause dynamics from the scandinavian triangle of radars within the PSMOS-DATAR Project, *Annales Geophysicae*, *22*(2), 367–386, doi:10.5194/angeo-22-367-2004, 2004.
- Marcos, A., F., O. Wise, J., J. Kendra, M., J. Gossbard, N., and R. Bowman, B., Detection of long-term decrease in thermospheric neutral density, *Geophys. Res. Lett.*, *32*(L04103), doi:10.1029/2004GL021269, 2005.

Bibliography

- Marsh, R., D., R. Garcia, R., E. Kinnison, D., A. Boville, B., F. Sassi, C. Solomon, S., and K. Matthes, Modeling the whole atmosphere response to solar cycle changes in radiative and geomagnetic forcing, *Journal of geophysical research*, *112*, doi:10.1029/2006JD008306, 2007.
- Masson-Delmotte, V., P. Zhai, H.-O. Pörtner, D. Roberts, J. Skea, P. Shukla, A. Pirani, W. Moufouma-Okia, C. Péan, R. Pidcock, S. Connors, J. Matthews, Y. Chen, X. Zhou, M. Gomis, E. Lonnoy, T. Maycock, M. Tignor, and W. T., IPCC, 2018: Summary for Policymakers, *World Meteorological Organization, Geneva, Switzerland*, p. 32 pp., 2018.
- Matthias, V., and M. Ern, On the origin of the mesospheric quasi-stationary planetary waves in the unusual Arctic winter 2015/16, *Atmospheric Chemistry and Physics*, *18*, 4803–4815, doi:10.5194/acp-18-4803-2018, 2018.
- Matthias, V., P. Hoffmann, A. Manson, C. Meek, G. Stober, P. Brown, and M. Rapp, The impact of planetary waves on the latitudinal displacement of sudden stratospheric warmings, *Annales Geophysicae*, *31*, 1397–1415, doi:10.5194/angeo-31-1397-2013, 2013.
- McKinley, W. R., D., *Meteor Science and Engineering*, McGraw-Hill Book Company, Inc., 1961.
- Müllemann, A., and F.-J. Lübken, Horizontal winds in the mesosphere at high latitudes, *Advances in Space Research*, *35*, doi:10.1016/j.asr.2004.11.014, 2004.
- Oberheide, J., M. E. Hagan, R. G. Roble, and D. Offermann, Sources of nonmigrating tides in the tropical middle atmosphere, *Journal of Geophysical Research*, *107*(D21), doi:10.1029/2002JD002220, 2002.
- Placke, Gravity waves and momentum fluxes in the mesosphere and lower thermosphere, Ph.D. thesis, University of Rostock, iAP Nr. 36/2014 ISSN 1615-8083, 2014.
- Plane, J. M. C., Cosmic dust in the Earth's atmosphere, *Chem Soc Rev*, *41*, doi:10.1039/c2cs35132c, 2012.
- Pokhotelov, D., E. Becker, G. Stober, and J. L. Chau, Seasonal variability of atmospheric tides in the mesosphere and lower thermosphere: meteor radar data and simulations, *Annales Geophysicae*, *36*(3), 825–830, doi:10.5194/angeo-36-825-2018, 2018.
- Qian, L., J. Laštovička, R. G. Roble, and C. Solomon, S., Progress in observations and simulations of global change in the upper atmosphere, *Journal of Geophysical Research*, *116*(A00H03), doi:10.1029/2010JA016317, 2011.
- Renkowitz, T., M. Tsutsumi, F. I. Laskar, J. L. Chau, and R. Latteck, On the role of anisotropic MF/HF scattering in mesospheric wind estimation, *Earth, Planets and Space*, *70*(1), 158, doi:10.1186/s40623-018-0927-0, 2018.

- Sato, K., T. Kinoshita, and K. Okamoto, A new method to estimate three-dimensional residual-mean circulation in the middle atmosphere and its application to gravity wave-resolving general circulation model data, *Journal of atmospheric science*, *70*, doi:10.1175/JAS-D-12-0352.1, 2013.
- Schmidt, F., G. Baumgarten, U. Berger, J. Fiedler, and F.-J. Lübken, Local time dependence of polar mesospheric clouds: a model study, *Atmospheric Chemistry and Physics*, *18*, 8893–8908, doi:10.5194/acp-18-8893-2018, 2018.
- Schmidt, H., G. P. Brasseur, M. Charron, E. Manzini, M. A. Giorgetta, T. Diehl, V. I. Fomichev, D. Kinnison, D. Marsh, and S. Walters, The HAMMONIA chemistry climate model: Sensitivity of the mesopause region to the 11-year solar cycle and CO₂ doubling, *Journal of Climate*, *19*(16), 3903–3931, doi:10.1175/JCLI3829.1, 2006.
- Schminder, R., and D. Kürschner, Permanent monitoring of the upper mesosphere and lower thermosphere wind fields (prevailing and semidiurnal tidal components) obtained from LF D1 measurements in 1991 at the Collm Geophysical Observatory, *Journal of Atmospheric and Terrestrial Physics*, *56*(10), 1263 – 1269, doi:10.1016/0021-9169(94)90064-7, 1994.
- Schult, C., G. Stober, L. Chau, J., and R. Latteck, Determination of meteor-head echo trajectories using interferometric capabilities of MAARSY, *Annales Geophysicae*, *31*, 1843–1851, doi:doi:10.5194/angeo-31-1843-2013, 2013.
- Schult, C., P. Brown, P. Pokorný, G. Stober, and L. Chau, J., A meteoroid stream survey using meteor head echo observations from the Middle Atmosphere ALOMAR Radar System (MAARSY), *Icarus*, *309*, 177–186, doi:10.1016/j.icarus.2018.02.032, 2018.
- Shepherd, G., T., Transport in the middle atmosphere, *Journal of meteorological society of Japan*, *85B*, 165–191, doi:doi.org/10.2151/jmsj.85B.165, 2007.
- Singer, W., R. Latteck, and D. Holdsworth, A new narrow beam Doppler radar at 3 MHz for studies of the high-latitude middle atmosphere, *Advances in Space Research*, *41*(9), 1488–1494, doi:10.1016/j.asr.2007.10.006, 2008.
- Smith, A. K., Global dynamics of the MLT, *Surv Geophys*, *33*, 1177–1230, doi:10.1007/s10712-012-9196-9, 2012.
- Stober, G., and J. L. Chau, A multistatic and multifrequency novel approach for specular meteor radars to improve wind measurements in the MLT region, *Radio Science*, *50*(5), 431–442, doi:10.1002/2014RS005591, 2015.
- Stober, G., and C. Jacobi, Meteor head velocity determination, *Wiss. Mitteil. Inst. f. Meteorol. Univ. Leipzig*, *41*, 2007.
- Stober, G., R. Latteck, M. Rapp, W. Singer, and M. Zecha, Maarsy – the new MST radar on Andøya: first results of spaced antenna and doppler measurements of atmospheric winds in the troposphere and mesosphere using a partial array, *Advances in Radio Science*, *10*, 291–298, doi:10.5194/ars-10-291-2012, 2012.

Bibliography

- Stober, G., V. Matthias, P. Brown, and J. L. Chau, Neutral density variation from specular meteor echo observations spanning one solar cycle, *Geophysical Research Letters*, *41*, 6919–6925, doi:10.1002/2014GL061273, 2014.
- Stober, G., V. Matthias, C. Jacobi, S. Wilhelm, J. Höffner, and J. L. Chau, Exceptionally strong summer-like zonal wind reversal in the upper mesosphere during winter 2015/16, *Annales Geophysicae*, *35*, 711–720, doi:10.5194/angeo-35-711-2017, 2017.
- Stober, G., J. L. Chau, J. Vierinen, C. Jacobi, and S. Wilhelm, Retrieving horizontal resolved wind field using multi-static meteor radar observations, *Atmospheric Measurement Techniques*, *11*, 4891–4907, doi:10.5194/amt-11-4891-2018, 2018.
- Thomas, E., G., Global change in the mesosphere-lower thermosphere region: has it already arrived?, *Journal of Atmospheric and Terrestrial Physics*, *58*(14), 1629–1656, doi:10.1016/0021-9169(96)00008-6, 1996.
- Trenberth, E., K., and J. Guillemot, C., The total mass of the atmosphere, *Journal of Geophysical Research: Atmospheres*, *99*(D11), 23,079–23,088, doi:10.1029/94JD02043, 1994.
- Tsuda, T., M. Nishida, C. Rocken, and H. Ware, R., A global morphology of gravity wave activity in the stratosphere revealed by the GPS occultation data (GPS/MET), *Journal of geophysical research*, *105*(D6), 7257 – 7273, doi:10.1029/1999JD901005, 2000.
- Volland, H., Atmospheric effects on the Earth’s rotation, Proceedings of a Workshop held at the Center for Interdisciplinary Research (ZiF), in *Earth’s Rotation from Eons to Days*, edited by P. Brosche and J. Suendermann, pp. 127–140, Springer-Verlag, 1988.
- Walterscheid, L., R., Solar cycle effects on the upper atmosphere: Implications for satellite drag, *Journal of spacecraft and rockets*, *26*(6), 439–444, doi:10.2514/3.26089, 1989.
- Westman, A., G. Wannberg, and A. Pellinen-Wannberg, Meteor head echo altitude distributions and the height cutoff effect studied with the EISCAT HPLA UHF and VHF , *Annales Geophysicae*, *22*, doi:1432-0576/ag/2004-22-1575, 2004.
- Wilhelm, S., G. Stober, and J. L. Chau, A comparison of 11-year mesospheric and lower thermospheric winds determined by meteor and MF radar at 69°N, *Annales Geophysicae*, *35*, 893–906, doi:10.5194/angeo-35-893-2017, 2017.
- Wilhelm, S., G. Stober, and P. Brown, Climatologies and long-term changes of mesospheric wind and wave measurements based on radar observations at high and mid-latitudes, *Annales Geophysicae*, *37*, 851–875, doi:doi.org/10.5194/angeo-37-851-2019, 2019a.
- Wilhelm, S., G. Stober, V. Matthias, C. Jacobi, and D. J. Murphy, Connection between the length of day and wind measurements in the mesosphere and lower thermosphere at mid- and high latitudes, *Annales Geophysicae*, *37*(1), 1–14, doi:10.5194/angeo-37-1-2019, 2019b.

Bibliography

- Xu, J., H.-L. Liu, W. Yuan, K. Smith, A., G. Roble, R., J. Mertens, C., M. Russel III, J., and G. Mlynchak, M., Mesopause structure from thermosphere, ionosphere, mesosphere, energetics, and dynamics (TIMED)/ sounding of the atmosphere using broadband emission radiometry (SABER) observations, *Journal of Geophysical Research*, *112*, D09,102, doi:10.1029/2006JD007711, 2007.
- Yuan, T., C.-Y. She, A. Krueger, D., F. Sassi, R. Garcia, G. Roble, R., H.-L. Liu, and H. Schmidt, Climatology of mesopause region temperature, zonal wind, and meridional wind over Fort Collins, Colorado (41°N, 105°W), and comparison with model simulations, *Journal of geophysical research*, *113*, doi:10.1029/2007JD008697, 2008.
- Yuan, W., J. Xu, R. Ma, Q. Wu, Y. Jiang, G., H. Gao, X. Liu, and S. Chen, First observation of mesospheric and thermospheric winds by a Fabry-Perot interferometer in China, *Chinese Science Bulletin*, *55*(35), doi:10.1007/s11434-010-4192-2, 2010.

Appendix A Wilhelm et al. (2017)

Wilhelm, S., Stober, G., and Chau, J. L.: A comparison of 11-year mesospheric and lower thermospheric winds determined by meteor and MF radar at 69 °N, *Ann. Geophys.*, 35, 893-906, <https://doi.org/10.5194/angeo-35-893-2017>, 2017.



A comparison of 11-year mesospheric and lower thermospheric winds determined by meteor and MF radar at 69° N

Sven Wilhelm, Gunter Stober, and Jorge L. Chau

Leibniz Institute of Atmospheric Physics at the University of Rostock, Kühlungsborn, Germany

Correspondence to: Sven Wilhelm (wilhelm@iap-kborn.de)

Received: 13 February 2017 – Revised: 6 July 2017 – Accepted: 7 July 2017 – Published: 31 July 2017

Abstract. The Andenes Meteor Radar (MR) and the Saura Medium Frequency (MF) Radar are located in northern Norway (69° N, 16° E) and operate continuously to provide wind measurements of the mesosphere and lower thermosphere (MLT) region. We compare the two systems to find potential biases between the radars and combine the data from both systems to enhance altitudinal coverage between 60 and 110 km. The systems have altitudinal overlap between 78 and 100 km at which we compare winds and tides on the basis of hourly winds with 2 km altitude bins. Our results indicate reasonable agreement for the zonal and meridional wind components between 78 and 92 km. An exception to this is the altitude range below 84 km during the summer, at which the correlation decreases. We also compare semidiurnal and diurnal tides according to their amplitudes and phases with good agreement below 90 km for the diurnal and below 96 km for the semidiurnal tides.

Based on these findings we have taken the MR data as a reference. By comparing the MF and MR winds within the overlapping region, we have empirically estimated correction factors to be applied to the MF winds. Existing gaps in that data set will be filled with weighted MF data. This weighting is done due to underestimated wind values of the MF compared to the MR, and the resulting correction factors fit to a polynomial function of second degree within the overlapping area. We are therefore able to construct a consistent and homogenous wind from approximately 60 to 110 km.

Keywords. Radio science (instruments and techniques)

1 Introduction

During the past decades, radars have been used to investigate mesospheric phenomena, e.g., polar mesospheric echoes

(Rapp et al., 2008, Suzuki et al., 2013, Chau et al., 2014) and atmospheric dynamics (e.g. Andrews et al., 1987, Fritts et al., 2012, Imura et al., 2015). Mesospheric radars are distributed over the whole globe and depending on their antenna arrays, frequencies, locations, and transmitting power, they provide valuable information about winds at different vertical and spatial scales. One of the main advantages of radar systems, compared to other remote sensing techniques for the mesosphere and lower thermosphere (MLT), is that they provide continuous measurements independent of weather conditions. A crucial aspect of the measured winds is the reliability of each technique. This requires a proper understanding of the underlying scattering processes and possible instrumental effects, analysis related simplifications, and assumptions that could introduce biases or systematic errors in the derived winds (Reid, 2015).

In this study we analyze data from the Saura Medium Frequency (MF) Radar and the Andenes Meteor Radar (MR), which are both located on the island of Andøya in northern Norway (69° N, 16° E). The comparison is done based on data collected between 2004 and 2014. This study pursues two primary goals. First we want to quantify potential biases between the two techniques, and secondly we intend to merge both wind fields in order to compile a consistent and homogenous wind from approximately 60 to 110 km of altitude. Further we examine whether it is possible to fill gaps in the time series and generate a long continuous time series, ideally throughout the whole comparison period, that is suitable to study atmospheric patterns with periods between months and years. Similar comparisons have already been performed within the past few decades by Valentini et al. (1997), Hocking et al. (2001b), and Hall et al. (2005) with smaller data sets and different locations. Their results showed particularly good agreement between MF and MR for alti-

tudes between 75 and 85 km, but they indicate larger discrepancies at higher altitudes in the obtained winds.

Former studies very often used MF winds obtained by full correlation analysis (FCA). Most MFs employ a wide beam and use only three receiving antennas. However, due to the large observation volume there were issues with the analysis that can mainly be attributed to the underlying assumption that the FCA technique requires homogeneous volume-filled backscattering within the beam volume (Sommer et al., 2016). A technical upgrade in 2003 for the Saura MF radar allows us to operate the MF in a Doppler beam swinging (DBS) mode and to derive winds from multiple oblique beams (Singer et al., 2008). The main difference of Saura, compared to many other MF radars, is its large antenna array (Mills Cross), which permits a rather narrow beam. The benefit of the MF DBS mode is that a wind and tidal comparison with MR can now be done based on the same wind fit routine. We operated the MF in DBS mode for this comparison.

The article is structured as follows. First we describe the radar systems used in this study. We explain the method to determine the wind and tides for both systems in Sect. 3, and in Sect. 4 we compare the winds and tides obtained from both systems. The discussion and conclusions are found in Sects. 5 and 6, respectively.

2 Experimental setup

In this study we present observations from two different radars located at Andenes (69.3° N, 16° E). The systems are the Andenes Meteor Radar, which measures radial velocities from meteor trails, and the Saura MF radar, which obtains measurements from refraction index variations due to dynamic processes (e.g., gravity waves) and D-layer ionization and associated irregularities (Reid, 2015). The technical details for both systems are summarized in Table 1.

In 2001 the Andenes Meteor Radar started its continuous operation up to the present. The radar has been updated several times and the peak transmitting power has increased from 6 to 30 kW. The radar consists of one circular polarized transmitting 3-element Yagi antenna and five circular polarized receiving 2-element Yagi antennas. The receiver antenna array is arranged as five-antenna Jones configuration (Jones et al., 1998). The system operates at 32.5 MHz. Most specular meteors are detected at an approximate altitude of 90 km (Stober and Chau, 2015, Vierinen et al., 2016). At this altitude, the observed measurement volume has a diameter of ~400 km. A detailed description of the so-called All-Sky meteor radar is found in Hocking et al. (2001a).

The Saura HF radar, historically called “MF”, is located 15 km south of the Andenes MR location and operates on a frequency of 3.17 MHz. Although the frequency used is in the HF band, Saura was designed and built as an MF radar (Singer et al., 2003). In 2002 the Saura MF started its observations. The transmitting and receiving antenna is formed

by 29 crossed half-wave dipole antennas in a Mills Cross arrangement. In addition to differential absorption and phase measurements of electron density, the system is able to provide winds (Singer et al., 2003) based on atmospheric irregularities (Briggs, 1984). The altitudinal coverage ranges from 50 to 100 km. Since 2003, the radar has allowed for Doppler beam swinging (DBS) experiments, which were done for this study, and spaced antenna applications. In DBS mode, off-zenith beams towards N, S, E, W and NW, NE, SW, SE at zenith angles between 6.8° and 7.3° were used. More technical information for the Saura MF radar can be found in Singer et al. (2003), Singer et al. (2008).

3 Wind and tidal analysis

We compared wind measurements obtained from the MR and MF instruments using a DBS retrieval technique. In the case of the MR, horizontal winds are preserved using a modified All-Sky-fit Doppler approach (Hocking and Thayaparan, 1997, Hocking et al., 2001a, Stober et al., 2017), for which an ensemble of at least five randomly distributed meteors in a given time and altitude bin are used to estimate the 3-D wind. In the case of the Saura MF, winds are derived by combining the radial velocity measurements from four oblique and one vertical beam. In both cases, the wind vector (u, v, w) is obtained from the following set of equations:

$$v_i(\theta, \phi)_{\text{rad}} = u \cos \phi_i \sin \theta_i + v \sin \phi_i \sin \theta_i + w \cos \theta_i, \quad (1)$$

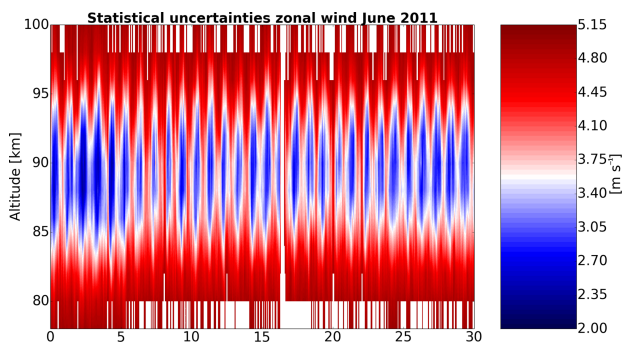
where u, v , and w are the zonal, meridional, and vertical wind components, θ_i and ϕ_i are the zenith and the azimuth angle, respectively, and $v_{\text{rad}i}$ is the radial velocity for each measurement. Hourly winds are obtained by binning the data in height and time. We use a 2 h sliding window centered at the reference time. A similar procedure is used for the altitude bins by applying a 3 km window shifted by 2 km and centered at a reference altitude.

The wind is computed considering the statistical uncertainties in each radial velocity measurement by applying an additional Gaussian weighting depending on its time of occurrence with respect to the reference time and for the altitude coordinate. The Gaussian-shaped window is used to provide an additional weighting of the individual meteors within a time and altitude bin. The regularization already estimates a temporal or vertical shear. This shear is used to penalize the impact of each measured radial velocity depending on its temporal or spatial offset from the reference grid. Further, this shear provides an estimate of the shear error for each time and altitude. This error is added to the statistical uncertainty in the radial velocity measurement. More information about the applied regularization can be found in Stober et al. (2017).

The accuracy of the wind is obtained from the fitting procedure to estimate the wind by taking into account the number of measurements per bin and the statistical uncer-

Table 1. Technical data and main parameters for the radars used in this study.

	Meteor radar	Medium-frequency radar
Location	69.3° N, 16° E	69.3° N, 16° E
Scattering processes	meteor trail	irregularities
Wind analysis height range	75–110 km	50–100 km
Wind analysis vertical resolution	2 km	2 km
Antenna	crossed	crossed
Frequency	32.55 MHz	3.17 MHz
Power	30 kW	116 kW

**Figure 1.** Statistical uncertainties for the hourly zonal wind of the MR for June 2011.

tainties in the measurements in the error covariance matrix. This leads to uncertainties of approximately $2\text{--}6\text{ m s}^{-1}$ for the hourly MR winds with larger errors at the edges of the observation range. This can be seen in Fig. 1, which shows the MR uncertainties based on the hourly zonal wind values for June 2011. The same structure occurs for the meridional wind component (not shown here). A more detailed description of the fitting routine can be found in Stober et al. (2017).

Furthermore, we apply two additional assumptions to simplify the retrieval method. These assumptions are (1) zero acceleration within the altitude and time bin and (2) zero vertical velocity, which leads to a smoother wind field solution. The assumptions are used to constrain our wind retrieval by applying Tikhonov regularization (Aster, 2013; Stober et al., 2017). Considering the rather large observation volume of a meteor radar, which has a diameter of approximately 400 km at 90 km of altitude, it is not advisable to fit for the vertical velocity directly. A wind field spanning such a volume likely also shows patterns of horizontal divergence or convergence. Using a simple gradient expansion of the wind field (Browning and Wexler, 1968 or Waldteufel and Corbin, 1978) shows that the horizontal divergence and the vertical wind are linked. Thus, applying the standard 3-D wind fit as it is typically applied for MST radars (Hooper et al., 2007) is not applicable to MRs.

The Saura MF winds are obtained from the radial velocity measurements. The determination of winds for the

medium-frequency radar is done with the same wind fit routine based on the capability of using our five-beam experiments with one vertical and four oblique. In DBS mode, off-zenith beams towards N, S, E, W and NW, NE, SW, SE at zenith angles between 6.8 and 7.3° were formed for the measurements. The radial velocities of the MF radar are estimated using the momentum method (Strauch et al., 1984), and there is no available information about the statistical uncertainties in the radial velocity measurements (Hooper et al., 2007). Hence, we are not able to conduct a full error propagation to estimate the statistical uncertainties in the observed winds.

Theoretically, it would be possible to compare the radial velocities of meteors, which occur directly in the Saura beam, while Saura is measuring the radial Doppler. This would be more direct than using meteor wind fits. However, the systems are located only 20 km apart, and the Saura beam only points at approximately 6.8° off-zenith, so the number of meteors would not be sufficient to provide statistically significant winds by the meteor radar. Hall et al. (2006) already showed that the number of detected meteors in zenith over and within an MF beam is strikingly marginal. Only by interpolating over a longer time bin would it be possible to provide winds by the meteor system, but these winds are not meaningful for our study.

The tidal components are obtained by estimating the diurnal, semidiurnal, and terdiurnal tidal oscillation components and applying an adaptive spectral filter (Stober et al., 2017). Therefore we decompose the time series as follows:

$$u, v = u_0, v_0 + \sum_{n=1}^3 a_n \sin(2\pi/T_n \cdot t) + b_n \cos(2\pi/T_n \cdot t). \quad (2)$$

Here u_0 and v_0 are the mean zonal and meridional wind. T_n takes values of 24, 12, and 8 for the three tidal components and a_n and b_n are coefficients of the tidal amplitude and the associated phases for each wind component. In this study we focused on the diurnal and semidiurnal tidal amplitudes and phases using a 5-day mean centered at the respective day to suppress smaller-scale variations in the amplitudes. We apply the same procedure to both data sets.

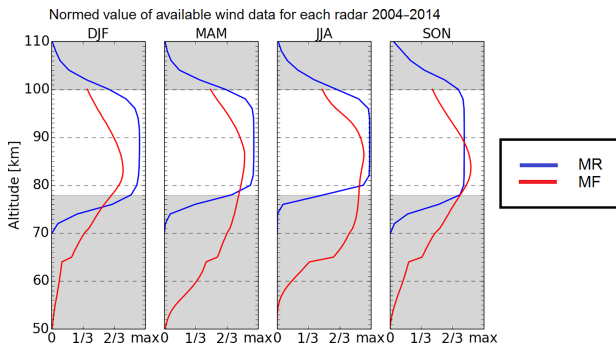


Figure 2. Altitude profile of the available wind data for the MR (blue) and the MF (red) according to season. The gray area shows the wind values for which at least one system is able to provide winds. The white area corresponds to the overlapping data area, which is used for comparison.

4 Results

4.1 Wind comparison between radar systems

In the following section we compare the obtained hourly winds. In Fig. 2 we show altitude profiles of the available wind data for both radars averaged over the seasons December–February (DJF), March–May (MAM), June–August (JJA), and September–November (SON). The white shaded area indicates the overlapping altitude range used for the comparison.

The MR measurements clearly have the best statistics between 80 and 96 km, as there is a clear maximum in the number of detections at these altitudes. In SON the amount of available wind data is reduced compared to the rest of the year due to maintenance in the years 2013 and 2014. Below 78 km and above 104 km, the number of continuous MR wind observations is decreased for all seasons due to the decreased number of meteor detections. These reduced statistics are reflected by the statistical uncertainties, which are increased for these altitudes.

For the MF radar, the number of available wind values varies highly with background ionization, so during the summer the amount of valid wind data is the largest, while during the winter the amount is decreased. The measurements have the best statistics for all seasons between 80 and 88 km, and within the white shaded area the number of valid winds decreases strongly above 92 km to $\sim 50\%$ of the maximum possible number of wind measurements.

In order to assess whether there are systematic seasonal deviations between the two radar systems, we compile a yearly composite by using a 5-day mean centered at the respective day. This composite mainly suppresses the impact of short-term variations, e.g., tides and gravity waves. The composite for both wind components and both radar systems for the years 2004–2014 is shown in Fig. 3. The left two fig-

ures show the typical mesospheric annual wind climatology for the zonal wind component with eastward-directed wind during the winter, a wind reversal during the spring, and a vertical wind shear in summer with eastward winds above ~ 90 km and westward winds below ~ 88 km. This is consistent with the results presented in Hoffmann et al. (2010). The strongest zonal mean winds occur during winter and summer with a mean wind velocity up to ± 40 m s $^{-1}$. Certainly even with smoothing the typical planetary wave activity during the winter season is reflected by both radars. Between March and April the zonal wind component changes from eastward to westward over the whole observed altitude range. However, the gradient during the transition of the wind direction is stronger at all altitudes for the MR than for the MF winds. During the summer, both radars show a strong westward-directed wind with values of about 20 m s $^{-1}$ below 85 km and eastward-directed winds above 90 km. Nevertheless, there is a clear discrepancy in the magnitude above 90 km. The MR measures values around 35 m s $^{-1}$, whereas the MF shows lower values around 10 m s $^{-1}$. The systematic underestimation of the MF winds compared to MR winds was pointed out by other studies; e.g., Valentic et al. (1997), Hocking and Thayaparan (1997), Hall et al. (2005) and Singer et al. (2008).

In addition to the amplitude of the wind, we show in Fig. 4 the comparison of the wind direction between the two radars for winter and summer at the altitudes of 80, 86, and 92 km. These scatter plots are based on hourly zonal and meridional wind data and mainly show good agreement between the radars. With increasing altitudes, the compared azimuth angles of the systems start to diverge from the line of equality.

4.2 Comparison of tidal signatures

Now we proceed to analyze the MF and MR winds with respect to the tides. The tidal signatures should be almost identical considering the global structure and long vertical wavelengths of these waves. The upper part of Fig. 5 shows the 12 and 24 h tidal amplitude for a selected year (2011), and the lower part shows the differences between the MR and the MF tides for the zonal wind. We focus on a comparison of the zonal component because the differences in the winds are more dominant. The stronger tidal component at the MLT is the semidiurnal tide, which reaches mean values of approximately ~ 40 m s $^{-1}$, whereas the diurnal tide reaches values of ~ 25 m s $^{-1}$. This pattern with similar values also occurs in the other years. In the diurnal component a strong enhancement of the amplitude occurs during June and July below 85 km for both data sets. During September and October the systems measure an enhancement of the semidiurnal tide above 85 km in both tidal components with higher values for the MR. The main discrepancies between the two radar systems appear at higher altitudes; the amplitude of the MR increases with height, while the amplitude of the MF

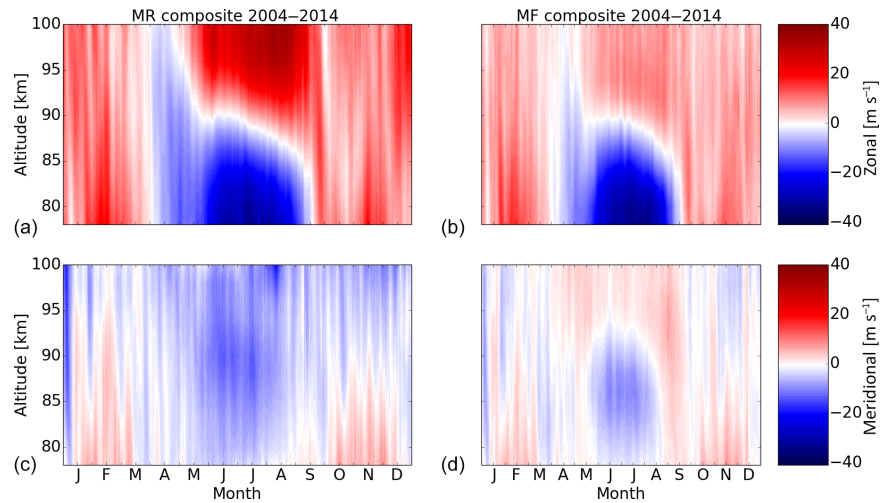


Figure 3. Composite of zonal (a, b) and meridional (c, d) wind component for meteor radar (a, c) and MF radar (b, d) for the years 2004–2014. The data have been smoothed by using a 5-day mean centered at the respective day.

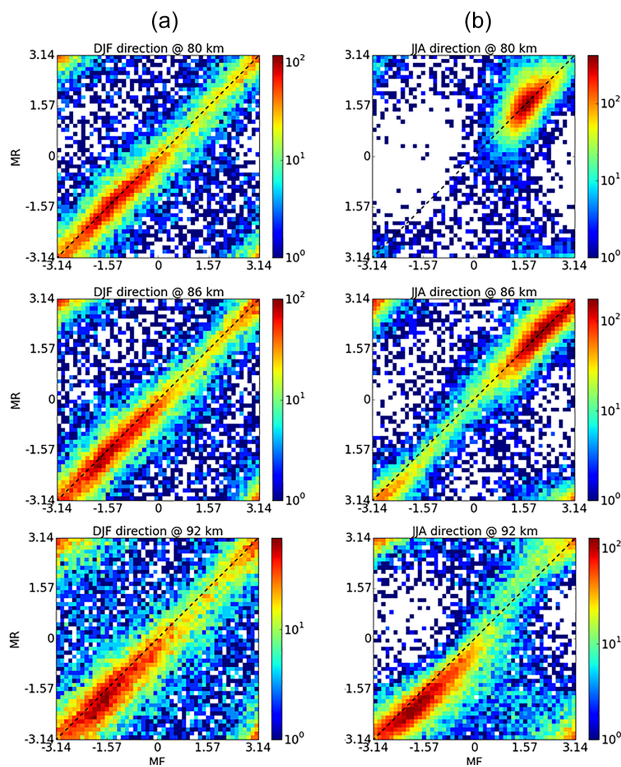


Figure 4. Scatter plots of the wind direction for DJF (a) and JJA (b) for 80, 86, and 92 km. The black dashed line shows the line of equality.

stays nearly constant. Below 90 km the pattern and size of both systems look quite similar.

Within every frame in the lower part of Fig. 5, the differences in each component are shown for different seasons. Figure 5a shows that the semidiurnal tidal amplitudes from the MR are larger than the MF amplitude at nearly every altitude. The differences increase with increasing heights. This behavior is evident for every season of the year. Nevertheless, the differences at every altitude are within the given uncertainties, which reflects the seasonal variability. For the seasonal difference in the diurnal tidal component (right panel), the values of both radars are equal within the given uncertainties. With larger altitudes, the MR radar shows larger mean values than the MF radar. Similar behavior for the amplitude and the differences in each tidal component can be found in the meridional wind (not shown here).

In addition to the amplitudes we compare the phases of the tides (Fig. 6). The phases can reach values between $-\pi$ and π . If the phases for one system show a value of 0 and for the other system the value is π , then the phases of the two systems point in opposite directions, which corresponds, e.g., in the case of the diurnal tide, to a phase offset of 12 h between the two radars. Figure 6 shows the mean seasonal (winter and summer) zonal phase structure based on seasonal means for the winter and summer from 2004 to 2014. Figure 6b shows that the semidiurnal phases of both radars for the winter months are equal between 78 and 94 km and similar up to 98 km within the variance. For the summer in the altitude range between 78 and 96 km, the systems provide the same tidal mean phases within the variance. The given uncertainties show the statistical variability, which increases for both systems with height for the semidiurnal tide. The meridional semidiurnal component (not shown here) provides reasonable agreement between the two radars within the errors for every altitude.

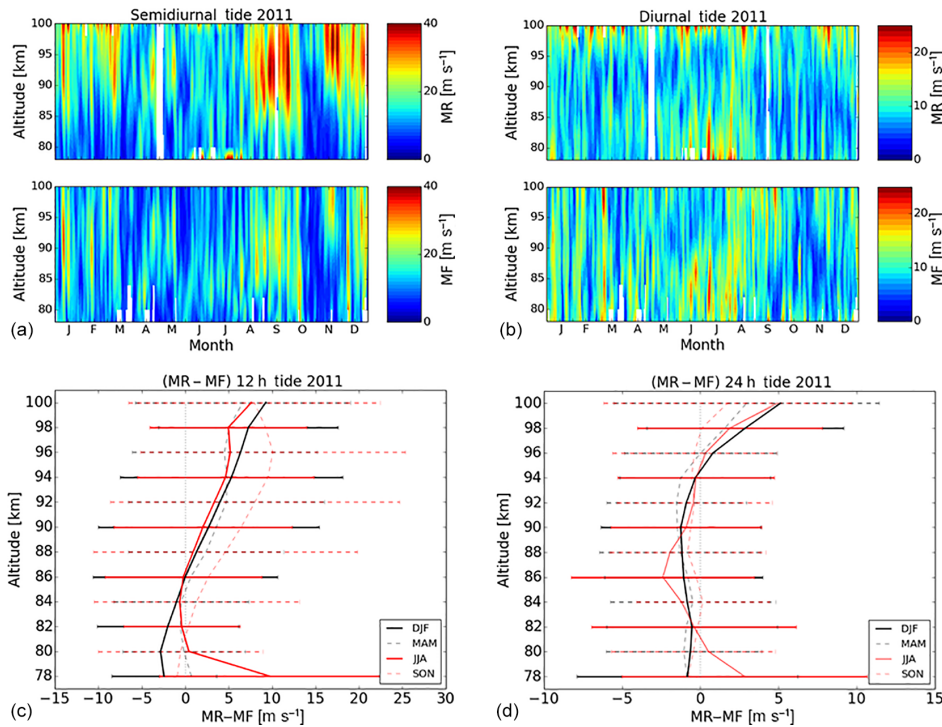


Figure 5. Semidiurnal (a) and diurnal tides (b) in 2011 for both systems. The white areas are missing values based on outliers or due to maintenance. (c, d) Calculated difference for SDT and DT between MR and MF for the seasons DJF (solid black), MAM (dashed black), JJA (solid red), and SON (dashed red) for the year 2011. The error bars correspond to the seasonal variability.

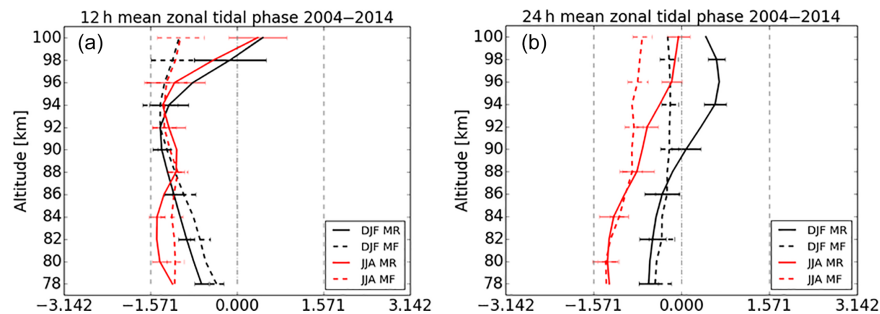


Figure 6. Vertical mean phase structure for the summer and winter seasons between 2004 and 2014. Semidiurnal (a) and diurnal tidal phases (b) of the zonal wind component for winter (DJF; in black) and summer (JJA; in red) for the meteor radar (solid) and the medium-frequency radar (dashed). The error bars show the variability in all seasons compared to the mean.

The comparison of the diurnal tidal phase (Fig. 6a) shows agreement below 90 km for both seasons within the uncertainties. Above 90 km the phase difference increases with increasing altitudes and can be up to ~ 12 h for the summer and ~ 6 h for the winter. The diurnal meridional component shows similar agreement only up to 82 km and above the offset increases and reaches differences of ~ 12 h during summer and winter.

4.3 Correlation

One goal of this study is to combine the two data sets to close gaps in the time series due to maintenance of one of the radars. To achieve that, it is necessary to find whether there is a general offset in the wind between the two systems. In order to generate a homogenous wind time series we intend to remove biases by defining one system as a reference.

Based on the estimated winds for both radars, the correlation coefficient R^2 is determined for different altitudes and times through the year. We apply two different approaches.

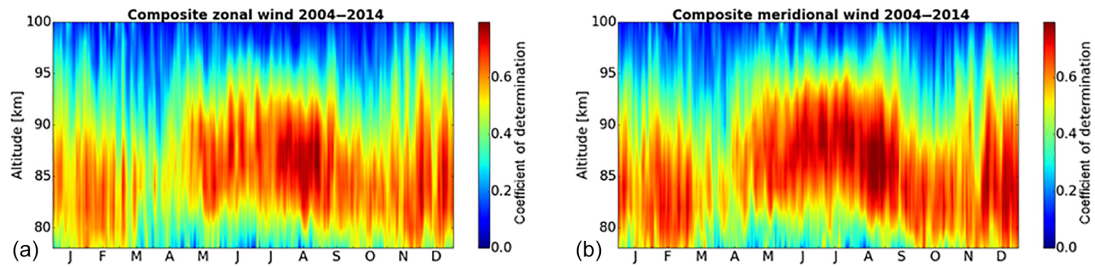


Figure 7. Composite of R^2 for the zonal (a) and meridional (b) component of the overlapped altitude of MF radar and meteor radar for the years 2004–2014. The data have been smoothed by using a 5-day running mean.

The first uses a 5-day running mean centered to the respective day. With this approach we estimate R^2 using hourly wind values over 5 days for each system. Figure 7 shows the resulting annual climatology for the zonal and meridional wind component. For the zonal wind component the highest correlation occurs during the summertime between 84 and 90 km. This is the area in which the wind transition between the eastward and westward wind occurs. During the spring the correlation drops below 0.5, which fits well with the occurrence of the wind transition during that time. Above 92 km the correlation drops below 0.5 and decreases further with increasing altitude. The same pattern is formed for the meridional wind component with decreasing correlation during the spring wind transition and above 94 km.

The second approach aims to remove potential biases between the two data sets shown in Fig. 8. To find a possible linear relationship according to the least square fit method, one radar system needs to be defined as an independent and the other as a dependent variable. According to Hall et al. (2005), based on different measurement volumes, it is not possible to determine, a priori, one of the radar data sets as an independent variable. Several studies have shown good agreement between meteor radar and other instruments and models (e.g., Jacobi et al., 2009, Stober et al., 2012, McCormack et al., 2017). Therefore we use for our study the winds of the MR as a reference. Figure 8 shows a scatter plot for 80, 86, and 92 km for the zonal and meridional wind component of hourly wind values for the complete time period. These show a decreased correlation accompanied by an increased tilt of the scatter for increasing heights. The increased tilt is caused by the stronger winds of the MR, as shown in Fig. 3. The MF winds tend to systematically underestimate the winds compared to the MR at all altitudes. The colors of the scatter represent the counts of the compared hourly wind values of both systems at the same time step.

Table 2 shows R^2 for the hourly wind values for the years 2004–2014 without any smoothing for the following cases: all zonal wind values, all meridional wind values, only February zonal winds, and only June zonal winds. The mean correlation values are slightly higher for the zonal wind component (0.55) than for the meridional wind (0.50). These val-

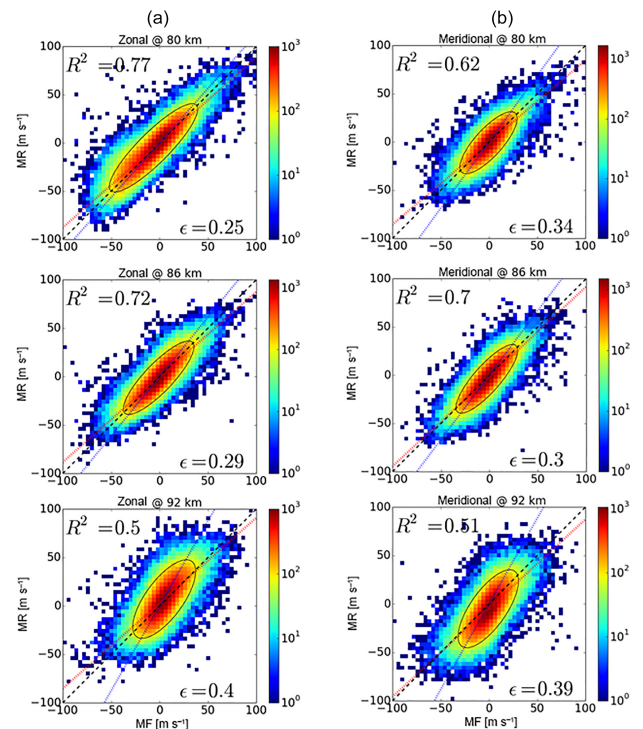


Figure 8. Scatter plots of MR versus MF zonal (a) and meridional (b) wind component for 80, 86, and 92 km. The contour shows the number of wind values for 2004–2014. The black dashed line shows the line of equality. The red dashed line shows the least absolute deviation linear fit with MR as an independent variable, and the blue line is with MF as an independent variable. The ellipse within the contour plot is a criteria for the correlation of the two systems; ϵ is calculated by the width divided by the length of the ellipse.

ues decrease with increasing altitude, from 0.75/0.70 (zonal at 82 and meridional at 84 km) to less than 0.4/0.4 (zonal and meridional > 94 km), which is in agreement with the results in Fig. 7. In addition to the altitudinal differences, we also observe seasonal differences with this approach. We found that for the zonal wind component, R^2 decreases for Febru-

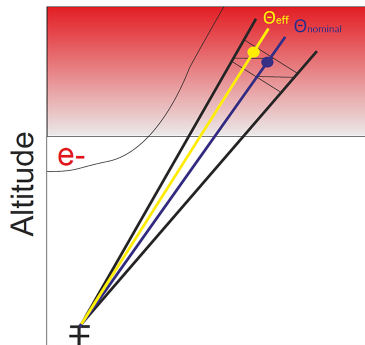


Figure 9. Schematic illustration of a tilted Saura beam (black) in a stratified atmosphere. The reddish area symbolizes an increasing electron density in the stratified medium. The observed tilted beam volume is not equally filled with larger electron density at the nearer-zenith beam edge. This results in a shifted beam pointing angle (yellow) relative to the main beam (blue).

ary from 0.79 to below 0.4 with increasing altitude. In contrast, however, R^2 for June increases between 78 and 88 km and decreases above 88 km. The same pattern occurs for the meridional wind component.

The ellipse within the colored area in Fig. 8 is another measure for determining the correlation between the radars. The thinner the ellipse, the higher the correlation between the two data sets. The ratio (ϵ) between the width and the length of the ellipse indicates the quality of the ellipse. The values can vary between 0 and 1 with 0 as an ideal correlation independent of a possible offset between the data and 1 with no correlation between the two data sets. According to Table 2 the values for the zonal component vary between 0.25 and 0.3 below 86 km and increase with increasing height. The values for the meridional component are on average slightly higher.

5 Discussion

The aim of this study is the comparison of the obtained winds and tides from two different radar systems. On the one side we have the meteor radar and on the other side the medium-frequency radar; the two systems are able to measure wind in an overlapping observation altitude between 78 and 100 km. We compared data gathered between 2004 and 2014. Based on this comparison, we will present in the following section a method to combine both radar winds into a consistent and homogenous data set.

As a first step we analyzed the provided zonal and meridional wind components based on a running mean composite. The zonal wind structure in Fig. 3 exhibits the expected behavior with eastward-directed winds during the winter and a westward-dominated wind during the summer. By visual comparison of the annual climatology, which is computed from a 5-day running mean centered to the respective day,

we obtain good agreement between the two systems below the altitude of 92 km for the zonal wind component, except during the wind transition period in spring. The presence of planetary waves in the wintertime can be seen in both radars. The main difference in the zonal wind component occurs above 92 km during the summer and shows for the meteor radar a strong eastward-directed wind pattern with mean values above 40 m s^{-1} , which do not occur at the same amplitude for the medium-frequency radar with mean values around 10 m s^{-1} .

The meridional wind component shows, as expected, lower amplitudes in both systems. Maximal wind values of $\pm 20 \text{ m s}^{-1}$ can be seen in both systems. Below 92 km the wind pattern of both radars looks similar, according to Fig. 3, expect during the transition time in spring and autumn when the systems sometimes show opposite wind directions.

Moreover, we compare the wind directions based on hourly data. According to Fig. 4, below 92 km the directions are mainly identical and above 92 km discrepancies occur, which is shown in a displacement to the line of equality. This phenomenon occurs for the whole year and increases with increasing altitudes.

Especially for lower wind values, these wind differences can be attributed to the different observation volumes of the two systems with $\sim 400 \text{ km}$ of diameter for the MR compared to $\sim 30 \text{ km}$ of diameter for the MF at 90 km of altitude. In addition to that volume effect, Hall et al. (2005) found a systematic bias (20 %) in the meridional wind component by the MF radar for altitudes below 90 km. They explained that the difference between the two systems occurs because the radars do not measure at the same altitude. The echoes of the MF radar measure in lower altitudes as expected. The reason for this is the group delay due to background ionization. Another reason could be that the signal the MF radar receives is purely due to the neutral wind (Hall et al., 2005). Manson et al. (2004) note that for the zonal wind component the difference is altitude dependent. They show good agreement during summer but with lower MF values (20–50 %) during the winter. Jacobi et al. (2009) further support these results. In agreement with their findings, we discovered an underestimation for the meridional wind below 92 km of approximately 10–60 %, which varies with season and altitude. The zonal component also shows lower wind values for the Saura MF in nearly every season and at every altitude. A reason to use the measured winds with Saura MF carefully above 92 km is due to E-region total reflection and the group retardation near midday (Reid, 2015). A study by McCormack et al. (2017), in which the Andenes MR was compared with the Navy Global Environmental Model (NAVGEM), a global spectral forecast model with a data assimilation algorithm, showed good agreement between their model and the MR measurements for the overlapping altitude range of each mean wind component. Furthermore a comparison between the VHF radar system MAARSY (Middle Atmosphere Alomar Radar System) and the MR at Andenes was done with

Table 2. Coefficient of determination for the altitudes 78 to 100 km for the zonal and meridional wind component based on hourly wind values. February and June R^2 are for the zonal wind component, and ϵ describes the ratio between the length and the thickness of the scatter plot.

Altitude	R^2 zonal	R^2 meridional	R^2 only Feb	R^2 only June	ϵ zonal	ϵ meridional
78	0.75	0.55	0.78	0.27	0.27	0.38
80	0.77	0.62	0.79	0.38	0.25	0.34
82	0.78	0.67	0.77	0.51	0.25	0.31
84	0.77	0.70	0.74	0.61	0.26	0.30
86	0.72	0.70	0.68	0.67	0.29	0.30
88	0.66	0.67	0.61	0.66	0.32	0.31
90	0.58	0.60	0.52	0.62	0.36	0.35
92	0.50	0.51	0.45	0.54	0.40	0.39
94	0.41	0.40	0.36	0.44	0.44	0.44
96	0.30	0.29	0.27	0.30	0.48	0.49
98	0.21	0.20	0.16	0.16	0.52	0.52
100	0.14	0.12	0.12	0.09	0.54	0.53
Mean	0.55	0.50	0.52	0.44	0.36	0.39

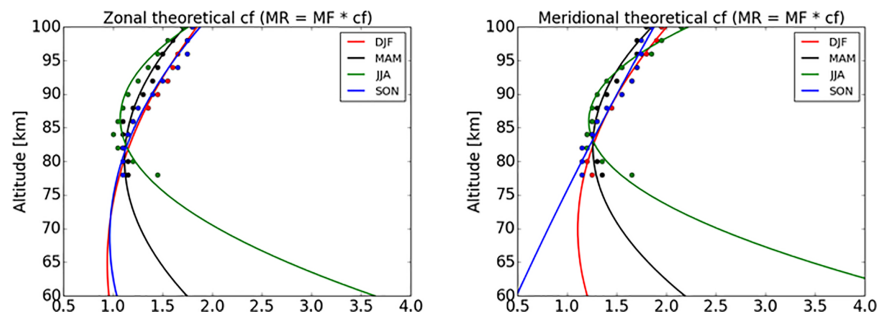


Figure 10. Theoretical seasonal correction factor for the zonal and meridional wind component of the MF radar. The points between 78 and 100 km are based on a comparison between the two radars according to Fig. 11. The fitted curves are polynomial functions of second degree according to Table 3.

correlations for the zonal (0.78) and meridional (0.79) wind components that supports the quality of the MR winds (Stober et al., 2012).

Differences in the wind measurements between the MR and the MF radars occur for two reasons. First, under the assumption of a stratified mesosphere, which means that the mesosphere is homogeneously filled with electron irregularities for every layer, the measured center of scatters in a tilted Saura beam (Fig. 9) is not necessarily in the middle of the beam volume (θ nominal). The measured center of backscatter is weighted by the electron density (θ eff) within the beam. In most cases the scattering center is weighted to lower zenith angles and therefore higher altitudes. This effect also plays an important role during strong electron events in the D and E regions. With higher altitudes this effect will increase due to broadening of the beam and can explain the differences between the MR radar and MF radar below 92 km in the wind amplitude and partially in the wind direction.

A second effect that influences the wind-derived measurements of the Saura radar is the scattering process. According to Singer (2003) and Singer (2007), sometimes there are differences of up to 10 dB between the main lobe of a vertical pointed narrow Doppler beam and the appropriate side lobes. However, the dynamic range of scattering in the D layer is about 35 dB. This side lobe contamination may affect the Doppler measurement itself, as the spectra contain multiple or show smeared and asymmetric peaks, which are difficult to take into account with the momentum method. More information about the momentum method can be found in Strauch et al. (1984). Thus the analysis is not able to derive a reliable radial velocity for these altitudes. Another relevant effect above 90 km is the pointing of the beam itself, the range, and the Doppler measurement. The electron density reaches values of $10^{11} e^{-m^{-3}}$ (Bilitza and Renisch, 2007) that require a more complex analysis, including height retardation, similar to ionosondes. Further, the beam pointing is no longer given by the pointing geometry alone, but becomes more and more affected by wave refraction. Considering electron den-

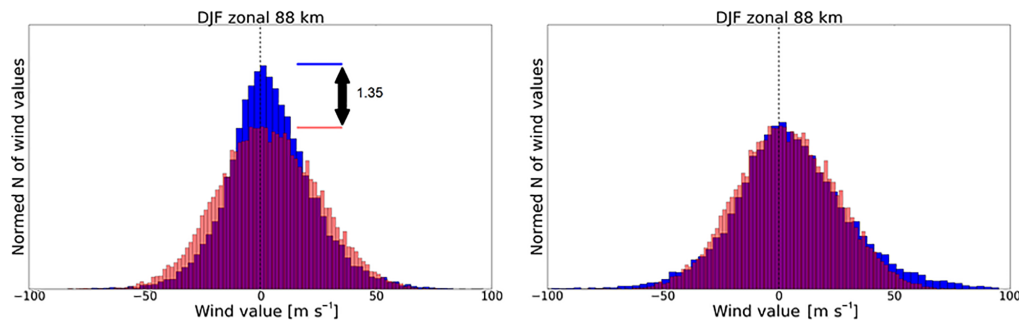


Figure 11. Comparison of sorted hourly wind values according to season, here DJF. MR (red) with values determined by the radar, MF (blue) with original values (left side), and values multiplied (right side) with a proportionate number according to the correction function of Table 3 to receive the same shape as the MR.

Table 3. Seasonal parameters used for a polynomial function to minimize the amplitude difference of the MF radar to the MR.

	a0	a1	a2
Zonal			
DJF	4.03	−0.0952	0.000734
MAM	11.0	−0.248	0.00155
JJA	28.6	−0.637	0.00369
SON	5.38	−0.128	0.000933
Meridional			
DJF	22.21	−0.5078	0.0030875
MAM	31.67	−0.7067	0.0041333
JJA	71.78	−1.615	0.0092282
SON	23.44	−0.5217	0.0030844

sities close to $10^{11} e\text{-m}^{-3}$ shows that the refractive index deviates significantly from $n = 1$ at medium and high frequencies. Assuming a typical electron density profile, the refractive index n is between 0.4 and 0.8 for altitudes above 92 km and the Saura frequency. This implies that the range and the Doppler measurements need to be corrected for the group- and phase-velocity effects.

It would be possible to improve the measurement of Saura by applying interferometry or imaging to account for the angular or range distribution of velocities; imaging Doppler interferometry (IDI; more information can be found in, e.g., Reid, 2015) could be a suitable approach for more reliable radial velocity measurements in the D layer, but in retrospect this adjustment cannot be done for the existing data. However, within this study we compare the winds of the MF and MR to find a statistical correction factor to construct a merged MR–MF time series for the complete available data set of both systems. For altitudes that are likely not affected by wave refraction, a correction factor is used to estimate an average pointing difference from the nominal beam pointing.

Based on the hourly wind values of both systems, we are able to determine a correlation for both wind components for every year by using a running mean boxcar. The shape of the correlation coefficient pattern (Fig. 7) shows the expected reasonable agreement below 92 km nearly for the whole year. The lower altitudes during summer and the wind transition time during spring show decreased correlations. The values of the meridional wind component are, according to these figures, higher than for the zonal component. The reason for the larger meridional values is an artifact due to the running boxcar method. According to Table 2 the values for the meridional wind are lower but the general pattern of the meridional figures is trustworthy. Manson et al. (2004) estimated a correlation (R) between the Erange MR and the Tromsø MF radars at a height of 88 km for winter (zonal) with 0.71, winter (meridional) with 0.75, summer (zonal) with 0.8, and summer (meridional) with 0.83. Our R^2 shows similar values for all cases (Table 2). The difference between Manson et al. (2004) and our findings can be explained by different lengths of the observation time and further by our hourly data compared to get the same shape for the histogram as the 2-hourly mean data of Manson et al. (2004).

The amplitude pattern of the tidal components (Fig. 5) is similar to the wind components with strong differences in the amplitude above 92 km for both components. The tidal amplitude of the MF radar does not grow with higher altitude due to no increasing winds with height. The semidiurnal tide is the main dominant tidal component in both systems, which fits with the results of Hoffmann et al. (2010). Yu et al. (2015) showed, however, increasing tidal amplitudes with increasing heights for several locations. The amplitudes in tidal modes vary with height, season, component, and location. Further studies investigated differences in the tidal components between MF and MR at Tromsø with the result that the surface topography influences the deposition of momentum flux, and therefore a tidal acceleration can be expected to vary with altitude over the observed area and with season (McIntyre, 1989, McLandress, 1998, Hall et al., 2005). In our case the surface topography does not play such an im-

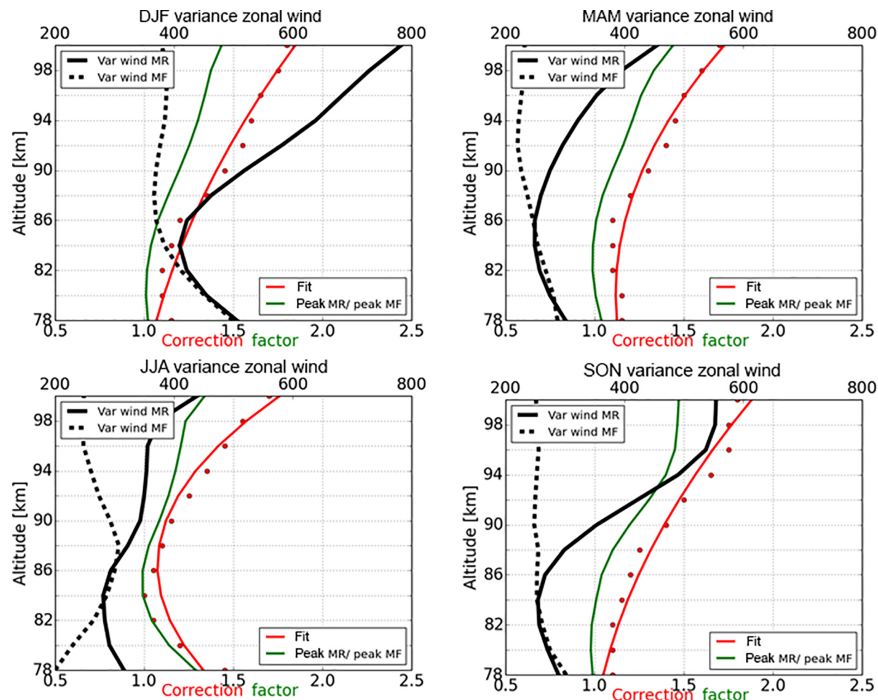


Figure 12. Seasonal plots to adjust the difference in the zonal wind value between the MF and the MR based on two different methods (colored). The correction factor is estimated by sorting the hourly winds according to their values and multiplying the correction factor (CF) on the MF value to get the same shape for the histogram as the MR (see Fig. 11). This is done for every altitude and season manually (red) and by dividing the maximum peak of MR by the maximum peak of MF (green). In black is the variance in the hourly winds for the corresponding season for MF (dashed) and MR (solid) based on hourly wind values over the whole time period for every altitude.

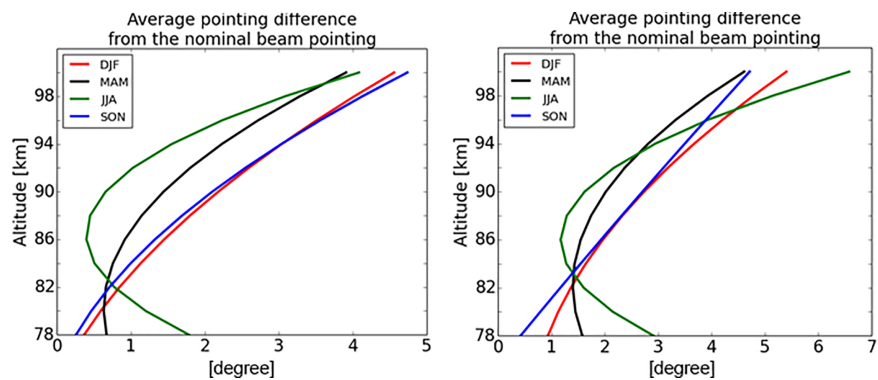


Figure 13. Theoretical average pointing difference from the nominal beam pointing of the Saura radar for DJF (red), MAM (black), JJA (green), and SON (blue) for the years 2004–2014. The left panel shows the zonal wind component, and the right panel shows the meridional wind component.

portant role because the two systems are only 20 km apart. By taking wind values within a 1 h bin, the influence of different measurement volumes of both systems and a strong change in the wind to the previous and next time bin can almost be neglected. Along with the altitudinal differences in the tidal amplitude, a distinct difference also occurs between the semidiurnal and diurnal components; the correla-

tion between the two systems for the 12 h tide is higher than for the 24 h tide with maximal values for the zonal case of ~ 0.6 compared to ~ 0.4 (not shown here). These values decrease with increasing altitudes. In addition to the amplitudes of the tidal components we compared the phases with a similar result. Below 88 km for the diurnal and 94 km for the semidiurnal component, the phases of both systems are in

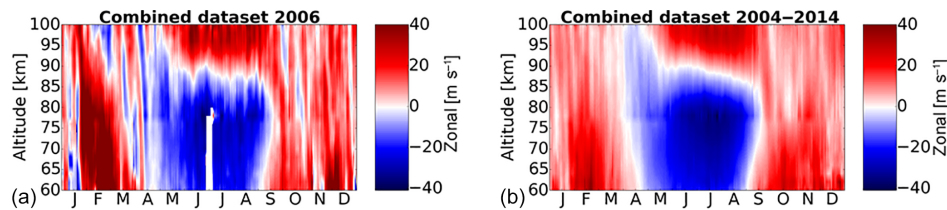


Figure 14. Zonal wind component for the year 2006 (a) and the composite for the years 2004–2014 (b). Below 78 km the data are based on the MF system, and above 92 km they are based on the MR radar. The overlapping area is based on the MR and the gaps within this area are filled with weighted MF radar data according to the correction functions in Table 3. The white areas during June 2006 are missing values.

good agreement within the uncertainties, but the difference increases with increasing heights up to a time delay of 12 h for the diurnal phases.

Due to the mentioned reasons and under the assumption that the derived tidal components of the MR are correct, we recommend that the tidal components based on the MF should not be used for tidal studies above 92 km.

On the basis of these findings we propose MR wind measurements as primary wind for the overlapping coverage and filling existing gaps with weighted MF winds with respect to each wind component, altitude, and seasonal appearance. By comparing the amplitude wind differences between the two systems, we estimated theoretical correction factors (CFs) that fit, in most cases, to a polynomial function of second degree. Table 3 shows the parameters for the polynomials for each season and wind component. By using these parameters we show in Fig. 10 a theoretical profile of the CF down to 60 km for both wind components. The points between 78 and 100 km show estimated CFs based on hourly wind amplitudes without any smoothing but with respect to seasons. The estimation of these CFs is done by comparing these data for every altitude and according to their shape and multiplying the MF radar data with an associated CF (Fig. 11). Figure 10 shows good agreement between the polynomial function and the estimated correction factors for all seasons. The highest theoretical CF below the overlapping area can be found during the summer. It should also be briefly mentioned that below and above the overlapping area these functions need further investigation because polynomials with a higher degree also fit within the overlapping area; beyond the overlapping area, where the CF is extrapolated, strong differences appear.

Figure 12 shows vertical profiles of the observed difference factors and our empirical correction factors. The green line shows the correction factors based on dividing the peak of MR by the peak of MF, and the red line and red dots are CFs and correction functions of Fig. 10. Both curves show a similar pattern. The black curves are the seasonal wind variances for MR (solid) and MF (dashed), which increase in the case of the MR with increasing heights. The variance curve of the MR fits well in shape with the two CF lines. This illustrates that one reason for the shape of the correction function is the growing wind values of the MR compared to the MF.

With the use of CF we show in Fig. 14 two examples for a combined zonal wind data set of both systems with altitude coverage between 60 and 100 km. They are based on a 5-day running mean for the year 2006 (Fig. 14a) and as a composite for the years 2004–2014 (Fig. 14b). Below 78 km the combined data set of the MF system is shown without the correction factor and above 92 km with only the meteor radar data. In the area in between we take mainly the MR data and fill gaps with the Saura radar data winds by applying the correction factors in Table 3. In general this leads to good results for both figures. Only the transition between 78 km and the altitudes below, at which the MF winds without any weighted function are connected, tend to still contain a small offset between the MF and MR winds.

Based on the correction factor we estimate an average pointing difference from the nominal beam pointing of the Saura beam, which can be seen in Fig. 13. Theoretically, by using a modified value of the Saura zenith pointing angle in the analysis, the MF and MR winds would agree better.

6 Conclusions

In this study we have compared the winds of the Saura MF and Andenes MR by applying a DBS wind analysis for both systems. Data from 11 years have been studied with the objective of obtaining a vertical wind profile between approximately 60 and 110 km. To achieve this, biases between the two systems were determined, mainly to remove system-specific differences, such as scattering processes, technical setup, and frequencies. Inside the overlapping altitude in the range from 78 to 100 km, the highest agreement (zonal and meridional $R^2 = 0.78/0.70$) of the two wind components is between 78 and 94 km, except during the transition time (spring) and during the summer below 82 km. Above 92 km the correlation decreases with increasing altitude. It is clear that there is no perfect correlation between the two radars, especially on shorter timescales, which is due to fundamental differences in the systems, e.g., different measurement volume, frequency, and scattering processes. We compared the derived tidal components between the two radars. The amplitudes and the phases of the diurnal and semidiurnal tides from both sets of measurements are in agreement be-

low 90 km. With increasing altitudes above 90 km, the mean semidiurnal phases are in agreement within ± 6 h and the diurnal phases are within ± 12 h. The use of tidal phases at these heights should therefore be taken with caution. The best agreement occurs during the winter period below 90 km for the semidiurnal tide. With increasing altitudes the agreement decreases because the phase and the amplitude of the MF-based tides remain almost constant with increasing altitude. This is not supported by the MR observations, which show a clear phase propagation with altitude and increasing altitudes. Based on our findings we provide a correction function for every season to minimize differences in wind amplitudes between the two systems. These correction functions fit to a polynomial function of second order, but should only be used for the altitudes at which both systems are able to obtain winds. Extrapolating the correction function beyond the overlapping area can cause problems and needs further investigation. By combining the MR and the weighted MF data set, we are able to construct a continuous data set with altitude coverage from 60 to 110 km over 11 years, which can be used for further studies.

Data availability. The radar data are available upon request from Gunter Stober (stober@iap-kborn.de).

Competing interests. The authors declare that they have no conflict of interest.

Acknowledgements. This work was partly supported by the WaTiLa project (SAW-2015-IAP-1 383) and partly by the Deutsche Forschungsgemeinschaft (DFG, German Research Foundation; project no. LU1174, PACOG). We acknowledge the technical support of the IAP technicians and are thankful for the discussions with Peter Hoffmann, Toralf Renkwitz, and Carsten Schult.

The topical editor, Keisuke Hosokawa, thanks Chris Meek and one anonymous referee for help in evaluating this paper.

References

- Andrews, D. G., Holton, J. R., and Leovy, C. B.: Middle atmosphere dynamics, Academic Press, New York, NY, USA, 489 pp., 1987.
- Aster, R. C. and Borchers, B. T. C.: Parameter Estimation and Inverse Problems, Academic Press, Elsevier, 2 Edn., 2013.
- Bilitza, D. and Renisch, B.: International Reference Ionosphere 2007: Improvements and new parameters, *Adv. Space Res.*, 42, 599–609, <https://doi.org/10.1016/j.asr.2007.07.048>, 2007.
- Briggs, B. H.: The analysis of spaced sensor records by correlation techniques, *Handbook for MAP*, 13, 166–186, 1984.
- Browning, K. and Wexler, R.: The determination of kinematic properties of a wind field using doppler radar, *J. Appl. Meteorol.*, 7, 105–113, 1968.
- Chau, J. L., Röttger, J., and Rapp, M.: PMSE strength during enhanced D region electron densities: Faraday rotation and absorption effects at VHF frequencies, *J. Atmos. Sol.-Terr. Phys.*, 118, 113–118, <https://doi.org/10.1016/j.jastp.2013.06.015>, 2014.
- Fritts, D. C., Iimura, H., Lieberman, R., Janches, D., and Singer, W.: A conjugate study of mean winds and planetary waves employing enhanced meteor radars at Rio Grande, Argentina (53.8° S) and Juliusruh, Germany (54.6° N), *J. Geophys. Res.-Atmos.*, 117, D05117, <https://doi.org/10.1029/2011JD016305>, 2012.
- Hall, C., Aso, T., Tsutsumi, M., Nozawa, S., Meek, C., and Manson, A.: Comparison of meteor and medium frequency radar kilometer scale MLT dynamics at 70° N, *J. Atmos. Sol.-Terr. Phys.*, 68, 309–316, <https://doi.org/10.1016/j.jastp.2005.03.025>, 2006.
- Hall, C. M., Aso, T., Tsutsumi, M., Nozawa, S., Manson, A. H., and Meek, C. E.: A comparison of mesosphere and lower thermosphere neutral winds as determined by meteor and medium-frequency radar at 70° N, *Radio Sci.*, 40, RS4001, <https://doi.org/10.1029/2004RS003102>, 2005.
- Hocking, W., Thayaparan, T., and Franke, S.: Method for statistical comparison of geophysical data by multiple instruments which have differing accuracies, *Adv. Space Res.*, 27, 1089–1098, [https://doi.org/10.1016/S0273-1177\(01\)00143-0](https://doi.org/10.1016/S0273-1177(01)00143-0), 2001b.
- Hocking, W. K. and Thayaparan, T.: Simultaneous and collocated observation of winds and tides by MF and meteor radars over London, Canada (43° N, 81° W), during 1994–1996, *Radio Sci.*, 32, 833–865, <https://doi.org/10.1029/96RS03467>, 1997.
- Hocking, W. K., Fuller, B., and Vandeppeer, B.: Realtime determination of meteor-related parameters utilizing modern digital technology, *J. Atmos. Sol.-Terr. Phys.*, 69, 155–169, [https://doi.org/10.1016/S1364-6826\(00\)00138-3](https://doi.org/10.1016/S1364-6826(00)00138-3), 2001a.
- Hoffmann, P., Becker, E., Singer, W., and Placke, M.: Seasonal variation of mesospheric waves at northern middle and high latitudes, *J. Atmos. Sol.-Terr. Phys.*, 72, 1068–1079, <https://doi.org/10.1016/j.jastp.2010.07.002>, 2010.
- Hooper, D. A., Nash, J., Oakley, T., and Turp, M.: Validation of a new signal processing scheme for the MST radar at Aberystwyth, *Ann. Geophys.*, 26, 3253–3268, <https://doi.org/10.5194/angeo-26-3253-2008>, 2007.
- Iimura, H., Fritts, D. C., Janches, D., Singer, W., and Mitchell, N. J.: Interhemispheric structure and variability of the 5-day planetary wave from meteor radar wind measurements, *Ann. Geophys.*, 33, 1349–1359, <https://doi.org/10.5194/angeo-33-1349-2015>, 2015.
- Jacobi, C., Arras, C., Kürschner, D., Singer, W., Hoffmann, P., and Keuer, D.: Comparison of mesopause region meteor radar winds, medium frequency radar winds and low frequency drifts over Germany, *Adv. Space Res.*, 43, 247–252, <https://doi.org/10.1016/j.asr.2008.05.009>, 2009.
- Jones, J., Webster, A. R., and Hocking, W. K.: An improved interferometer design for use with meteor radars, *Radio Sci.*, 33, 55–65, <https://doi.org/10.1029/97RS03050>, 1998.
- Manson, A. H., Meek, C. E., Hall, C. M., Nozawa, S., Mitchell, N. J., Pancheva, D., Singer, W., and Hoffmann, P.: Mesopause dynamics from the scandinavian triangle of radars within the PSMOS-DATAR Project, *Ann. Geophys.*, 22, 367–386, <https://doi.org/10.5194/angeo-22-367-2004>, 2004.
- McCormack, J., Hoppel, K., Kuhl, D., de Wit, R., Stober, G., Espy, P., Baker, N., Brown, P., Fritts, D., Jacobi, C., Janches, D., Mitchell, N., Ruston, B., Swadley, S., Viner, K., Whitcomb, T., and Hibbins, R.: Comparison of mesospheric winds from a high-altitude meteorological analysis system and meteor radar observations during the boreal winters of 2009–

- 2010 and 201–2013, *J. Atmos. Sol.-Terr. Phys.*, 154, 132–166, <https://doi.org/10.1016/j.jastp.2016.12.007>, 2017.
- McIntyre, M. E.: On dynamics and transport near the polar mesopause in summer, *J. Geophysical Res.-Atmos.*, 94, 14617–14628, <https://doi.org/10.1029/JD094iD12p14617>, 1989.
- McLandress, C.: On the importance of gravity waves in the middle atmosphere and their parameterization in general circulation models, *J. Atmos. Sol.-Terr. Phys.*, 60, 1357–1383, [https://doi.org/10.1016/S1364-6826\(98\)00061-3](https://doi.org/10.1016/S1364-6826(98)00061-3), 1998.
- Rapp, M., Strelnikova, I., Latteck, R., Hoffmann, P., Hoppe, U.-P., Haggström, I., and Rietveld, M. T.: Polar mesosphere summer echoes (PMSE) studied at Bragg wavelengths of 2.8 m, 67 cm, and 16 cm, *J. Atmos. Sol.-Terr. Phys.*, 70, 947–961, <https://doi.org/10.1016/j.jastp.2007.11.005>, 2008.
- Reid, I. M.: MF and HF radar techniques for investigating the dynamics and structure of the 50 to 110 km height region: a review, *Prog. Earth Planet. Sci.*, 2, 33 pp., <https://doi.org/10.1186/s40645-015-0060-7>, 2015.
- Singer, W., Latteck, R., Holdsworth, D. A., and Kristiansen, T. (Eds.): A new narrow beam MF Radar at 3 MHz for studies of the high-latitude middle atmosphere: System description and first results, *Proceedings of the 10th international workshop on technical and scientific aspects of MST radar*, 2003.
- Singer, W., Latteck, R., and Holdsworth, D.: A new narrow beam Doppler radar at 3 MHz for studies of the high-latitude middle atmosphere, *Adv. Space Res.*, 41, 1488–1494, 2008.
- Sommer, S., Stober, G., and Chau, J. L.: On the angular dependence and scattering model of polar mesospheric summer echoes at VHF, *J. Geophys. Res.-Atmos.*, 121, 278–288, <https://doi.org/10.1002/2015JD023518>, 2016.
- Stober, G. and Chau, J. L.: A multistatic and multifrequency novel approach for specular meteor radars to improve wind measurements in the MLT region, *Radio Sci.*, 50, 431–442, <https://doi.org/10.1002/2014RS005591>, 2015.
- Stober, G., Latteck, R., Rapp, M., Singer, W., and Zecha, M.: MAARSY – the new MST radar on Andøya: first results of spaced antenna and Doppler measurements of atmospheric winds in the troposphere and mesosphere using a partial array, *Adv. Radio Sci.*, 10, 291–298, <https://doi.org/10.5194/ars-10-291-2012>, 2012.
- Stober, G., Matthias, V., Jacobi, C., Wilhelm, S., Höffner, J., and Chau, J. L.: Exceptionally strong summer-like zonal wind reversal in the upper mesosphere during winter 2015/16, *Ann. Geophys.*, 35, 711–720, <https://doi.org/10.5194/angeo-35-711-2017>, 2017.
- Strauch, R., Merritt, D., Moran, K., Earnshaw, K., and Van De Kamp, D.: The Colorado Wind-Profiling Network, *J. Atmos. Ocean. Technol.*, 1, 37–49, 1984.
- Suzuki, H., Nakamura, T., Ejiri, M. K., Ogawa, T., Tsutsumi, M., Abo, M., Kawahara, T. D., Tomikawa, Y., Yukimatu, A. S., and Sato, N.: Simultaneous PMC and PMSE observations with a ground-based lidar and SuperDARN HF radar at Syowa Station, Antarctica, *Ann. Geophys.*, 31, 1793–1803, <https://doi.org/10.5194/angeo-31-1793-2013>, 2013.
- Valentic, T. A., Avery, J. P., Avery, S. K., and Vincent, R. A.: A comparison of winds measured by meteor radar systems and an MF radar at Buckland Park, *Radio Sci.*, 32, 867–874, <https://doi.org/10.1029/96RS03308>, 1997.
- Vierinen, J., Chau, J. L., Pfeffer, N., Clahsen, M., and Stober, G.: Coded continuous wave meteor radar, *Atmos. Meas. Tech.*, 9, 829–839, <https://doi.org/10.5194/amt-9-829-2016>, 2016.
- Waldteufel, P. and Corbin, H.: On the Analysis of Single-Doppler Radar Data, *J. Appl. Meteorol.*, 18, 532–542, 1978.
- Yu, Y., Wan, W., Ren, Z., Xiong, B., Zhang, Y., Hu, L., Ning, B., and Liu, L.: Seasonal variations of MLT tides revealed by a meteor radar chain based on Hough mode decomposition, *J. Geophys. Res.-Space*, 120, 7030–7048, <https://doi.org/10.1002/2015JA021276>, 2015.

Appendix B Wilhelm et al. (2019a)

S. Wilhelm, G. Stober, and P. Brown, Climatologies and long-term changes of mesospheric wind and wave measurements based on radar observations at high and mid-latitudes, *Ann. Geophys.*, <https://doi.org/10.5194/angeo-2019-51>, under review.



Climatologies and long-term changes in mesospheric wind and wave measurements based on radar observations at high and mid latitudes

Sven Wilhelm¹, Gunter Stober^{1,3,4}, and Peter Brown²

¹Leibniz Institute of Atmospheric Physics at the University of Rostock, Kühlungsborn, Germany

²Department of Physics and Astronomy, Western University, London, Ontario, Canada

³Institute of Applied Physics, University of Bern, Bern, Switzerland

⁴Oeschger Centre for Climate Change Research, University of Bern, Switzerland

Correspondence: Sven Wilhelm (wilhelm@iap-kborn.de)

Received: 28 March 2019 – Discussion started: 12 April 2019

Revised: 16 August 2019 – Accepted: 27 August 2019 – Published: 24 September 2019

Abstract. We report on long-term observations of atmospheric parameters in the mesosphere and lower thermosphere (MLT) made over the last 2 decades. Within this study, we show, based on meteor wind measurement, the long-term variability of winds, tides, and kinetic energy of planetary and gravity waves. These measurements were done between the years 2002 and 2018 for the high-latitude location of Andenes (69.3° N, 16° E) and the mid-latitude locations of Juliusruh (54.6° N, 13.4° E) and Tavistock (43.3° N, 80.8° W). While the climatologies for each location show a similar pattern, the locations differ strongly with respect to the altitude and season of several parameters. Our results show annual wind tendencies for Andenes which are toward the south and to the west, with changes of up to 3 m s^{-1} per decade, while the mid-latitude locations show smaller opposite tendencies to negligible changes. The diurnal tides show nearly no significant long-term changes, while changes for the semidiurnal tides differ regarding altitude. Andenes shows only during winter a tidal weakening above 90 km, while for the Canadian Meteor Orbit Radar (CMOR) an enhancement of the semidiurnal tides during the winter and a weakening during fall occur. Furthermore, the kinetic energy for planetary waves showed strong peak values during winters which also featured the occurrence of sudden stratospheric warming. The influence of the 11-year solar cycle on the winds and tides is presented. The amplitudes of the mean winds exhibit a significant amplitude response for the zonal component below 82 km during summer and from November to December between 84 and 95 km at Andenes and CMOR.

The semidiurnal tides (SDTs) show a clear 11-year response at all locations, from October to November.

1 Introduction

Over the last several decades, studies of wind and wave action in the mesosphere and lower thermosphere (MLT) have focused on coupling processes to layers above and below (e.g., Yiğit et al., 2016), dynamical processes of the wind (e.g., Fritts and Alexander, 2003), the local variability of the measured winds (e.g., Stober et al., 2018), and long-term changes (LTCs) in winds and waves (e.g., Keuer et al., 2007). Wind measurements at these heights rely mainly on remote-sensing techniques, like satellites, lidars, radars, and passive microwave radiometers. Each of these techniques has its own strengths and limitations with regards to the time and altitude resolution or measurement conditions. Meteor radar wind observations of the MLT have a long proven record due to their reliable, long-term measurement capability, independent of weather conditions. These radars detect the ionized plasma trails of meteors left behind after the hypersonic passage of meteoroids in the Earth's atmosphere. The resulting meteor trails drift with the neutral background wind. By measuring the radial velocities and the positions of the trail echoes in the sky, wind velocities of the atmosphere can be determined. The measurements of these local winds and the associated tides are key inputs to validate and up-

date global circulation models. Basically, climatologies of winds and tides in the mesosphere are well represented in global circulation models (GCMs). With the onset of the mesopause, differences occur between models and observations, which are shown in several studies. Yuan et al. (2008a) showed differences between three models and observations, as well as also between the models themselves, by mentioning that the height of the summer mesopause differs. Stronger differences occur during the winter, and opposite prevailing wind directions occur above the mesopause between models and observations (e.g., Pokhotelov et al., 2018). A reason for these differences is probably based on the use of different gravity wave parameterizations.

The general circulation of the MLT is strongly influenced by the transfer and deposition of atmospheric momentum, transported by upward-propagating waves. This momentum perturbs the purely zonal geostrophic flow, which would exist in the absence of any momentum exchange for the case of an atmosphere in radiative equilibrium. In particular, the ageostrophic meridional flow is affected by this momentum exchange, which leads to mesospheric upwelling and downwelling. As a consequence, adiabatic cooling and heating occur, forcing the atmospheric temperature structure away from radiative equilibrium, resulting in a non-radiative equilibrium wind pattern (e.g., Middleton et al., 2001; Becker, 2012). The observed wind, in turn, is a superposition of several atmospheric waves, such as planetary waves (PWs), tidal waves, and gravity waves (GWs), which are categorized according to their spatial extents and periods.

Large-scale PWs are primary formed in the troposphere by topography and diabatic heating. They influence the general circulation by transferring warm air from the tropics to the poles and by returning cold air towards the tropics. Planetary waves with periods of 2, 5, 10, and 16 d and their role in dynamical processes within the MLT and regions above and below have been frequently discussed in the literature (e.g., Iimura et al., 2015; Egito et al., 2016; Matthias and Ern, 2018).

Migrating and non-migrating atmospheric tides in the MLT are crucial for understanding the dynamics in the atmosphere, in particular for vertical coupling processes between several atmospheric layers. They serve as a carrier of momentum, which can be deposited in areas far away from their source region (e.g., Pedatella et al., 2012; Yiğit and Medvedev, 2015). Non-migrating tides are generated by longitudinal differences in radial heating (e.g., Hagan and Forbes, 2002), and while propagating upwards the tidal amplitude grows significantly due to the exponential density decrease. The dissipation of tides contributes to fluctuations in the mean wind flow (e.g., Lieberman and Hays, 1994). For equatorial latitudes, the most dominant tide is the diurnal (24 h), but according to the linear tidal theory (Lindzen and Chapman, 1969), at middle and high latitudes, the diurnal tide does not primarily dominate at the MLT. Therefore, at these latitudes it is the semidiurnal (12 h) tide which is impor-

tant, having the highest amplitudes during the winter months and during the autumn transition (e.g., Hoffmann et al., 2010; Jacobi, 2012; Pokhotelov et al., 2018).

Primary GWs, which are generated in the troposphere, propagate upwards, with the amplitude of the waves increasing exponentially and efficiently transporting momentum and kinetic energy into the middle atmosphere. The main tropospheric source of GWs is the airflow over orographic irregularities, such as mountains, the vertical movements in convection cells, and strong wind shears in combination with jet instabilities. Here, gravity acts as the wave's restoring force against vertical movement. Depending on the propagation direction of the background wind relative to that of the GWs, strong filtering can occur at different heights. For example, during the summer, the mainly eastward-directed GWs are able to reach the mesosphere because most of the westward-propagating waves get filtered by the westward-directed stratospheric background wind. If GWs break at the MLT, they deposit upward transported momentum onto the background wind, which can lead to a wind reversal (e.g., Fritts and Alexander, 2003). The horizontal scale of the associated excitation varies between several tens and several thousand kilometers with associated periods of minutes up to 1 day (Tsuda, 2014).

Examining the observed wind by decomposing it into its distinct spectral components has been performed by several studies in recent years (e.g., Eckermann et al., 2016; Hysell et al., 2017; Shibuya et al., 2017; Baumgarten et al., 2018). For this study, we use the approach of decomposing the wind according to Stober et al. (2017) and Baumgarten and Stober (2019) by applying an adaptive spectral filter technique (ASF). In this technique the decomposition of the observed wind is basically done by adapting the window length for each tidal component and a vertical regularization of the phase slope using the classical harmonic approach:

$$u, v = u_0, v_0 + \sum_{n=1}^3 a_n \sin(2\pi/T_n \cdot t) + b_n \cos(2\pi/T_n \cdot t), \quad (1)$$

where T_n takes the values of 24, 12, and 8 h to determine the diurnal, semidiurnal, and terdiurnal tides for each wind component. a_n and b_n are the coefficients of the appropriate amplitude. The gravity wave activity is the residuum, which includes all fluctuations different than tides and planetary waves.

GW activity is often expressed in terms of spectra as a function of wave frequencies and wave numbers, which is rather challenging considering the observational limitations. Therefore, Fritts and VanZandt (1993) described an energy spectrum for the wind velocity, which is composed of a combination of several GWs. Tsuda et al. (2000) defines the total wave energy as the sum of the potential energy and kinetic energy E_k per unit mass, the latter being given by

$$E_k = \frac{1}{2}(u'^2 + v'^2 + w'^2), \quad (2)$$

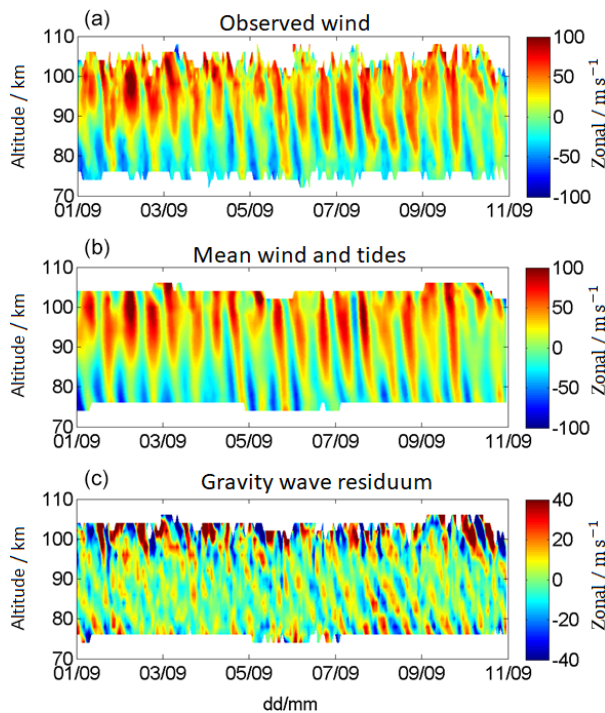


Figure 1. Decomposition of the observed wind (a) into the mean wind and tidal component (b), and the gravity wave residuum (c) for Andenes 1–11 September 2017. Note the different labels of the color bar.

where u' and v' are the perturbation of the horizontal wind velocity and w' is the vertical wind perturbation to the wave propagation direction. Even with very precise measurements w' is much smaller than the horizontal perturbations and therefore can be and is very often neglected.

To illustrate the different components, Fig. 1 shows a decomposition of the observed wind (top) into the mean wind and tidal component (middle) and the GW residual (bottom). The decomposition is shown for the location of Andenes for 10 d. Further information and a more detailed description regarding the algorithm can be found in Sect. 2.

LTCs in the atmosphere are complex. They are influenced by several factors, including fluctuations in solar and geomagnetic activity, which in turn can induce changes in the neutral density together with changes in the zonally directed winds (e.g., Emmert et al., 2008; Stober et al., 2012), or by anthropogenic emissions of greenhouse gases, which affect the troposphere through increased heating and causing cooling in the upper atmosphere (e.g., Beig, 2011; Laštovička et al., 2012). Several studies have investigated LTCs based on radar measurements for the northern high and mid latitudes, e.g., Middleton et al. (2001), Portnyagin et al. (2004), Portnyagin et al. (2006), Keuer et al. (2007), Jacobi et al. (2008), Hoffmann et al. (2011), Imura et al. (2011), and Jacobi et al. (2015). From these studies, meteor radar wind ob-

servations show for the last decade season-dependent results for the mid latitudes, with stronger eastward- and southward-directed tendencies during the autumn and winter and opposite tendencies during the spring (e.g., Jacobi et al., 2015). For high latitudes, the zonal wind shows a time-varying tendency with an overall eastward-directed wind during the winter and also an increase in the semidiurnal tidal amplitude. However, large differences are present among these studies, which are based on different measurement intervals and different latitudes (e.g., Imura et al., 2011).

In this study, we present climatologies and the decadal variability of winds, tides, gravity waves, and planetary waves from the northern high-latitude location of Andenes and the mid-latitude locations of Juliusruh and Tavistock (Canadian Meteor Orbit Radar – CMOR). The data are described in Sect. 2 and the resulting climatologies and decadal climate variabilities for the wind are presented in Sect. 3 and for diurnal and semidiurnal tides, gravity waves, and planetary waves in Sect. 4, respectively. The wind and tidal response on an 11-year oscillation is described in Sect. 5. Section 6 concludes the paper.

2 Data

This study uses observations from three meteor radars (MRs), which are located at the polar latitude station of Andenes (69.3° N, 16.0° E; Norway), the Juliusruh mid-latitude location (54.6° N, 13.4° E; Germany), and the mid-latitude location of Tavistock, the Canadian Meteor Orbit Radar (CMOR, 43.3° N, 80.8° W; Canada).

The Andenes MR was installed in 2002 and was run with a 15 kW transmitter at 32.55 MHz until May 2008. In May 2008 the system was moved to a new location 4 km away from the original site. Later in 2009, the system was further upgraded to 30 kW transmitting power. In 2011 and 2012 the original antennas were updated and replaced. Since 2012 the system has run in a stable hardware configuration. However, the experiment settings also underwent some changes during this interval. From 2002 to 2015 (October) the radar ran an experiment with a pulse repetition frequency of 2096 Hz and a 3.6 km mono pulse using a 2 km range sampling. In October 2015 the experiment was changed and the system is now operated with a pulse repetition frequency of 625 Hz and transmits a 7 bit Barker code with 1.5 km range sampling.

The time series of the Juliusruh MR is a composite of several different radar systems. From 2002 to 2010 the OS-WIN radar was operated in a meteor mode interleaved to its normal MST-radar observations at a transmitting frequency of 53.5 MHz. These measurements were conducted 118 km west of the later Juliusruh MR site. In November 2007 the Juliusruh MR started its operation as a dual-frequency radar at 32.55 and 53.5 MHz. The experiment settings were similar to the ones in Andenes between 2002 and 2015. From 2014 to

2015 the system underwent several modifications. First, the experiment settings were changed to run the 625 Hz pulse repetition frequency and a 7 bit Barker code with 1.5 km range sampling (Stober and Chau, 2015). From January 2014 until autumn 2014 the transmitter of the Juliusruh 32.55 MHz system was not operating and only the 53.5 MHz system was observing. In spring 2015 the Juliusruh 53.5 MHz radar ceased its operation and the Juliusruh 32.55 MHz system remained operational, but with an increased transmitting power of 30 kW. Since this last modification, the system has operated continuously in a stable hardware and experiment configuration.

The CMOR MR provides the longest and most homogeneous MR time series used in this study. The system has run in a more or less unchanged configuration since 2002 as a triple-frequency system (17.45, 29.85, and 38.15 MHz) near Tavistock, Canada. Observations are carried out with a pulse repetition frequency of 532 Hz using a 11 km mono pulse and 3 km range sampling. The 17 and 38 MHz radars each use a 6 kW transmitter; the 29 MHz system was upgraded from 6 to 12 kW in the framework of the CMOR2 upgrade in May 2009. In this study, we compiled one homogeneous wind data set involving all available data of the triple-frequency observations.

In this study, the composites and LTCs are based on data sets for the years 2002–2018 for each location. The winds are obtained by applying a modified version of the all-sky fit (Hocking et al., 2001; Stober et al., 2018), and they have an hourly temporal resolution and partly cover the heights between 70 and 110 km, with a vertical altitude resolution of 2 km. The different atmospheric waves are extracted by an ASF (Stober et al., 2017; Baumgarten et al., 2018). In this study, we focus on observed mean winds, tides, gravity, and planetary waves. The statistical uncertainties are based on the applied fitting procedure by taking into account full error propagation of the radial wind errors as well as the number of meteors per altitude and time bin. The resulting uncertainties of the wind vary in the range of 2–16 m s⁻¹, with larger errors occurring in bins with fewer meteors or at the upper and lower edges of the meteor layer. More information about the experimental setup and the technical specifications for the Andenes and Juliusruh meteor radars, as well as about the wind analysis and the obtained uncertainties for all three radars, can be found in Stober et al. (2017, 2018). More technical information about CMOR and CMOR2 is described in, e.g., Webster et al. (2004), Jones et al. (2005), and Brown et al. (2008).

2.1 Homogenization of time series

The instruments used in this study were operational for almost 2 decades and some meteor radars did undergo substantial maintenance and modifications on the hardware. Most crucial for the wind measurements are the phase calibration and stability, the range sampling, and the Doppler measure-

ment. The Andenes and Juliusruh meteor radars were maintained twice a year, including a test of the phase match of the cables and antennas. Further, the SKiYCORR software runs a phase test and provides a summary file of the impedance for each channel and day indicating potential problems. In addition to the regular maintenance, the CMOR meteor radar interferometry (phases) is cross-validated to optical observations. In particular, meteor showers are monitored with CMOR throughout the year, providing another source of information on the phase stability. The Andenes and Juliusruh meteor radars were also checked and cross-validated using selected meteor showers during the course of the year.

Both European meteor radars were frequently range and power calibrated using a delay line (Latteck et al., 2008; Stober et al., 2010). The CMOR radar is also routinely checked for potential issues in the range sampling by applying various cross-calibrations. All systems used the same software package over the complete time span to derive the Doppler velocities to avoid artefacts due to changes in the parameter estimation (e.g., Doppler velocity or the velocity uncertainty).

Before the multi-frequency data sets for CMOR and Juliusruh are compiled, we analyze the winds for each frequency independently and cross-validate the resultant time series. If one instrument shows systematic issues in the wind time series compared to the other instruments and the climatology, these data are flagged and are no longer considered in the finally compiled and merged wind time series. The Andenes meteor radar data are campaign-wise cross-validated with other meteor radars in Norway.

2.2 Adaptive spectral filtering of time series

The ASF provides a wave decomposition of our original observed time series into a daily mean wind, diurnal and semidiurnal tides, as well as a gravity wave residuum with an hourly resolution. Here, the gravity wave residuum also includes the terdiurnal tidal component. The hourly resolved time series are then averaged to daily means keeping the error information. The ASF is designed to account for the intermittency of waves, in particular, of tides and mean winds for time periods less than a day. Therefore, we adapt the window length of the harmonic tidal fit to the number of wave cycles. In the first step, we fit the daily mean wind with a window length of 24 h plus all tidal components. The next step uses the daily mean wind and the diurnal tidal component as a boundary to extract the information of the semidiurnal tide and so forth. This procedure is applied as a sliding window along the time series and all wave information (amplitude and phase) for all waves is determined for each time step. The technique is least squares based and, hence, robust against unevenly sampled data or data gaps shorter than the length of the window. Another benefit of the least squares implementation is the error propagation to all derived parameters. Further, we implemented a regularization constraint for the

mean winds and diurnal and semidiurnal tides making use of the vertical wavelength information assuming that the mean winds and tidal phase should only show gradual changes within a vertical kernel function of 8 km for the mean winds and 10 km for the tidal phases. The daily mean wind time series (tides and gravity waves removed) are further analyzed to obtain the planetary wave activity. Therefore, we define a seasonal background wind based on the daily mean time series of u_0 and v_0 for the zonal and meridional components, respectively:

$$u_0, v_0 = u_m, v_m + \sum_{i=1}^2 a_n \sin(2\pi/T_n \cdot t) + b_n \cos(2\pi/T_n \cdot t). \quad (3)$$

Here u_m and v_m are an annual mean zonal and meridional wind, and a_n and b_n are coefficients for the seasonal subharmonics with periods $T_n = 365.25/n$ d ($n = 1, 2$). We determine the background wind field for every month at the 15th by fitting the above-described seasonal model to the daily mean wind time series using a 2-year window centered at the respective month and reconstruct the background wind time series for the other days for each month. The planetary wave activity is then given by subtracting the previously obtained daily mean winds and the reconstructed background wind field. The benefit of this approach compared to other techniques, e.g., smoothing the data or running averages, is that it is more robust against larger data gaps of up to months in length. Another benefit is that, due to the long window used for the fitting, seasonal peculiarities, e.g., sudden stratospheric warmings, do not affect the monthly means, but are well captured in the planetary wave activity.

Monthly mean tidal amplitudes and GW and PW activity are derived by computing monthly medians of the available data sets. Thus, the resultant time series contain some data gaps. However, there are still enough data points to estimate a LTC and a potential solar cycle effect for all these waves for each month. The LTC and solar cycle effect are derived by using a linear trend model plus an 11-year oscillation, which is not tied to the F10.7 solar radio flux or the sunspot number. Qian et al. (2019) analyzed WACCM-X and wind observations above Collm (51° N, 13° E) and found that the wind signature is less statistically significant than the temperature response to the solar radio flux. Other studies exploring the stratospheric/tropospheric response to solar forcing indicate a clearer dependence (Salby and Callaghan, 2006; Rind et al., 2008; Lu et al., 2017) on solar activity. At the MLT, the wind seems to be less directly influenced by the F10.7 or sunspot number. Pokhotelov et al. (2018) found almost no correlation between the occurrence of mesospheric echoes at mid latitudes and the solar radio flux (F10.7), but a clear dependence on the occurrence of these echoes due to meridional winds. Further, Stober et al. (2014) investigated the neutral air density response during solar cycle 23 and found a phase delay of almost 1 year between the F10.7 proxy and the neu-

tral air density variation. Considering all the aspects above, we model the resulting mean winds as

$$u_{mm}, v_{mm} = a_{u,v} + m_{u,v} \cdot t + a \cdot \sin(2\pi/11.0 \cdot t) + b \cdot \cos(2\pi/11.0 \cdot t), \quad (4)$$

where u_{mm} and v_{mm} are the monthly mean zonal and meridional components for the mean wind and each wave, $m_{u,v}$ is linear change over the whole period, a and b are the solar cycle components, $a_{u,v}$ is the mean at year 0, and t is the time in years.

3 Climatologies and long-term changes in the mean wind

Analyzing long time series always requires an estimate of the associated confidence values of the measured linear changes or other derived parameters. In this study, we conduct a full error propagation to all parameters using the covariance matrices of the fitted functions. Based on this statistical uncertainty we are able to define the 90 % and 95 % confidence levels given by $x \pm \sigma z$. Here x is a parameter, σ is the statistical uncertainty of x , and z is a factor, which takes values $z = 1.64$ for the 90 % confidence interval and $z = 2$ for the 95 % interval, respectively, assuming a Gaussian error distribution. We label the different confidence intervals by dashed (90 %) and solid (95 %) contours for all derived parameters. We tested our confidence intervals for whether they are significant by introducing two null hypotheses. The long-term linear changes are tested under the assumption that there is no linear change as a null hypothesis, and the solar cycle is tested with the null hypothesis that there is no significant solar cycle. However, it is also important to note that there could be a potential autocorrelation in our time series due to the solar cycle. We estimated all confidence levels under the assumptions that the Gauss–Markov theorem holds and our least square estimators are an unbiased solution, viz. that the fit residuals are uncorrelated.

Mean wind climatologies at the MLT are often shown for a particular location or instrument or as averages over different periods. In this study we present climatologies of mean winds, diurnal and semidiurnal tides, and PW and GW activity covering more than 25° latitude from mid latitudes to polar latitudes. Thus we are providing a profile of the mean wind systems at the MLT over the Northern Hemisphere. Furthermore, the data sets span the same observational periods from 2002 to 2018 and the winds are obtained by the same type of analysis.

The mean wind climatologies are shown in Fig. 2. Every location shows a distinct seasonal pattern, with eastward-directed winds during the winter and a transition/reversal between eastward and westward winds during the summer. Meridional winds are northward-directed during the winter and southward-directed during the summer. The zero line transition is shown as a black contour line. The zonal wind

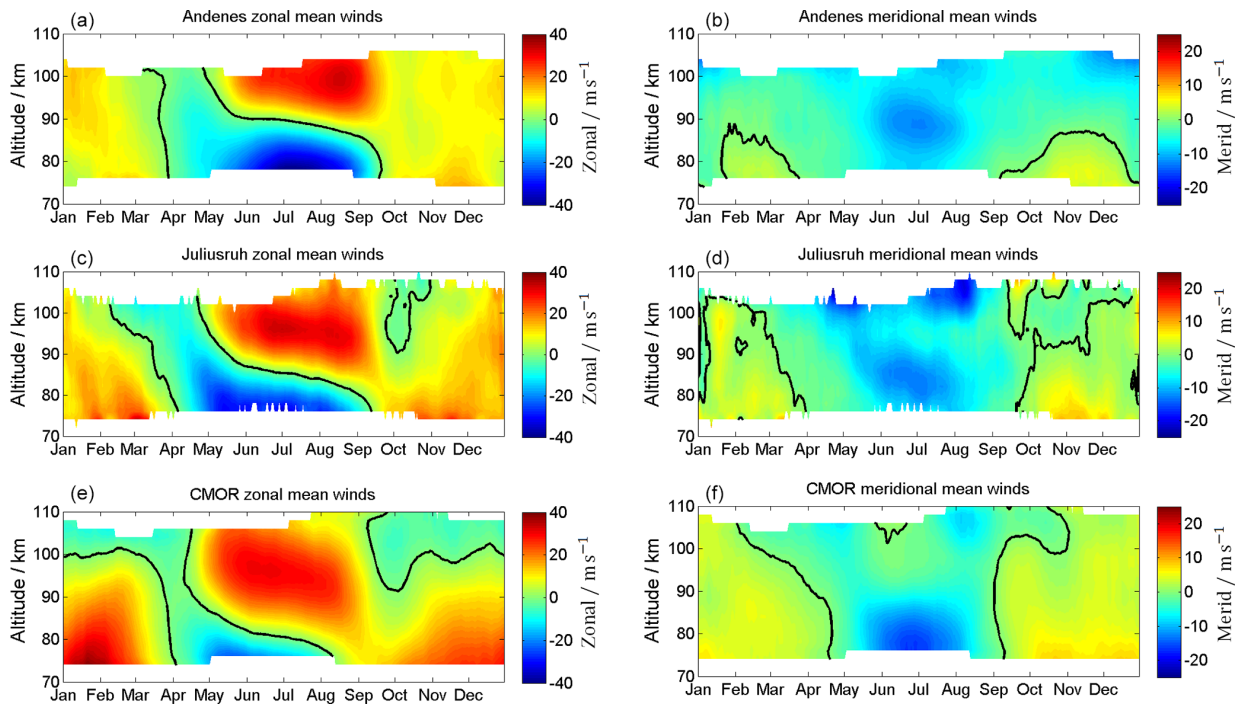


Figure 2. Composite of zonal (a, c, e) and meridional (b, d, f) wind components for Andenes (a, b), Juliusruh (c, d), and CMOR (e, f). The black line corresponds to the wind reversal. Note the different labels of the color bar.

pattern indicates two pronounced features when comparing the different latitudes. In winter, the eastward-directed winds are much stronger at CMOR, with up to 40 m s^{-1} , and decrease towards higher latitudes with $6\text{--}10 \text{ m s}^{-1}$. Further, CMOR shows a zero line crossing in the zonal winds around 100 km altitude, which is not seen at Juliusruh and Andenes. During the fall transition, Juliusruh shows for a month at altitudes above 95 km westward-directed wind. During summer the wind pattern looks rather similar; just the zonal wind reversal altitude increases from the mid latitudes towards the polar latitudes by almost $8\text{--}10 \text{ km}$ (June, July, August).

The meridional wind climatology also shows latitudinal differences. During the winter season, the mid latitudes show northward winds of magnitude 10 m s^{-1} . The summertime is characterized by a southward mesospheric jet of $10\text{--}15 \text{ m s}^{-1}$, which is closely related to the zonal wind reversal. The most prominent features in the meridional winds are the zero line and its altitude variation during the course of the year. At Andenes, northward winds occur only below 90 km altitude and then for only a few months in winter. In contrast, at the mid-latitude stations northward winds are found at all altitudes throughout the winter and southward winds for the summer months. Due to the different lengths of time series compared to other studies, these results are only partly consistent with findings of, e.g., Yuan et al. (2008b), Kishore Kumar and Hocking (2010), Hoffmann et al. (2011), Jacobi (2012), Conte et al. (2018), and Lukianova et al. (2018).

Although the climatologies are statistically robust regarding the mean patterns in both wind components, there is a year-to-year variability and also changes over much longer timescales. Figure 3 shows the time series of the zonal (left) and meridional (right) winds for the Andenes high-latitude location (top) and the Juliusruh (middle) and CMOR (bottom) mid-latitude locations. As described in Sect. 2, especially for Juliusruh, the system modifications resulted in an increase in the altitude coverage due to software and hardware improvements over several years. The seasonal pattern, shown in the climatologies (Fig. 2), is even more clearly visible in Fig. 4, where the year-to-year variability is more pronounced, by using the seasonal fit removing the PW activity from the time series.

Just by visual inspection of Fig. 4, some of the year-to-year variability or LTC becomes visible; e.g., for the years 2003–2007 CMOR shows a westward-directed wind regime above 100 km during summer, which disappears in more recent years. Furthermore, there is an enhancement of the southward-directed winds in Andenes after the year 2015 at altitudes above 95 km.

Monthly changes are estimated using Eq. (4) and are shown in Fig. 5 for both wind components. The dashed black lines represent the 90 % confidence level and the solid black lines the 95 % confidence level. It is rather obvious from Fig. 5 that there is no common linear change at all three latitudes, and thus we discuss each site separately. At An-

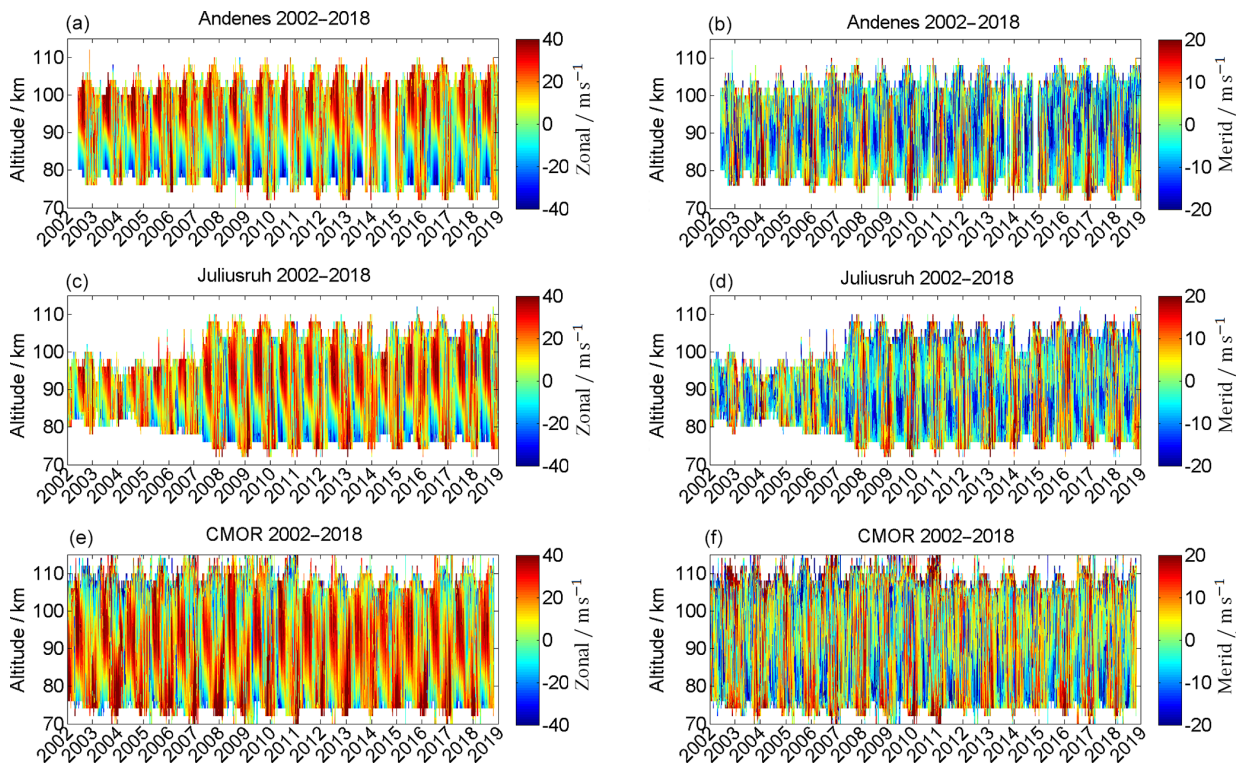


Figure 3. Observed zonal (a, c, e) and meridional (b, d, f) wind components for Andenes (a, b), Juliusruh (c, d), and CMOR (e, f) for the locations according to available data series. Note the different labels of the color bar.

denes, an enhancement of the westward-directed wind occurs during the beginning of the year with values of up to $0.3 \text{ m s}^{-1} \text{ year}^{-1}$, as well as for the summer in the area above the transition height. After the fall transition, a small enhancement of eastward winds is found, with values of up to $0.3 \text{ m s}^{-1} \text{ year}^{-1}$ below 100 km. The meridional wind for Andenes shows a pronounced southward-directed wind long-term variability, with values of up to $0.5 \text{ m s}^{-1} \text{ year}^{-1}$ above $\sim 96 \text{ km}$ for the winter and above $\sim 90 \text{ km}$ for the summer. The LTC for Juliusruh is less significant, with changes which correspond to an eastward-directed tendency during the beginning of April and May and westward-directed below 90 km at June/July. Furthermore, eastward enhancements below 90 km between September and November and at the beginning of the year above 90 km, with values of up to 0.5 m s^{-1} , are found. The meridional component of Juliusruh shows tendencies towards south between January and April and an opposite tendency between May and November. At the location of CMOR, the strongest significant LTC occurs between April and August with an eastward acceleration of the zonal wind, enhancing the zonal jet above 90 km and weakening the westward jet below with values of up to $0.5 \text{ m s}^{-1} \text{ year}^{-1}$. Meridional winds at CMOR show a southward long-term variability between 90 and 100 km at the

beginning of the year and some northward accelerations in summer.

The seasonal analysis provides information about the mean zonal and meridional wind for each year and altitude. Figure 6 shows the vertical LTC based on annual mean values. The vertical profiles indicate the linear change per decade of the zonal (red) and meridional (blue) wind. The most significant changes occur at Andenes in both wind components. The mean zonal wind speed is decreasing between 85 and 100 km by up to $3 \text{ m s}^{-1} \text{ decade}^{-1}$. The LTC of the meridional wind reaches values up to $2 \text{ m s}^{-1} \text{ decade}^{-1}$. At mid latitudes (Juliusruh) the zonal wind shows only a weak change per decade and an eastward acceleration with $0\text{--}0.5 \text{ m s}^{-1} \text{ decade}^{-1}$. The meridional winds indicate a more pronounced linear tendency. Below 85 km the meridional jet seems to be further westward accelerated, whereas at higher altitudes an eastward acceleration is found. At CMOR the zonal wind shows almost no long-term variability at all altitudes between 75 and 110 km. The meridional wind indicates a LTC above 90 km altitude corresponding to a northward acceleration of the mean circulation.

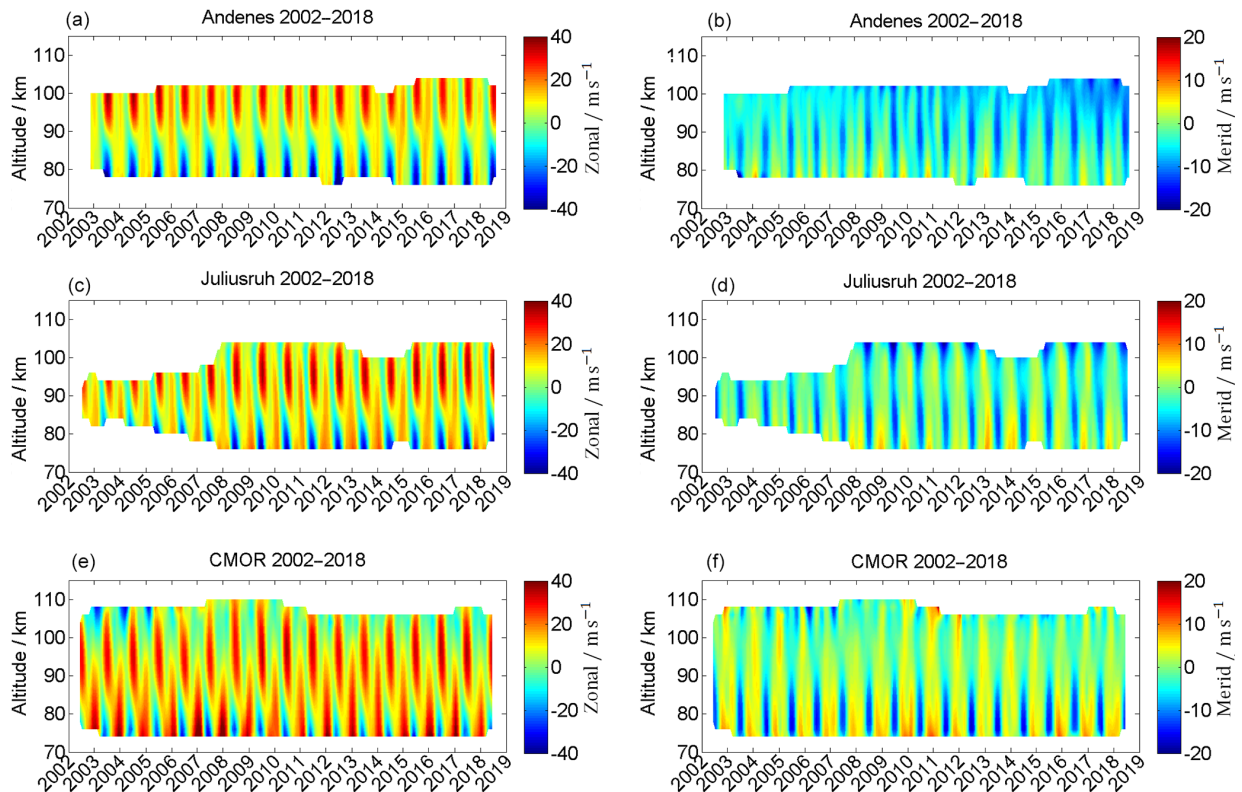


Figure 4. Seasonal mean zonal (a, c, e) and meridional (b, d, f) wind components for Andenes (a, b), Juliusruh (c, d), and CMOR (e, f) for the locations according to available data series. Note the different labels of the color bar.

4 Climatologies and long-term changes in waves

4.1 Diurnal tides

The monthly median amplitudes and the associated composites for the tidal 24 h diurnal components are shown in Figs. 7 and 8. The seasonal pattern of the diurnal tidal (DT) amplitude shows a rather rapid increase around 100 km altitude and at least during the summer a secondary enhancement around 80 km altitude with values of $\sim 15 \text{ m s}^{-1}$. Comparing all three locations, CMOR shows the strongest maximum and strongest mean amplitudes for the zonal diurnal tides, with mean values larger than 25 m s^{-1} . This occurs at heights above 90 km and especially between January and April shows a general enhancement of the zonal diurnal tidal amplitude. Juliusruh reaches maximum mean values of $\sim 25 \text{ m s}^{-1}$ only between the late summer and autumn above 100 km. During this time, Andenes also shows the strongest diurnal tidal amplitudes in the zonal direction, but with weaker maximal mean values of up to 20 m s^{-1} . The meridional diurnal tidal component at all three locations shows a similar pattern, with enhancements of the amplitudes between summer and winter, for heights above 94 km, where it reaches maximum mean values of over 30 m s^{-1} . All lo-

cations show a second increase during the summer around 82 km, and even higher up for CMOR, with mean values of $15\text{--}20 \text{ m s}^{-1}$. Another very prominent feature of the diurnal tidal amplitudes is related to its polarization relation. At Andenes and Juliusruh the meridional component is significantly enhanced compared to the zonal diurnal tidal amplitude. At CMOR this effect is less pronounced during June–December and reverses in spring, where the zonal diurnal tidal amplitude is much larger compared to the meridional component.

Comparing our climatologies to previous studies reveals some interesting differences. Portnyagin et al. (2004) and Jacobi (2012) found a distinct maximum during the summer months and almost no tidal signature in winter at altitudes from 92 to 98 km. Both studies also did not show the diurnal summer maximum below 82 km. These differences are partly explainable by the different length of the analyzed time series. Portnyagin et al. (2004) could only use a bit more than 1 year of data for the Scandinavian climatology. Jacobi (2012) compiled a climatology from 6 years during solar minimum conditions. However, the ASF decomposition of tides and mean winds considering the intermittent behavior of the diurnal amplitude and phase may also play a role.

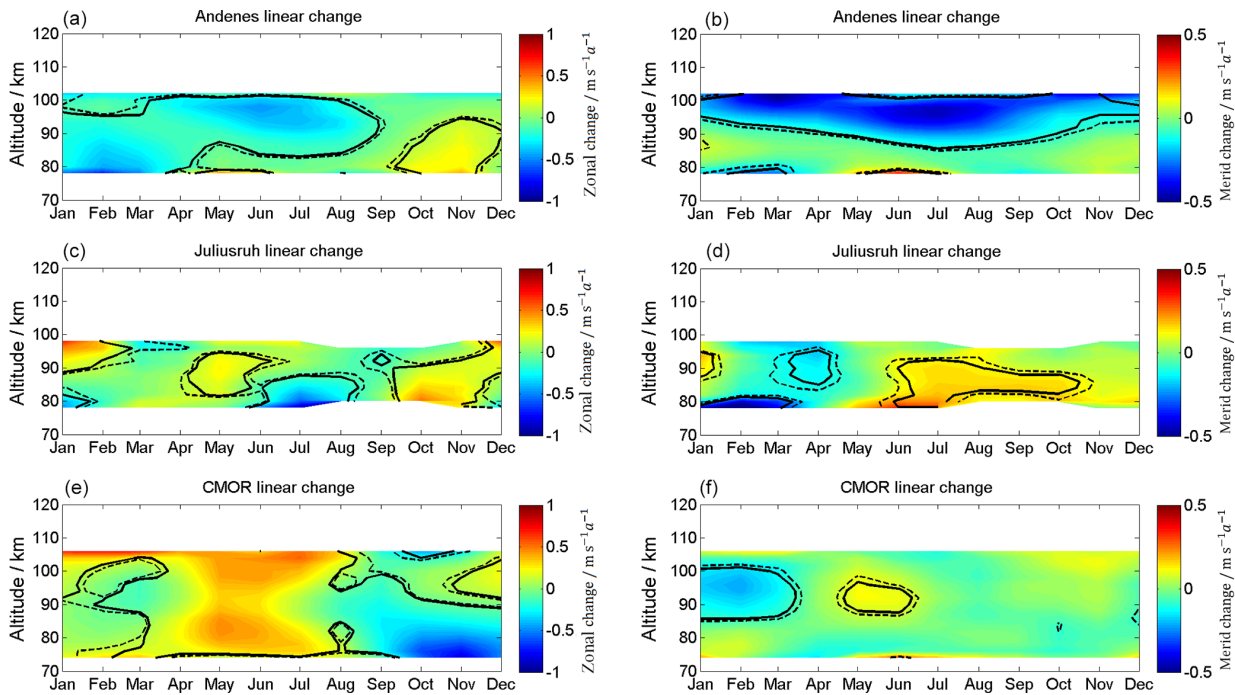


Figure 5. Linear long-term changes in zonal (a, c, e) and meridional (b, d, f) wind for Andenes (a, b), Juliusruh (c, d), and CMOR (e, f). Note the different labels of the color bar. The solid black lines correspond to the 95 % significance, the dashed black lines to the 90 % significance.

The diurnal tidal phases are shown in Fig. 9. The phases are referenced to a longitude of 13° east. The white contour line labels phase jumps and zero phases. The CMOR phases are shifted as if they would have been observed at the CMOR latitude but at the above-mentioned longitude in the European sector. The diurnal tidal phases show a distinct seasonal pattern and latitudinal differences. Throughout the year there are substantial changes in the phases at a given altitude; in particular, at the polar latitudes during the winter months, the phases undergo phase drifts of several hours within a month.

Based on the long-term series, Fig. 10 indicates the interannual LTC for the diurnal components. For the locations of Andenes and Juliusruh, the diurnal component shows small but significant tendencies. During the summer at Andenes, a westward-directed amplitude gradient is present in the westward wind regime below 85 km, with values of up to $0.3 \text{ ms}^{-1} \text{ year}^{-1}$. Furthermore, there is a northward-directed wind amplitude change during the fall at around 100 km. At the location of Juliusruh, changes take place in the zonal component during the winter, with a tendency towards a decreasing diurnal tidal activity above 90 km. However, at Andenes and Juliusruh the zonal and meridional diurnal tidal amplitudes show only rather small changes from 2002 to 2018. At CMOR changes emerge between 82 and 100 km in January. During the early winter, the LTC shows an increasing diurnal tidal amplitude activity, with values up to $0.4 \text{ ms}^{-1} \text{ year}^{-1}$ for the zonal component and almost no

change for the meridional component. During the summer months, the LTC points towards a decreasing tidal amplitude, with up to $1 \text{ ms}^{-1} \text{ year}^{-1}$ for heights above 100 km. Meridional tidal diurnal amplitudes at CMOR exhibit only small changes.

4.2 Semidiurnal tides

The 12 h semidiurnal tide is the most dominant wave in the MLT throughout the year at mid and high latitudes. The time series of semidiurnal tidal (SDT) amplitudes is presented in Fig. 11 and the SDT climatology is given in Fig. 12. SDT amplitudes are usually larger compared to DT amplitudes and reach at the mid latitudes for the zonal wind component maximum mean values of $\sim 30\text{--}40 \text{ ms}^{-1}$ and for the meridional component maximum mean values of $20\text{--}40 \text{ ms}^{-1}$. In general, the semidiurnal tidal components at all locations show similar seasonal patterns. SDT amplitudes increase with increasing heights and reach maximum values around 100 km altitude. The seasonal pattern of the SDT shows a very similar morphology throughout the year at all three MR sites. There is a winter maximum, a spring minimum, and a second amplification during September–October and a second minimum in November. At Andenes the SDT amplitude reaches mean values for both components of up to 30 ms^{-1} . The highest SDT amplitudes are seen at mid-latitude station Juliusruh during the winter months, with values of up

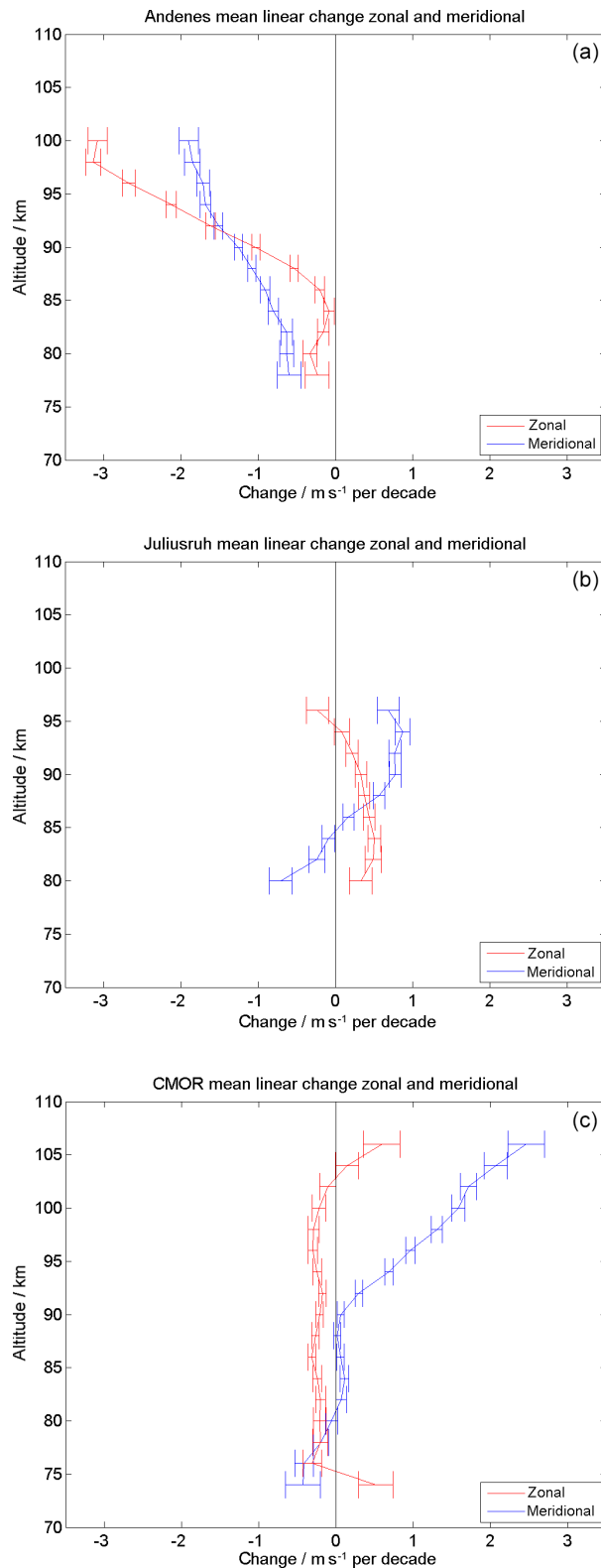


Figure 6. Linear long-term changes in zonal (red) and meridional (blue) wind, based on annual values for Andenes (a), Juliusruh (b), and CMOR (c). The error bars correspond to the statistical variance.

to 40 m s^{-1} . In contrast, the fall transition reaches its highest SDT amplitudes of $\sim 40 \text{ m s}^{-1}$ (zonal component) at CMOR.

At Andenes and Juliusruh the zonal and meridional wind components indicate similar values for amplitudes and occurrence of the SDT. Comparable amplitudes are present during the winter months at CMOR. However, the fall transition above looks slightly different for the CMOR MR. The zonal SDT amplitude appears to be larger than the meridional component.

Figure 13 shows the phase behavior for the SDT. The seasonal pattern indicates an asymmetry and rapid phase change during the fall transition and the winter months. During the spring transition the phases also are altered, but are less prominent compared to the fall and winter time. The phases also reflect the seasonal asymmetry similar to the amplitudes of the SDT. Further, it appears that latitudinal differences between Andenes and Juliusruh are small, whereas the phase differences to the CMOR latitude are much more significant. SDT phases also show continuous phase changes throughout the year. During the fall transition the phase changes within a month by more than 6 h at all three latitudes. However, the winter time is also characterized by drifting SDT phases within a month.

The LTC for the semidiurnal tides is shown in Fig. 14. At Andenes a significant change emerges above 90 km during the winter (November, December), showing a rather strong decrease in the SDT with amplitudes of $1 \text{ m s}^{-1} \text{ year}^{-1}$. Additionally, a significant enhancement of the SDT occurs during the autumn transition, showing an increase of up to $1 \text{ m s}^{-1} \text{ year}^{-1}$. Similar patterns for the summer also occur for Juliusruh. This behavior is not reflected at CMOR. There, it appears that the SDT amplitudes in November are further increasing in the zonal and meridional components. CMOR also exhibits a significant increase in the wintertime (December–February) of SDT amplitudes above 90 km.

4.3 Planetary and gravity waves

The planetary wave activity is estimated as residual between the daily mean winds, as obtained from the adaptive spectral filtering and the seasonal fit shown in Eq. (3). The seasonal fit provides a robust estimate of a background wind field for every day of the year and each wind component. The zonal and meridional wind residuals can be written as u' and v' and are considered a good proxy of a planetary wave amplitude. However, this method does not allow us to distinguish between a planetary-wave-like oscillation and a SSW event, which typically lasts 3–5 d at the MLT. However, Matsuno (1971) already pointed out that PWs play a major role in the evolution of SSWs. Figure 15 shows the PW energy. All three locations show striking enhancements during the winter, especially during years when a major sudden stratospheric warming (red arrow) takes place. During the years with a major sudden stratospheric warming event, the PW energy appears to be increased and takes values of

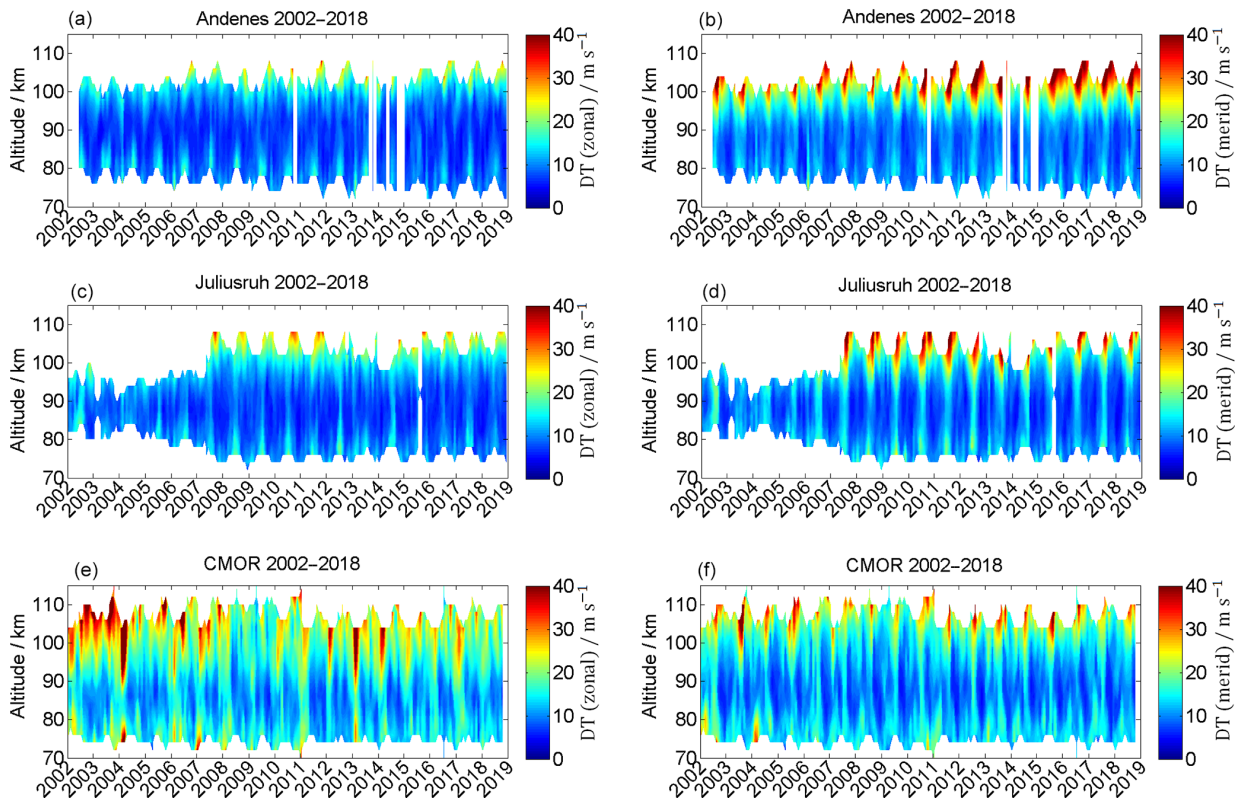


Figure 7. Time series of the zonal (a, c, e) and meridional (b, d, f) diurnal tidal components for Andenes (a, b), Juliusruh (c, d), and CMOR (e, f).

up to $300 \text{ m}^2 \text{ s}^{-2}$ in the winter months. Minor sudden stratospheric warmings (green arrow) show also an increase in the PW energy, but are usually weaker than during years with a major sudden stratospheric warming. Even for the year 2016, where we found an exceptional circulation pattern at the MLT, an enhancement of the PW energy is present Stober et al. (2017), although this year did not show the evolution of a typical SSW (Matthias and Ern, 2018). For the rest of the year, the PW activity is comparatively low, with sparse enhancements observed at CMOR.

In Figs. 16 and 17 the long-term observations of kinetic gravity wave energy (GW) and the corresponding GW energy climatology are presented. The general seasonal pattern for all three locations appears to be quite similar. An enhancement of the kinetic GW energy with increasing heights is noticeable, as well as a seasonal pattern with increased GW energies between the autumn transition and the end of the winter, with values of up to $400 \text{ m}^2 \text{ s}^{-2}$. Below a height of $\sim 82 \text{ km}$ during the summer there is a secondary enhancement, which is especially noticeable at Andenes and Juliusruh. At that time, values of up to $\sim 150 \text{ m}^2 \text{ s}^{-2}$ are recorded for Andenes, and up to $\sim 250 \text{ m}^2 \text{ s}^{-2}$ for Juliusruh.

5 Wind dependencies on an 11-year oscillation

For long-term wind data which exceed the period of a solar cycle it is advantageous to consider the influence of an 11-year oscillation on the wind. Figure 18 visualizes the impact of an 11-year oscillation on a seasonal basis. All three stations show nearly no changes in the meridional component, while the zonal winds appear to be highly responsive to the solar activity during the summer around 80 km and during the winter. At the equinoxes, the zonal wind component is unaffected by the 11-year modulation. During the summer, all three locations show an 11-year oscillation with an amplitude response between 3 and 5 m s^{-1} below 82 km .

In addition to the annual profile, Figs. 19 and 20 show seasonal linear influences of solar radiation on the tidal components. The influence of the 11-year oscillation on the diurnal tides is shown in Fig. 19. Andenes and Juliusruh show no changes in the zonal component, while the 11-year oscillation in CMOR becomes prominent above 90 km . For the meridional component, only Andenes and CMOR are affected above 94 km during the summer months, by values of up to 4 m s^{-1} . For the semidiurnal tides (Fig. 20) all locations show for both components enhancements during and after the autumn transition above $\sim 90 \text{ km}$, which last at CMOR

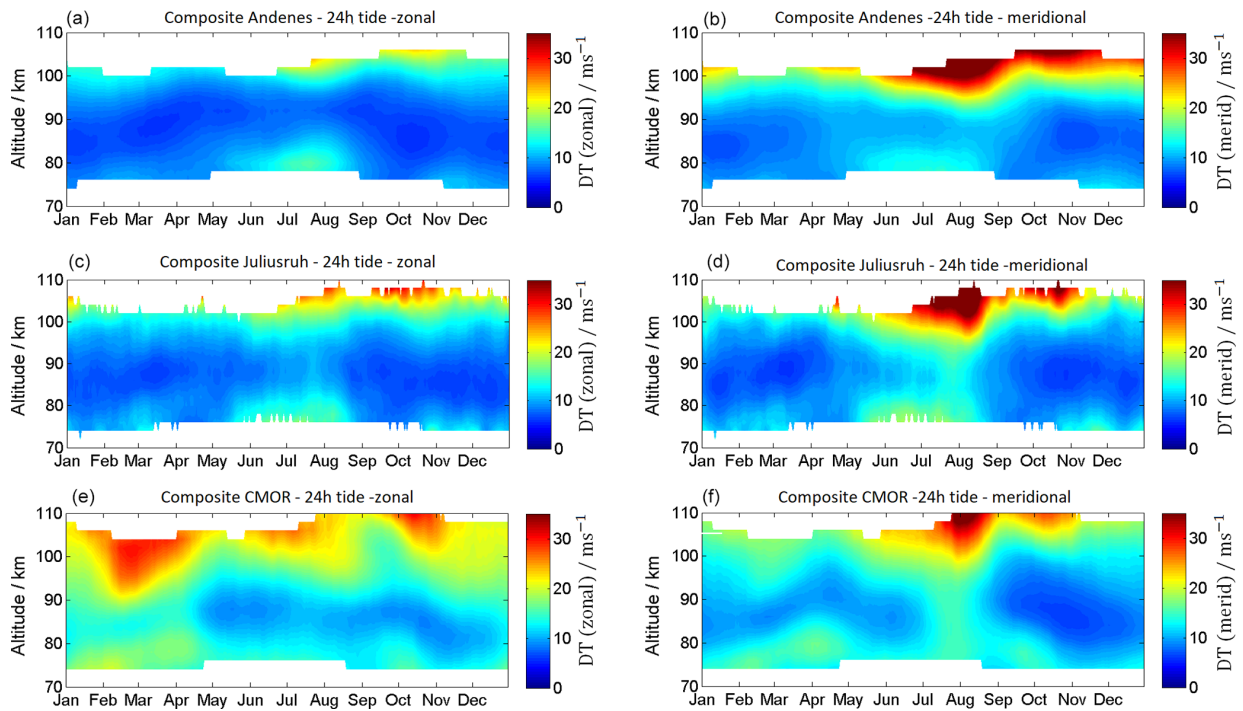


Figure 8. Composites of the zonal (a, c, e) and meridional (b, d, f) diurnal tidal components for Andenes (a, b), Juliusruh (c, d), and CMOR (e, f).

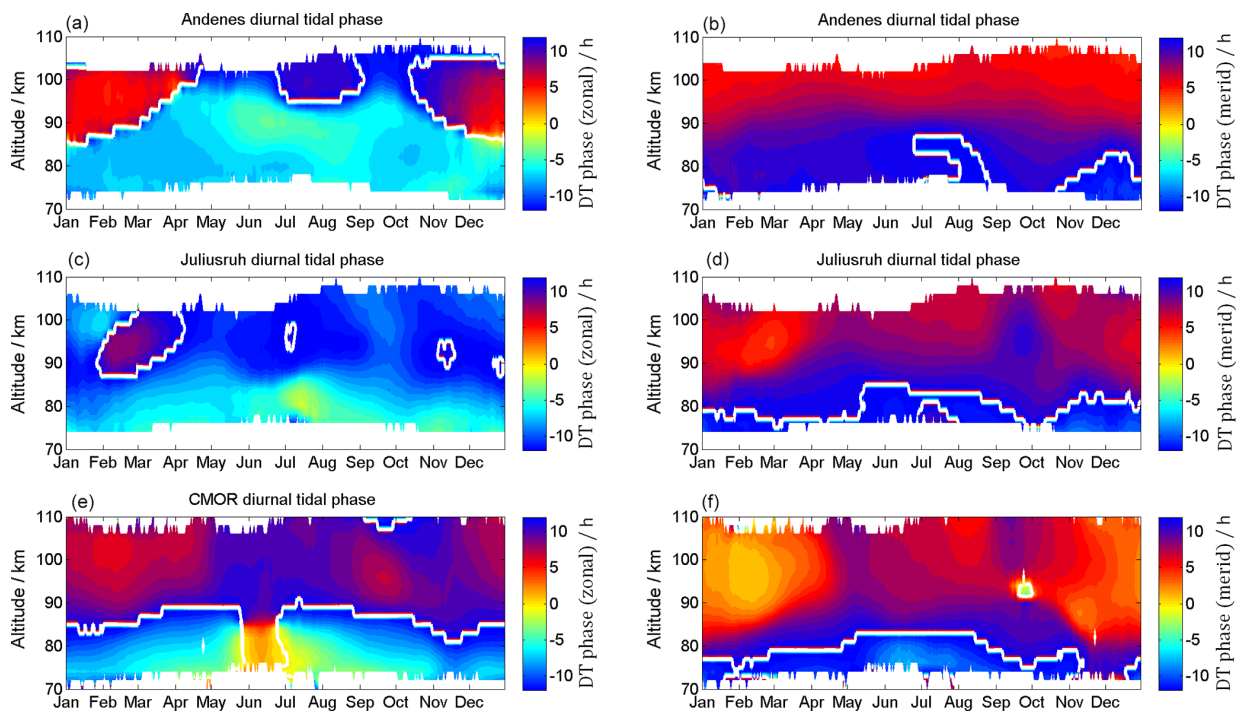


Figure 9. Composites of the zonal (a, c, e) and meridional (b, d, f) diurnal phase information for Andenes (a, b), Juliusruh (c, d), and CMOR (e, f).

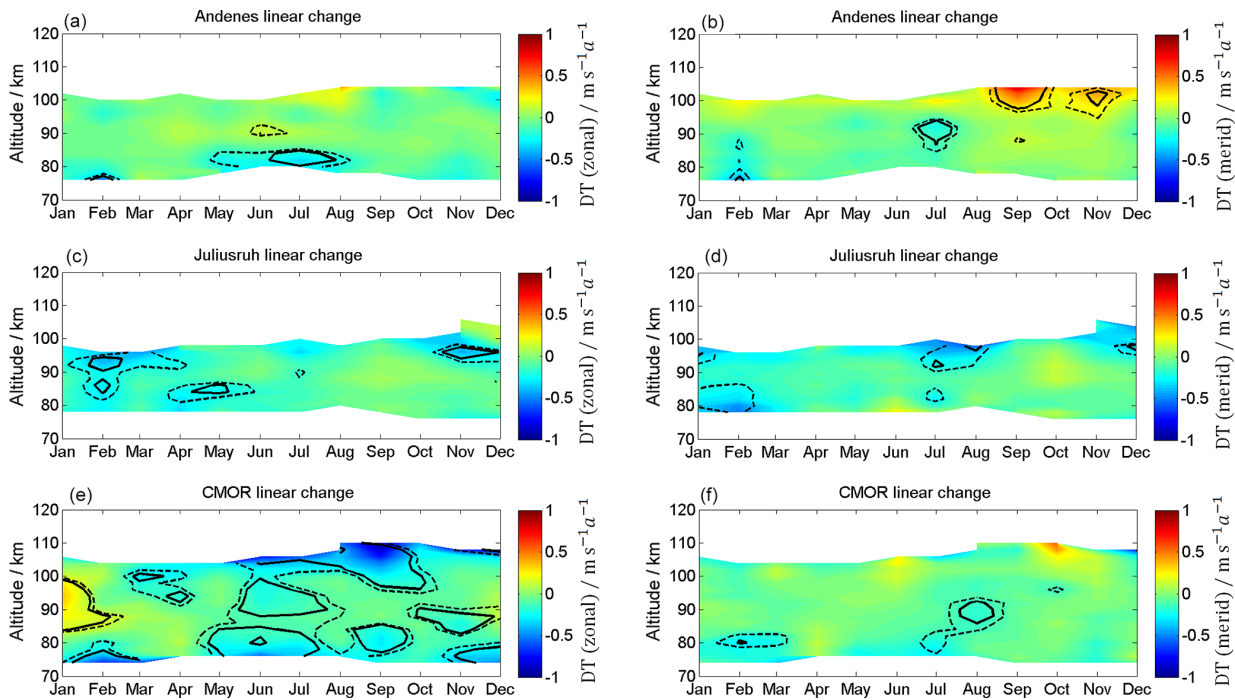


Figure 10. Linear long-term changes in zonal (a, c, e) and meridional (b, d, f) diurnal tidal components for Andenes (a, b), Juliusruh (c, d), and CMOR (e, f). The solid black lines correspond to 95 % significance, the dashed black lines to the 90 % significance.

until the spring. These enhanced values are remarkable because during the time after the autumn transition the tidal amplitudes are quite low (see Fig. 12), which indicates an increased response to the solar cycle for this period of the year. The modulation of the semidiurnal tidal amplitudes due to the solar cycle forcing ranges between 3 and 6 m s^{-1} for the winter season. Considering that some of the previous tidal climatologies are compiled during different phases of a solar cycle explains some of the discrepancies (Jacobi, 2012; Pokhotelov et al., 2018).

The phase information for the solar cycle can be found in the Appendix. The phase is referenced to the year 2002. The yellowish to light orange color indicates a zero phase shift compared to the reference year and corresponds to the maximum solar activity during solar cycle 23 (e.g., F10.7 or sunspot number). Phases that are outside the 90 % confidence interval are shaded and should not be treated as reliable due to the weak signal. The phase behavior itself seems to be rather complex and depends on season and altitude. The phase pattern of mean winds also shows a strong latitude dependence in both wind components. Only the winter season exhibits similarities in the response to the solar cycle of the sun with respect to the phase behavior. There is a certain coherence of the phases between the latitudes, in particular for the semidiurnal tide, which indicates a pronounced phase offset between September/October and December/January, which requires further investigation. However, the diurnal

tide is basically only affected at the CMOR station and shows phases close to zero corresponding to a more or less direct response to the solar forcing. A more detailed discussion of the phase behavior and the potential causes requires modeling and is beyond the scope of this paper.

6 Discussion

We have used meteor radar observations to characterize the mesospheric and lower thermospheric (MLT) winds, tides, gravity waves, and planetary waves for the northern high-latitude site of Andenes and the northern mid-latitude sites of Juliusruh and CMOR. Based on measurements between the years 2002 and 2018, long-term changes (LTCs) were estimated for winds and tides at each location. Depending on the length of the data series, the latitudinal location, and the observed heights, long-term tendencies can differ significantly with latitude.

For the mean zonal and meridional wind, the typical wind pattern occurs with eastward-directed winds during the winter and a switch from westward to eastward winds during the summer. The transition heights were located at lower heights for the mid-latitude locations. Changes between northward-directed winds in the winter and southward winds during the summer were apparent from all the measurements. Furthermore, above 100 km a westward-directed wind field occurs only for CMOR after the autumn transition, which lasts un-

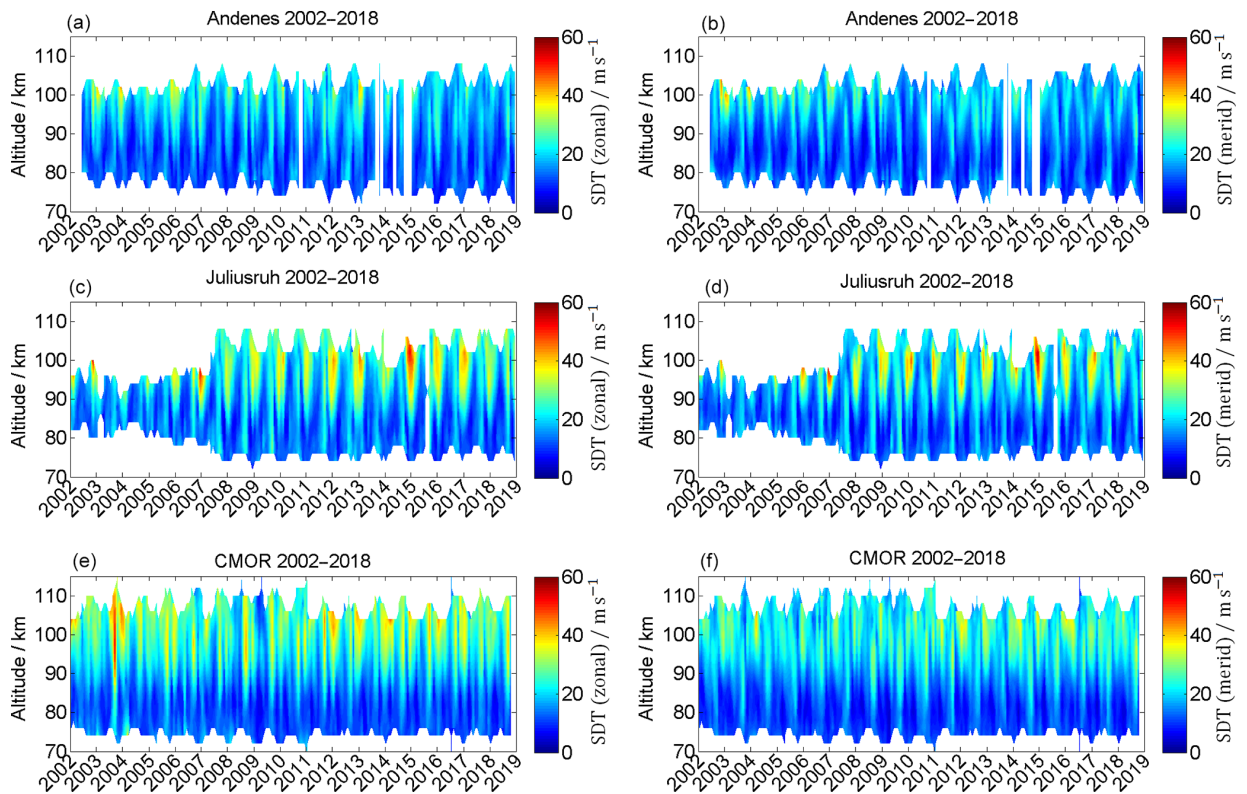


Figure 11. Same as Fig. 7 but for the semidiurnal tidal components.

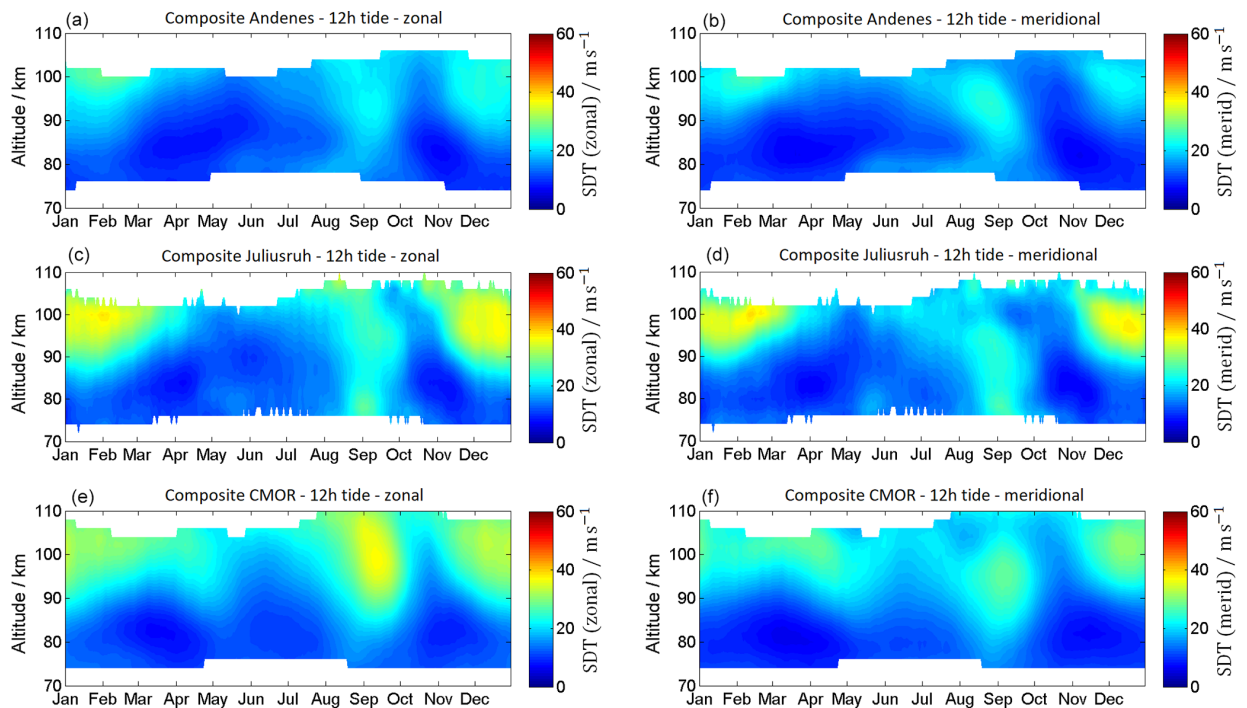


Figure 12. Same as Fig. 8 but for the semidiurnal tidal components.

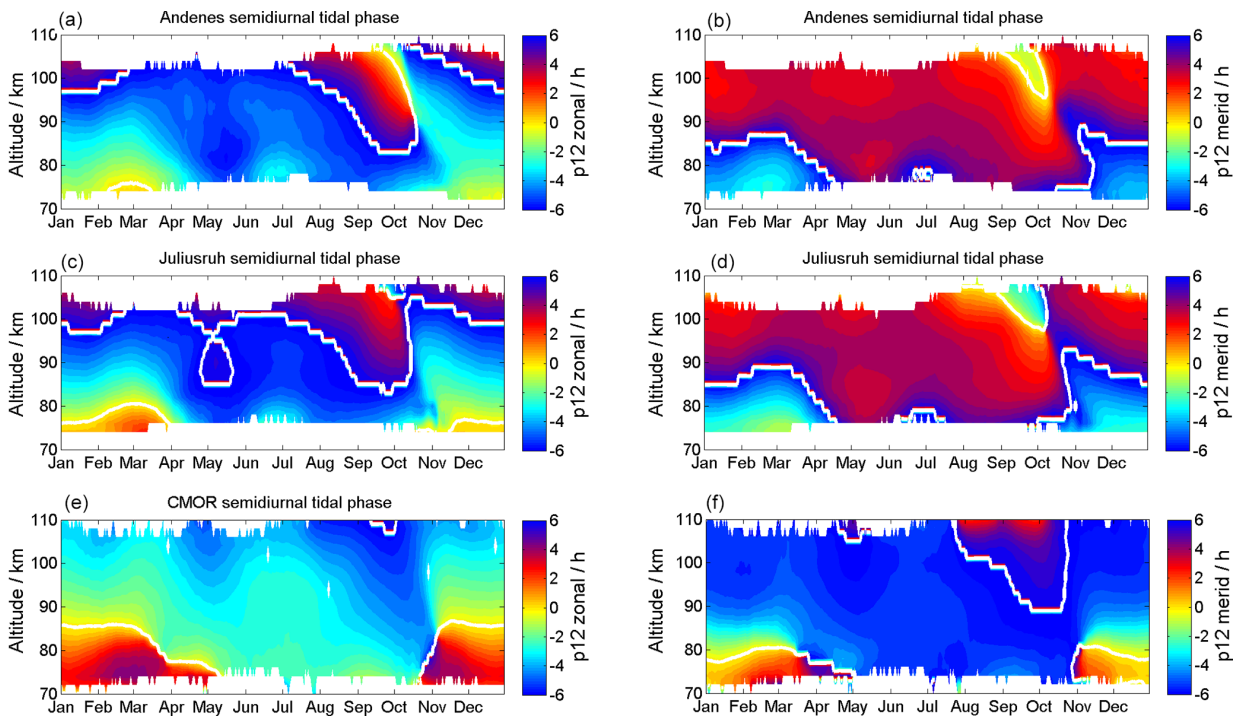


Figure 13. Same as Fig. 9 but for the semidiurnal tidal components.

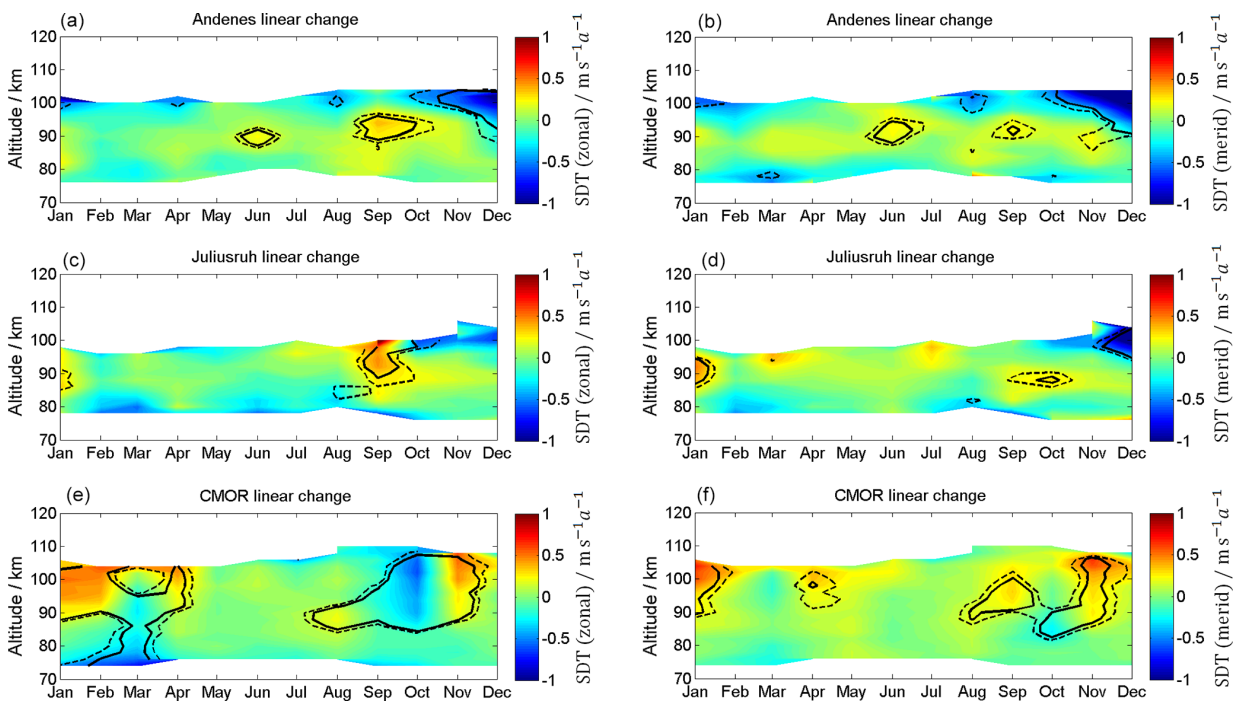


Figure 14. Same as Fig. 10 but for the semidiurnal tidal components.

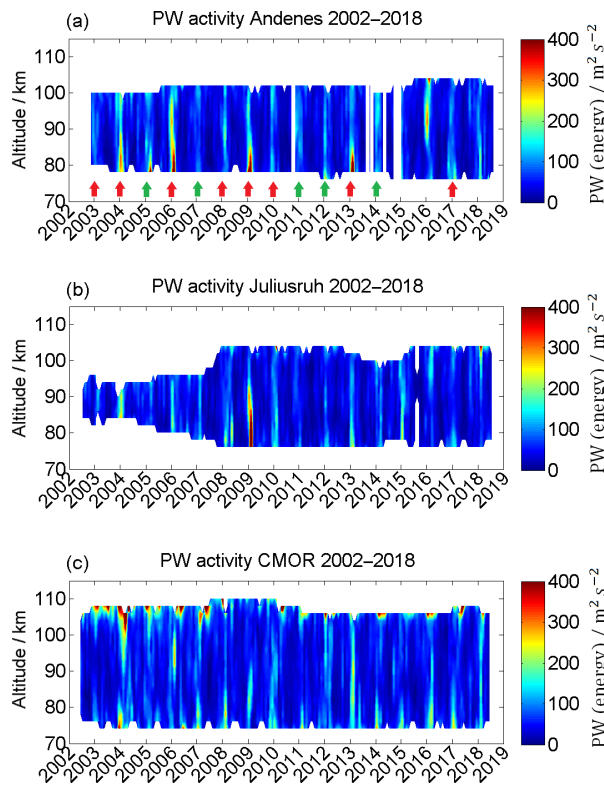


Figure 15. Time series of planetary wave energy for Andenes (a), Juliusruh (b), and CMOR (c). The red (green) bold arrows correspond to winter with a major (minor) sudden stratospheric warming.

til the spring transition. These climatologies fit generally to model studies made by, e.g., Jacobi et al. (2009) and Geißler and Jacobi (2017), or to the results of remote-sensing instruments by Schminder and Kürschner (1994). However, some of these studies show smaller differences in the wind values than we find, which we ascribe to different time series or disparities in the window fit length.

Based on annual mean values, the winds in the MLT over Andenes show a tendency of decreasing amplitude for the zonal and meridional components. In contrast, the mid-latitude locations show weaker tendencies or only increasing tendencies above a certain altitude. Stronger differences occur when comparing seasonal tendencies for each location, where in some cases opposite tendencies for the same height and same season can occur. Comparing these tendencies with previous studies, differences are to be expected based on differently used time series and on different averaging periods. Enhancements or weakenings of the mean zonal wind are also expected to take place due to several geophysical processes, such as the quasi-biennial oscillation or the El Niño–Southern Oscillation, which are not incorporated in some studies.

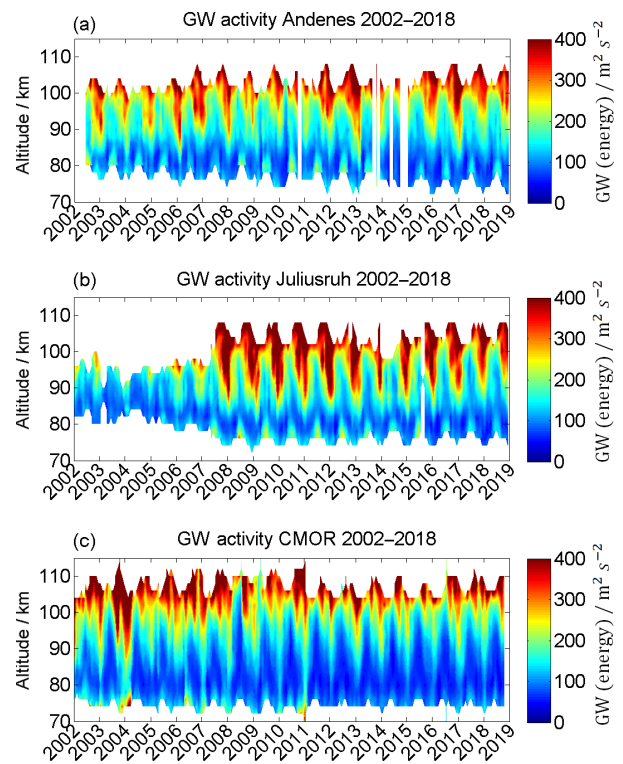


Figure 16. Time series of kinetic gravity wave energy for Andenes (a), Juliusruh (b), and CMOR (c).

In Hoffmann et al. (2011) long-term tendencies were measured based on medium-frequency meteor radar for the location of Juliusruh. They found a similar increasing tendency during the autumn but a different tendency during the spring. This difference may be due to the particular time series they used, namely from 1990 until 2010. In the work by Jacobi et al. (2015), LTCs were estimated for the Collm mid-latitude meteor radar station (Germany) for the years 2004 until 2014. They used monthly mean meteor measurements and found tendencies similar to our work for the winter through to the summer months for both wind components. However, they reported an opposite LTC for the meridional component during autumn compared to our results. Using the MUAM model (Geißler and Jacobi, 2017) also shows the northward tendency during the summer for both mid-latitude MRs, based on trends over a 37-year period. In addition, they found a strong opposite LTC for summer at Andenes.

Concerning tides, we find that the observed SDT component dominates over the DT component at Andenes and Juliusruh but reaches nearly similar zonal amplitudes for the lower-latitude location of CMOR. The amplitudes of the meridional diurnal component exceeds the value of the SDT for heights above 100 km. The diurnal component is characterized by a second enhancement during the summer, while

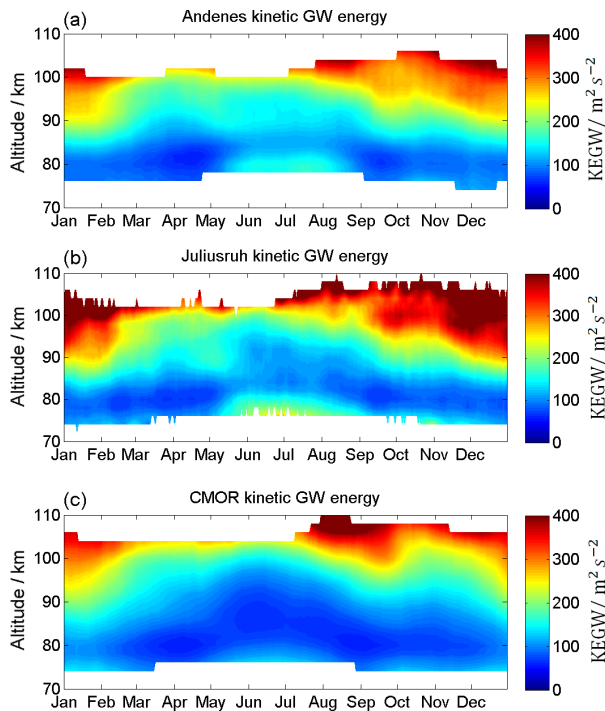


Figure 17. Composite of kinetic gravity wave energy for Andenes (a), Juliusruh (b), and CMOR (c).

the SDT component shows an increase in amplitude during the autumn transition at all locations.

The amplitudes and the seasonal occurrence of tides, especially the SDT, correspond well to an earlier study made by Manson et al. (2009). Their work covered 1 year with the SDT and DT reported for several northern latitude locations. Similar to the case for the winds, the seasonal LTC pattern differs by location. While for the tidal components Andenes and Juliusruh show similar changes, CMOR shows somewhat opposite tendencies. Similar climatologies for the SDT tides were found at the latitude of $\sim 40^\circ$ N based on model results and lidar measurements in several earlier studies (e.g., Yuan et al., 2008a). Later, Pokhotelov et al. (2018) showed agreement between model data and radar SDT tidal measurements for the locations of Andenes and Juliusruh. For diurnal tides, Portnyagin et al. (2004) found similar amplitudes and also a small enhancement during the summer at around 80 km based on medium-frequency radar measurements of the diurnal tides between 1990 and 2000.

The climatology of tidal phases for the DT and SDT points out that the tidal phases are not very stable at the MLT and are more or less continuously changing throughout the course of the year. In particular, the rapid phase changes during the fall transition and the winter months (DJF) for the SDT are critical for many other analysis using long windows to determine tidal features. Typically, such long windows are used to separate the lunar tide from the SDT (Chau et al., 2015;

Conte et al., 2017). However, Fuller-Rowell et al. (2016) already pointed out that the phase stability is highly important in such an analysis. They found a lunar tide in model data (Whole Atmosphere Model – WAM) as a result of a drifting phase of the SW2 and TW3 tide during an SSW.

For each of the three locations in our study, the planetary wave energy shows abnormally high peak values during the winter when sudden stratospheric warming also is present. According to Matsuno (1971) these warmings are caused by the interaction of upward-propagating planetary waves. The values we find for the planetary wave energy correspond well to earlier studies (e.g., Tsuda et al., 1988), with similar values for the kinetic energy reported by Dowdy et al. (2007). The kinetic gravity wave energy for each location shows larger values at higher altitudes and also during the winter, with values of up to $400 \text{ m}^2 \text{ s}^{-2}$. The summer gravity wave energy enhancement, which occurred in Juliusruh at around 80 km, can also partly be seen with the use of medium-frequency radar data. It is even more apparent with the use of model data (Hoffmann et al., 2010).

The 11-year oscillation is found to affect both the observed winds and tides. The strongest influence is on the zonal wind during the solstices. A study made by Keuer et al. (2007) suggests that for the location of Juliusruh, the strongest influences of solar radiation on the zonal wind should be at 80 km than above during the winter, as well as nearly similar influences for all heights during the summer. Their work suggests that the meridional component should show no impact from solar radiation on the winds. Both findings correspond well to our results. For the tidal diurnal component, particularly at the lower mid-latitude location of CMOR, there is a strong influence from the 11-year oscillation for heights above ~ 95 km, while for the SDT components all three MRs show a noticeable response to the 11-year oscillation during the winter for heights above 90 km.

7 Conclusions

Measuring long-term climatologies (LTCs) in the atmosphere requires continuous and consistent observations. In this study, we analyzed observations from three MRs at Andenes, Juliusruh, and CMOR (Canada) at mid and high latitudes to obtain LTC in mean winds, diurnal and semidiurnal tides, gravity waves and planetary waves, and their latitudinal dependence for the time period between January 2002 and December 2018.

The focus of this study is to characterize the LTC and solar cycle effects on mean winds, atmospheric tides, and gravity wave and planetary wave energy at three different latitudes. Our results demonstrate that it is valuable to sustain continuous observations at the MLT region at several locations as there is no common LTC or solar cycle response. Although we provide confidence levels with our measurements, the uncertainties depend on the chosen time windows. However, the

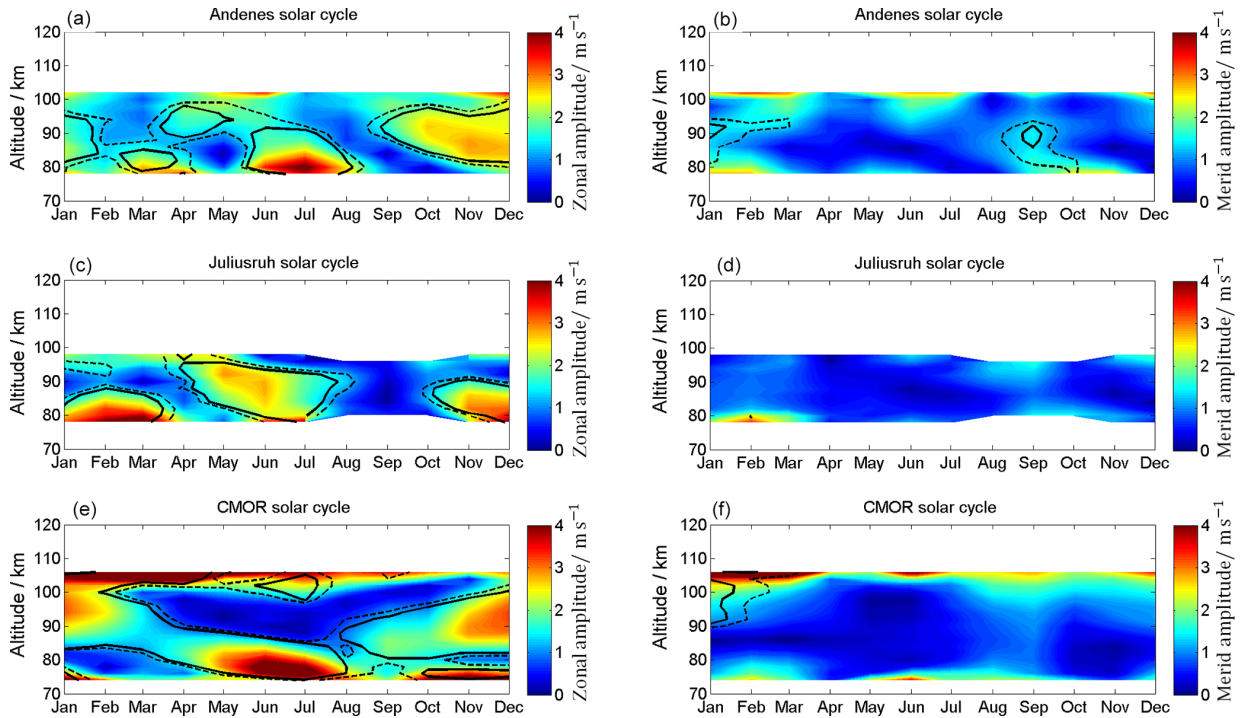


Figure 18. Linear change in the solar radiation on the zonal (a, c, e) and meridional (b, d, f) wind for Andenes (a, b), Juliusruh (c, d), and CMOR (e, f). The solid black lines correspond to 95 % significance, the dashed black lines to the 90 % significance.

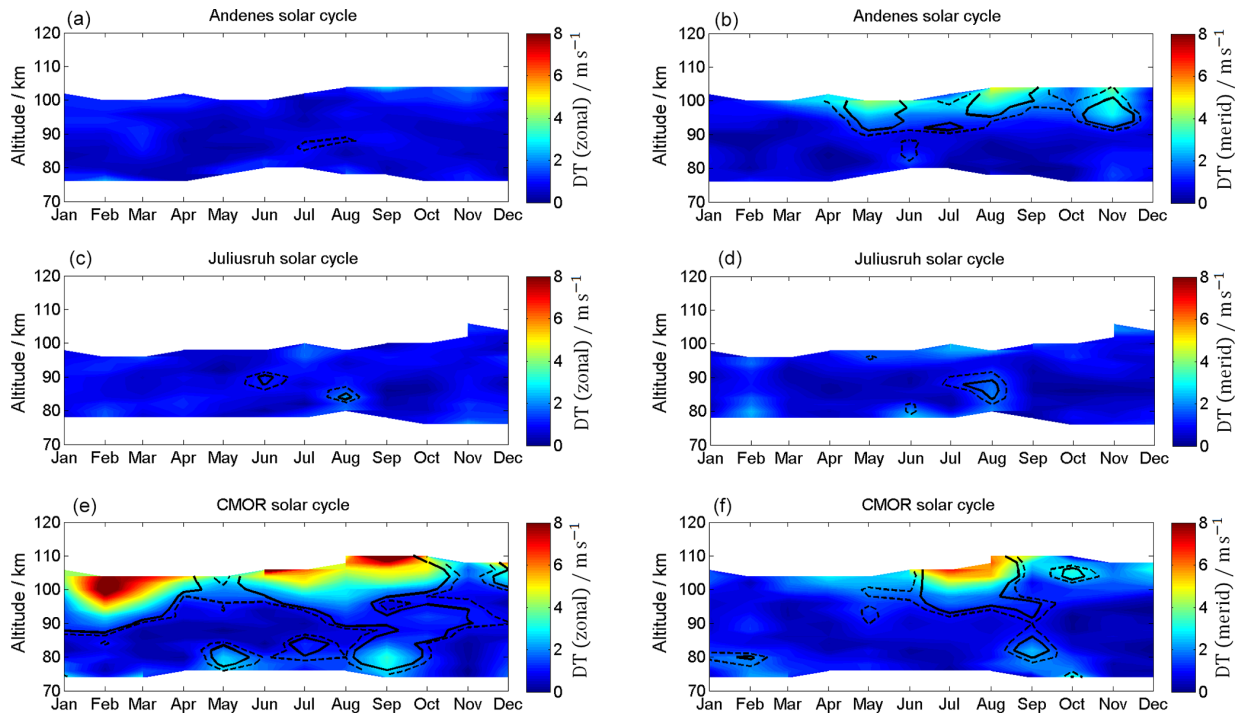


Figure 19. Linear change in an 11-year oscillation on the diurnal zonal (a, c, e) and meridional (b, d, f) tidal components for Andenes (a, b), Juliusruh (c, d), and CMOR (e, f). The solid black lines corresponds to 95 % significance, the dashed black lines to the 90 % significance.

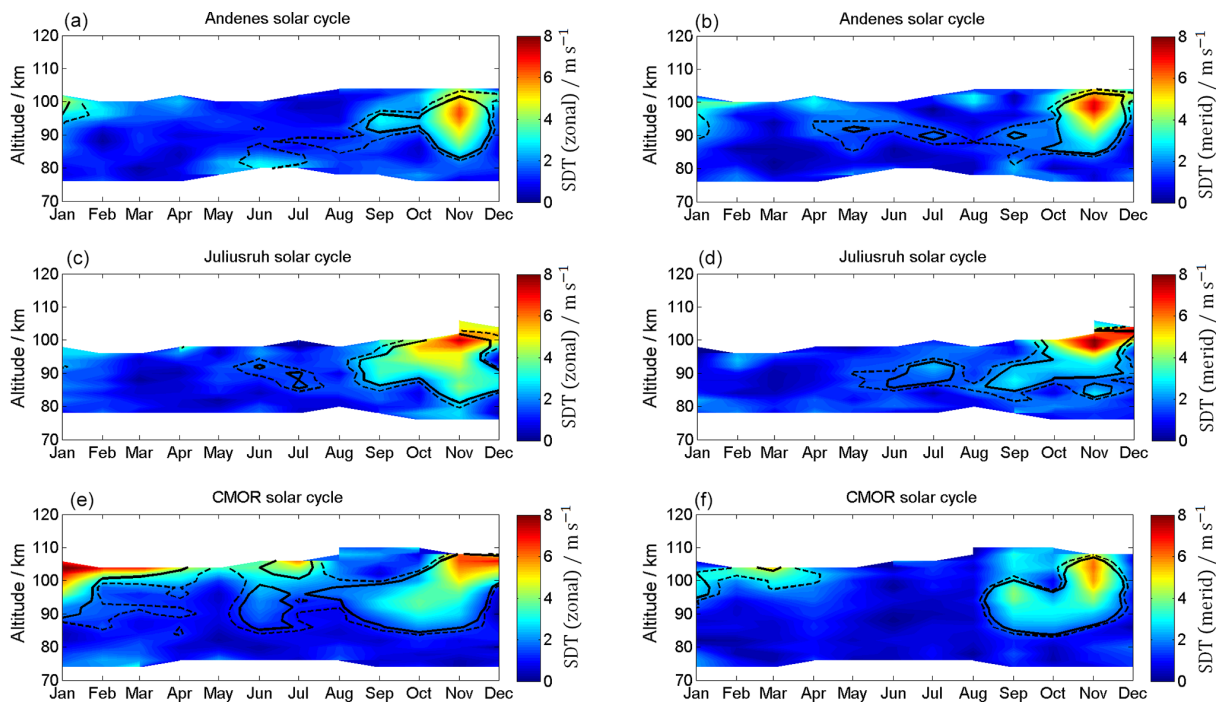


Figure 20. Same as Fig. 19 but for the semidiurnal component.

very long data sets used in our study show that there is a significant year-to-year variability.

Our main specific conclusions are the following.

- Mean wind climatologies show similar patterns between the mid and high latitudes. However, there is a clear latitudinal dependence of the summer zonal mesospheric jet reversal altitudes from westward to eastward winds, which increases with increasing latitude. There are also remarkable differences in the eastward zonal winds during the winter time (December–February), which decreases with latitude as well. However, only the Canadian MR shows a zonal wind reversal to westward winds above 100 km altitude. Meridional wind climatologies also reflect the latitudinal dependence, with northward winds during winter and southward winds in summer. In particular, the magnitude of the southward wind increases with decreasing latitude and the altitude of the meridional jet corresponds to the altitude behavior of the summer zonal wind reversal.
- The linear change in the zonal and meridional seasonal winds indicates different latitudinal tendencies for each month and component. The most prominent changes are the southward acceleration of the meridional winds at Andenes, the northward acceleration and, thus, weakening of the southward meridional winds at Juliusruh from June to September. CMOR shows the strongest linear response in the zonal wind component, with an intensi-

fying summer eastward jet above 84 km and a weakening of the zonal westward winds below.

- The yearly mean winds show only weak linear changes at CMOR and Juliusruh. At Andenes, the yearly mean wind speed seems to become more southward and westward with altitude.
- Diurnal tides show a strong polarization between the zonal and meridional components. Above Andenes and Juliusruh the meridional tide amplitude exceeds the zonal component. The diurnal tide shows only a weak latitudinal dependence of the meridional component but a significant increase in the zonal amplitude at the latitude of CMOR. Diurnal tides indicate almost no significant linear changes at the investigated latitudes.
- The climatology of the semidiurnal tide shows the highest amplitudes at mid latitudes above Juliusruh and a similar pattern at all latitudes. The semidiurnal tide shows a similar pattern, regarding occurrence and magnitude, of the zonal and meridional components. Only during the fall transition above the CMOR MR does the semidiurnal tide not show comparable values in amplitude and occurrence time. During September the zonal amplitude exceeds the meridional component.
- Semidiurnal tides show latitudinally dependent linear responses. Above Andenes and during the winter

- months (November, December) the SDT amplitude decreases with about $10 \text{ m s}^{-1} \text{ decade}^{-1}$ amplitude above 90 km altitude. Mid-latitude station Juliusruh exhibits almost no significant linear change in the SDT. The CMOR mid-latitude station shows the most significant linear changes in the SDT. During the winter months (November, December, January) SDT amplitudes increase by $5 \text{ m s}^{-1} \text{ decade}^{-1}$. Further, SDT amplitudes during the fall transition (October) seem to be further weakening.
- The climatology of the tidal phases for the diurnal tide and the semidiurnal tide is not very stable. They change continuously through the year. Phase changes for the semidiurnal tide occur especially during the fall transition and the winter.
 - The planetary wave activity shows a large year-to-year variability and latitudinal dependence, with the strongest activity at the polar latitudes. Juliusruh and CMOR MR indicate a weaker mean activity compared to Andenes.
 - The gravity wave activity also shows a distinct seasonal pattern at all three latitudes, with a maximum during the winter months (December, January, February) and late summer (September) above 90 km. Andenes and Juliusruh exhibit a secondary much weaker enhancement in June, July, and August below 80 km altitude. CMOR shows a significant increase in the GW energies at higher altitudes compared to the other two stations.
 - The mean winds also exhibit a significant amplitude response to an 11-year oscillation. In particular, the zonal mean winds show a characteristic seasonal solar cycle effect. During summer all three stations exhibit an 11-year oscillation with an amplitude of $3\text{--}5 \text{ m s}^{-1}$ in the zonal component below 82 km altitude. The winter months (November, December, January, February) show a solar cycle response below 82 km at mid and high latitudes and from November to December a relevant solar cycle amplitude between 84 and 95 km at Andenes and CMOR.
 - The solar cycle response to the DT is less prominent. Andenes shows some weak amplitude modulation in the meridional component above 90 km between April and November. Almost no solar cycle effect is visible above Juliusruh. CMOR shows the strongest solar cycle effect in both wind components during summer above 95 km altitude and in the zonal component from January to April.
 - The SDT exhibits a clear 11-year response at mid and high latitudes. The SDT zonal and meridional winds show a similar pattern of the confidence levels and amplitudes. All three stations exhibit a strong solar cycle amplitude of $5\text{--}8 \text{ m s}^{-1}$ from October to November and in the altitude range between 84 and 100 km. The Canadian station also presents a significant change from January to March above 100 km.
 - DT and SDT phases show a characteristic seasonal behavior. The temporal evolution of the phases indicates continuous changes throughout the course of the year. SDT phases show rapid phase changes during the fall transition and at polar latitudes during the winter months (DJF). The mean phase behavior as well as the continuous changes should be considered by analyzing the lunar tides.
 - Mean winds, DT, and SDT show a season-dependent solar cycle effect and considerable different seasonal-phase responses to the solar forcing. In particular, the SDT fall transition is characterized by an anticorrelation in September/October with the solar activity, whereas the winter months (DJF) seem to respond more directly to the solar forcing (e.g., F10.7 or sunspot number).

Data availability. The Andenes and Juliusruh radar data are available upon request from Gunter Stober (stober@iap-kborn.de, gunter.stober@iap.unibe.ch). The CMOR radar data are available upon request from Peter Brown (pbrown@uwo.ca).

Appendix A

Besides the amplitude information of the solar cycle fitting (Figs. 18–20), we also computed the phase information. These are shown for the wind component in Fig. A1, for the diurnal tidal phase in Fig. A2, and for the semidiurnal tidal-phase component in Fig. A3. The shaded areas are not significant. It turned out to be a very complex situation of all the different features as described in Sect. 5. Some of them seem to be correlated with the solar cycle and others anticorrelated. The phase behavior reflects a very complex time and altitude pattern that can also be observed in the solar cycle amplitude plots.

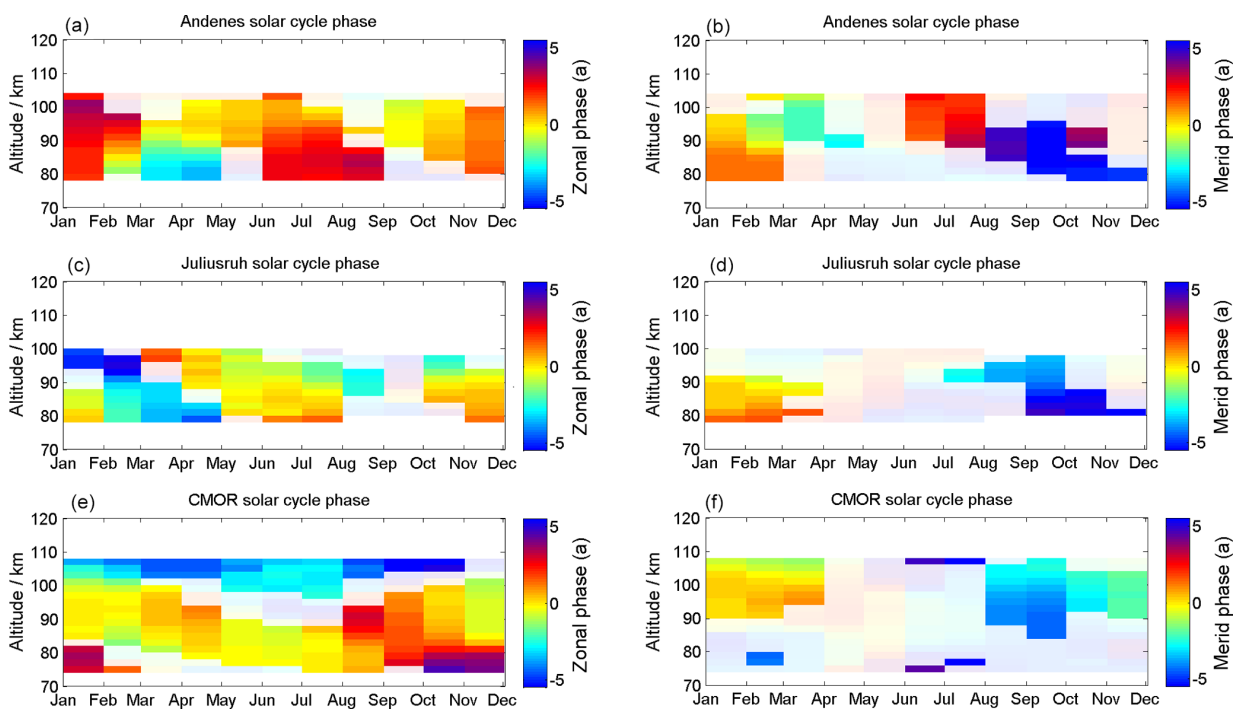


Figure A1. Phase information of the solar cycle fit for the wind component. The shaded areas are not significant.

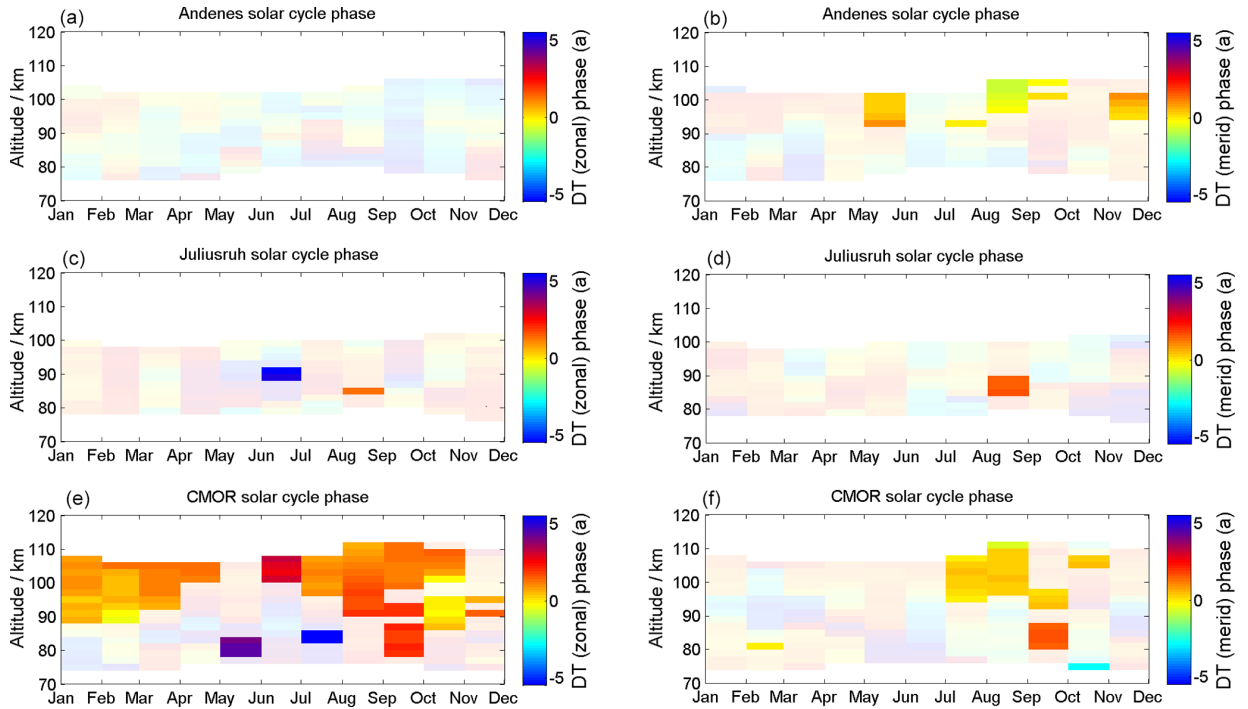


Figure A2. Same as Fig. A1 but for the diurnal component.

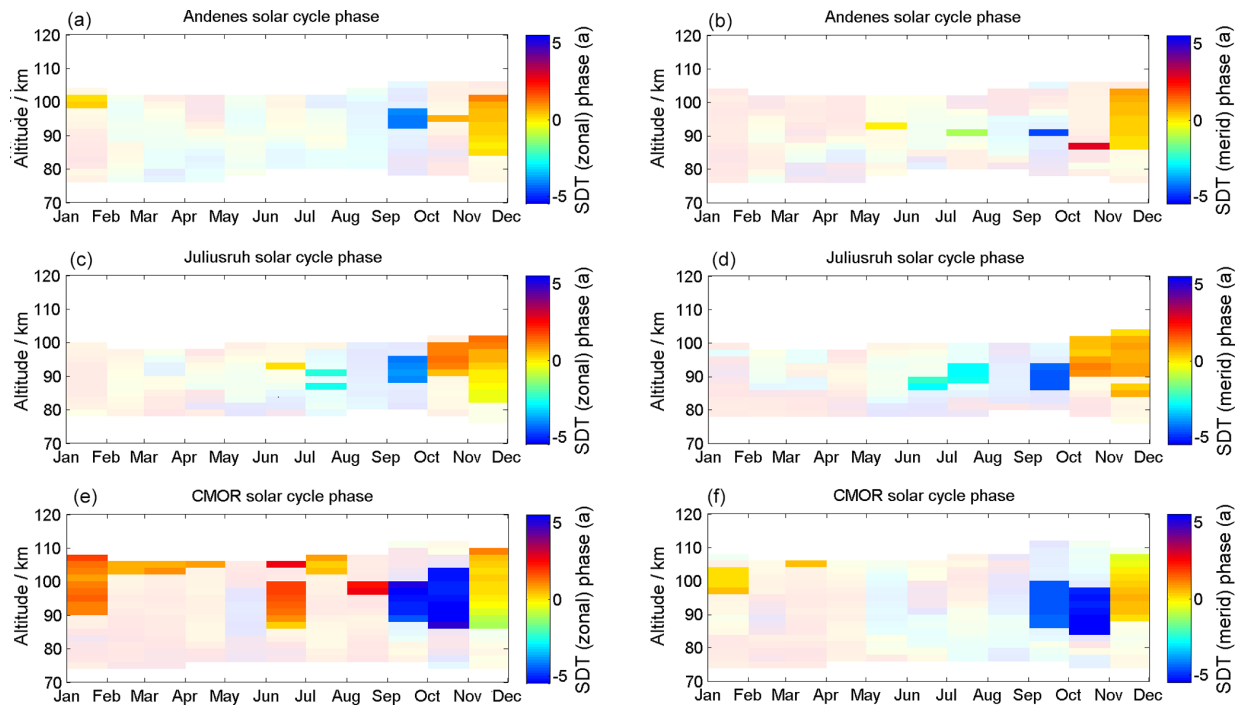


Figure A3. Same as Fig. A1 but for the semidiurnal component.

Author contributions. SW wrote the manuscript with input from all the authors. Furthermore, all the co-authors contributed to the data interpretation. GS provided the high-resolution meteor wind data analysis for all the stations and ensured the operation of the Andenes and Juliusruh meteor radar. PB ensures the operation of the CMOR meteor radar.

Competing interests. The authors declare that they have no conflict of interest.

Acknowledgements. This work was partly supported by the WATILA project (SAW-2015-IAP-1 383) and partly by the Deutsche Forschungsgemeinschaft (DFG, German Research Foundation; project no. LU1174, PACOG as part of the MS-GWaves research unit). Furthermore, we acknowledge the IAP technicians for the technical support. We are thankful for discussions with Peter Hoffmann.

Financial support. The publication of this article was funded by the Open Access Fund of the Leibniz Association.

Review statement. This paper was edited by Dalia Buresova and reviewed by two anonymous referees.

References

- Baumgarten, K. and Stober, G.: On the evaluation of the phase relation between temperature and wind tides based on ground-based measurements and reanalysis data in the middle atmosphere, *Ann. Geophys.*, 37, 581–602, <https://doi.org/10.5194/angeo-37-581-2019>, 2019.
- Baumgarten, K., Gerding, M., Baumgarten, G., and Lübken, F.-J.: Temporal variability of tidal and gravity waves during a record long 10-day continuous lidar sounding, *Atmos. Chem. Phys.*, 18, 371–384, <https://doi.org/10.5194/acp-18-371-2018>, 2018.
- Becker, E.: Dynamical Control of the Middle Atmosphere, *Space Sci. Rev.*, 168, 283–314, <https://doi.org/10.1007/s11214-011-9841-5>, 2012.
- Beig, G.: Long-term trends in the temperature of the mesosphere/lower thermosphere region: 1. Anthropogenic influences, *J. Geophys. Res.*, 116, A00H11, 2011.
- Brown, P., Weryk, R., Wong, D., and Jones, J.: A meteoroid stream survey using the Canadian Meteor Orbit Radar: I. Methodology and radiant catalogue, *Icarus*, 195, 317–339, <https://doi.org/10.1016/j.icarus.2007.12.002>, 2008.
- Chau, J. L., Hoffmann, P., Pedatella, N. M., Matthias, V., and Stober, G.: Upper mesospheric lunar tides over middle and high latitudes during sudden stratospheric warming events, *J. Geophys. Res.-Space Phys.*, 120, 3084–3096, <https://doi.org/10.1002/2015JA020998>, 2015.
- Conte, J. F., Chau, J. L., Stober, G., Pedatella, N., Maute, A., Hoffmann, P., Janches, D., Fritts, D., and Murphy, D. J.: Climatology of semidiurnal lunar and solar tides at middle and high latitudes: Interhemispheric comparison, *J. Geophys. Res.-Space Phys.*, 122, 7750–7760, <https://doi.org/10.1002/2017JA024396>, 2017.
- Conte, J. F., Chau, J. L., Laskar, F. I., Stober, G., Schmidt, H., and Brown, P.: Semidiurnal solar tide differences between fall and spring transition times in the Northern Hemisphere, *Ann. Geophys.*, 36, 999–1008, <https://doi.org/10.5194/angeo-36-999-2018>, 2018.
- Dowdy, A., Vincent, R. A., Tsutsumi, M., Igarashi, K., Murayama, Y., Singer, W., and Murphy, D. J.: Polar mesosphere and lower thermosphere dynamics: 1. Mean wind and gravity wave climatologies, *J. Geophys. Res.-Atmos.*, 112, D17104, <https://doi.org/10.1029/2006JD008126>, 2007.
- Eckermann, S. D., Broutman, D., Ma, J., Doyle, J. D., Pautet, P. D., Taylor, M. J., Bossert, K., Williams, B. P., Fritts, D. C., and Smith, R. B.: Dynamics of Orographic Gravity Waves Observed in the Mesosphere over the Auckland Islands during the Deep Propagation Gravity Wave Experiment (DEEPWAVE), *J. Atmos. Sci.*, 73, 3855–3876, <https://doi.org/10.1175/JAS-D-16-0059.1>, 2016.
- Egito, F., Andrioli, V., and Batista, P.: Vertical winds and momentum fluxes due to equatorial planetary scale waves using all-sky meteor radar over Brazilian region, *J. Atmos. Solar-Terr. Phys.*, 149, 108–119, <https://doi.org/10.1016/j.jastp.2016.10.005>, 2016.
- Emmert, J. T., Picone, J. M., and Meier, R. R.: Thermospheric global average density trends, 1967–2007, derived from orbit of 5000 near-Earth objects, *Geophys. Res. Lett.*, 35, L05101, <https://doi.org/10.1029/2007GL032809>, 2008.
- Fritts, D. C. and Alexander, M. J.: Gravity wave dynamics and effects in the middle atmosphere, *Rev. Geophys.*, 41, 1003, <https://doi.org/10.1029/2001RG000106>, 2003.
- Fritts, D. C. and VanZandt, T. E.: Spectral Estimates of Gravity Wave Energy and Momentum Fluxes. Part I: Energy Dissipation, Acceleration, and Constraint., *J. Atmos. Sci.*, 50, 3685–3694, [https://doi.org/10.1175/1520-0469\(1993\)050<3685:SEOGWE>2.0.CO;2](https://doi.org/10.1175/1520-0469(1993)050<3685:SEOGWE>2.0.CO;2), 1993.
- Fuller-Rowell, T. J., Fang, T.-W., Wang, H., Matthias, V., Hoffmann, P., Hocke, K., and Studer, S.: Impact of Migrating Tides on Electrodynamic During the January 2009 Sudden Stratospheric Warming, chap. 14, pp. 163–174, American Geophysical Union (AGU), <https://doi.org/10.1002/9781118929216.ch14>, 2016.
- Geißler, C. and Jacobi, C.: Mesospheric wind and temperature trends simulated with MUAM, *Meteorologische Arbeiten aus Leipzig*, 22, ISBN 978-3-9814401-3-3, 2017.
- Hagan, M. E. and Forbes, J. M.: Migrating and nonmigrating diurnal tides in the middle and upper Atmosphere excited by tropospheric latent heat release, *J. Geophys. Res.*, 107, 4754, <https://doi.org/10.1029/2001JD001236>, 2002.
- Hocking, W. K., Fuller, B., and Vandeppeer, B.: Realtime determination of meteor-related parameters utilizing modern digital technology, *J. Atmos. Solar-Terr. Phys.*, 69, 155–169, [https://doi.org/10.1016/S1364-6826\(00\)00138-3](https://doi.org/10.1016/S1364-6826(00)00138-3), 2001.
- Hoffmann, P., Becker, E., Singer, W., and Placke, M.: Seasonal variation of mesospheric waves at northern middle and high latitudes, *J. Atmos. Solar-Terr. Phys.*, 72, 1068–1079, <https://doi.org/10.1016/j.jastp.2010.07.002>, 2010.
- Hoffmann, P., Rapp, M., Singer, W., and Keuer, D.: Trends of mesospheric gravity waves at northern middle latitudes during summer, *J. Geophys. Res.*, 116, D00P08, <https://doi.org/10.1029/2011JD015717>, 2011.

- Hysell, D., Fritts, D., Laughman, B., and Chau, J. L.: Gravity Wave-Induced Ionospheric Irregularities in the Postsunset Equatorial Valley Region, *J. Geophys. Res.*, 122, 579–590, <https://doi.org/10.1002/2017JA024514>, 2017.
- Iimura, H., Fritts, D. C., Tsutsumi, M., Nakamura, T., Hoffmann, P., and Singer, W.: Long-term observations of the wind field in the Antarctic and Arctic mesosphere and lower-thermosphere at conjugate latitudes, *J. Geophys. Res.*, 116, D20112, <https://doi.org/10.1029/2011JD016003>, 2011.
- Iimura, H., Fritts, D. C., Janches, D., Singer, W., and Mitchell, N. J.: Interhemispheric structure and variability of the 5-day planetary wave from meteor radar wind measurements, *Ann. Geophys.*, 33, 1349–1359, <https://doi.org/10.5194/angeo-33-1349-2015>, 2015.
- Jacobi, C.: 6 year mean prevailing winds and tides measured by VHF meteor radar over Collm (51.3° N, 13.0° E), *J. Atmos. Solar-Terr. Phys.*, 78–79, 8–18, <https://doi.org/10.1016/j.jastp.2011.04.010>, 2012.
- Jacobi, Ch., Hoffmann, P., and Kürschner, D.: Trends in MLT region winds and planetary waves, Collm (52° N, 15° E), *Ann. Geophys.*, 26, 1221–1232, <https://doi.org/10.5194/angeo-26-1221-2008>, 2008.
- Jacobi, C., Fröhlich, K., Portnyagin, Y., Merzlyakov, E., Solovjova, T., Makarov, N., Rees, D., Fahrutdinova, A., Guryanov, V., Fedorov, D., Korotyshkin, D., Forbes, J., Pogoreltsev, A., and Kürschner, D.: Semi-empirical model of middle atmosphere wind from the ground to the lower thermosphere, *Adv. Space Res.*, 43, 239–246, 2009.
- Jacobi, C., Lilienthal, F., Geißler, C., and Krug, A.: Long-term variability of mid-latitude mesosphere-lower thermosphere winds over Collm (51 N, 13 E), *J. Atmos. Solar-Terr. Phys.*, 136, 174–186, <https://doi.org/10.1016/j.jastp.2015.05.006>, 2015.
- Jones, J., Brown, P., Ellis, K., Webster, A., Campbell-Brown, M., Krzemenski, Z., and Weryk, R.: The Canadian Meteor Orbit Radar: system overview and preliminary results, *Planet. Space Sci.*, 53, 413–421, <https://doi.org/10.1016/j.pss.2004.11.002>, 2005.
- Keuer, D., Hoffmann, P., Singer, W., and Bremer, J.: Long-term variations of the mesospheric wind field at mid-latitudes, *Ann. Geophys.*, 25, 1779–1790, <https://doi.org/10.5194/angeo-25-1779-2007>, 2007.
- Kishore Kumar, G. and Hocking, W. K.: Climatology of northern polar latitude MLT dynamics: mean winds and tides, *Ann. Geophys.*, 28, 1859–1876, <https://doi.org/10.5194/angeo-28-1859-2010>, 2010.
- Laštovička, J., Solomon, S. C., and Qian, L.: Trends in the Neutral and Ionized Upper Atmosphere, *Space Sci. Rev.*, 168, 113–145, <https://doi.org/10.1007/s11214-011-9799-3>, 2012.
- Latteck, R., Singer, W., Morris, R. J., Hocking, W. K., Murphy, D. J., Holdsworth, D. A., and Swarnalingam, N.: Similarities and differences in polar mesosphere summer echoes observed in the Arctic and Antarctica, *Ann. Geophys.*, 26, 2795–2806, <https://doi.org/10.5194/angeo-26-2795-2008>, 2008.
- Lieberman, R. S. and Hays, P. B.: An estimate of the momentum deposition in the lower thermosphere by the observed diurnal tide., *J. Atmos. Sci.*, 51, 3094–3105, [https://doi.org/10.1175/1520-0469\(1994\)051<3094:AEOTMD>2.0.CO;2](https://doi.org/10.1175/1520-0469(1994)051<3094:AEOTMD>2.0.CO;2), 1994.
- Lindzen, R. S. and Chapman, S.: Atmospheric tides, *Space Sci. Rev.*, 10, 3–188, <https://doi.org/10.1007/BF00171584>, 1969.
- Lu, H., Gray, L. J., White, I. P., and Bracegirdle, T. J.: Stratospheric Response to the 11-Yr Solar Cycle: Breaking Planetary Waves, Internal Reflection, and Resonance, *J. Climate*, 30, 7169–7190, <https://doi.org/10.1175/JCLI-D-17-0023.1>, 2017.
- Lukianova, R., Kozlovsky, A., and Lester, M.: Climatology and inter-annual variability of the polar mesospheric winds inferred from meteor radar observations over Sodankylä (67 N, 23 E) during solar cycle 24, *J. Atmos. Solar-Terr. Phys.*, 171, 241–249, <https://doi.org/10.1016/j.jastp.2017.06.005>, 2018.
- Manson, A. H., Meek, C. E., Chshyolkova, T., Xu, X., Aso, T., Drummond, J. R., Hall, C. M., Hocking, W. K., Jacobi, Ch., Tsutsumi, M., and Ward, W. E.: Arctic tidal characteristics at Eureka (80° N, 86° W) and Svalbard (78° N, 16° E) for 2006/07: seasonal and longitudinal variations, migrating and non-migrating tides, *Ann. Geophys.*, 27, 1153–1173, <https://doi.org/10.5194/angeo-27-1153-2009>, 2009.
- Matsuno, T.: A Dynamical Model of the Stratospheric Sudden Warming, *J. Atmos. Sci.*, 28, 1479–1494, [https://doi.org/10.1175/1520-0469\(1971\)028<1479:ADMOTS>2.0.CO;2](https://doi.org/10.1175/1520-0469(1971)028<1479:ADMOTS>2.0.CO;2), 1971.
- Matthias, V. and Ern, M.: On the origin of the mesospheric quasi-stationary planetary waves in the unusual Arctic winter 2015/2016, *Atmos. Chem. Phys.*, 18, 4803–4815, <https://doi.org/10.5194/acp-18-4803-2018>, 2018.
- Middleton, H. R., Mitchell, N. J., and Muller, H. G.: Mean winds of the mesosphere and lower thermosphere at 52° N in the period 1988–2000, *Ann. Geophys.*, 20, 81–91, <https://doi.org/10.5194/angeo-20-81-2002>, 2002.
- Pedatella, N., Liu, H.-L., and Hagan, M.: Day-to-day migrating and nonmigrating tidal variability due to the six-day planetary wave, *J. Geophys. Res.*, 117, A06301, <https://doi.org/10.1029/2012JA017581>, 2012.
- Pokhotelov, D., Becker, E., Stober, G., and Chau, J. L.: Seasonal variability of atmospheric tides in the mesosphere and lower thermosphere: meteor radar data and simulations, *Ann. Geophys.*, 36, 825–830, <https://doi.org/10.5194/angeo-36-825-2018>, 2018.
- Portnyagin, Y. I., Solovjova, T. V., Makarov, N. A., Merzlyakov, E. G., Manson, A. H., Meek, C. E., Hocking, W., Mitchell, N., Pancheva, D., Hoffmann, P., Singer, W., Murayama, Y., Igarashi, K., Forbes, J. M., Palo, S., Hall, C., and Nozawa, S.: Monthly mean climatology of the prevailing winds and tides in the Arctic mesosphere/lower thermosphere, *Ann. Geophys.*, 22, 3395–3410, <https://doi.org/10.5194/angeo-22-3395-2004>, 2004.
- Portnyagin, Y. I., Merzlyakov, E. G., Solovjova, T. V., Jacobi, C., Kürschner, D., Manson, A., and Meek, C.: Long-term trends and year-to-year variability of mid-latitude mesosphere/lower thermosphere winds, *J. Atmos. Solar-Terr. Phys.*, 68, 1890–1901, <https://doi.org/10.1016/j.jastp.2006.04.004>, 2006.
- Qian, L., Jacobi, C., and McInerney, J.: Trends and Solar Irradiance Effects in the Mesosphere, *J. Geophys. Res.*, 124, 1343–1360, <https://doi.org/10.1029/2018JA026367>, 2019.
- Rind, D., Lean, J., Lerner, J., Lonergan, P., and Lebois-sitier, A.: Exploring the stratospheric/tropospheric response to solar forcing, *J. Geophys. Res.*, 113, D24103, <https://doi.org/10.1029/2008JD010114>, 2008.
- Salby, M. L. and Callaghan, P. F.: Influence of the Solar cycle on the General circulation of the Stratosphere and Upper Troposphere, *Space Sci. Rev.*, 124, 287–303, <https://doi.org/10.1007/s11214-006-9064-3>, 2006.

- Schminder, R. and Kürschner, D.: Permanent monitoring of the upper mesosphere and lower thermosphere wind fields (prevailing and semidiurnal tidal components) obtained from LF D1 measurements in 1991 at the Collm Geophysical Observatory, *J. Atmos. Terr. Phys.*, 56, 1263–1269, [https://doi.org/10.1016/0021-9169\(94\)90064-7](https://doi.org/10.1016/0021-9169(94)90064-7), 1994.
- Shibuya, R., Sato, K., Tsutsumi, M., Sato, T., Tomikawa, Y., Nishimura, K., and Kohma, M.: Quasi-12 h inertia-gravity waves in the lower mesosphere observed by the PANSY radar at Syowa Station (39.6° E, 69.0° S), *Atmos. Chem. Phys.*, 17, 6455–6476, <https://doi.org/10.5194/acp-17-6455-2017>, 2017.
- Stober, G. and Chau, J. L.: A multistatic and multifrequency novel approach for specular meteor radars to improve wind measurements in the MLT region, *Radio Sci.*, 50, 431–442, <https://doi.org/10.1002/2014RS005591>, 2015.
- Stober, G., Jacobi, C., and Keuer, D.: Distortion of meteor count rates due to cosmic radio noise and atmospheric particularities, *Adv. Radio Sci.*, 8, 237–241, <https://doi.org/10.5194/ars-8-237-2010>, 2010.
- Stober, G., Jacobi, C., Matthias, V., Hoffmann, P., and Gerdling, M.: Neutral air density variations during strong planetary wave activity in the mesopause region derived from meteor radar observations, *J. Atmos. Solar-Terr. Phys.*, 74, 55–63, <https://doi.org/10.1016/j.jastp.2011.10.007>, 2012.
- Stober, G., Matthias, V., Brown, P., and Chau, J. L.: Neutral density variation from specular meteor echo observations spanning one solar cycle, *Geophys. Res. Lett.*, 41, 6919–6925, <https://doi.org/10.1002/2014GL061273>, 2014.
- Stober, G., Matthias, V., Jacobi, C., Wilhelm, S., Höffner, J., and Chau, J. L.: Exceptionally strong summer-like zonal wind reversal in the upper mesosphere during winter 2015/16, *Ann. Geophys.*, 35, 711–720, <https://doi.org/10.5194/angeo-35-711-2017>, 2017.
- Stober, G., Chau, J. L., Vierinen, J., Jacobi, C., and Wilhelm, S.: Retrieving horizontally resolved wind fields using multi-static meteor radar observations, *Atmos. Meas. Tech.*, 11, 4891–4907, <https://doi.org/10.5194/amt-11-4891-2018>, 2018.
- Tsuda, T.: Characteristics of atmospheric gravity waves observed using the MU (Middle and Upper atmosphere) radar and GPS (Global Positioning System) radio occultation, *P. Jpn. Acad., B-Phys.*, 90, 12–27, <https://doi.org/10.2183/pjab.90.12>, 2014.
- Tsuda, T., Kato, S., and Vincent, R.: Long period wind oscillations observed by the Kyoto meteor radar and comparison of the quasi-2-day wave with Adelaide HF radar observations, *J. Atmos. Terr. Phys.*, 50, 225–230, [https://doi.org/10.1016/0021-9169\(88\)90071-2](https://doi.org/10.1016/0021-9169(88)90071-2), 1988.
- Tsuda, T., Nishida, M., Rocken, C., and Ware, R. H.: A Global Morphology of Gravity Wave Activity in the Stratosphere Revealed by the GPS Occultation Data (GPS/MET), *J. Geophys. Res.*, 105, 7257–7273, <https://doi.org/10.1029/1999JD901005>, 2000.
- Webster, A. R., Brown, P. G., Jones, J., Ellis, K. J., and Campbell-Brown, M.: Canadian Meteor Orbit Radar (CMOR), *Atmos. Chem. Phys.*, 4, 679–684, <https://doi.org/10.5194/acp-4-679-2004>, 2004.
- Yiğit, E. and Medvedev, A.: Internal wave coupling processes in Earth's atmosphere, *Adv. Space Res.*, 55, 983–1003, <https://doi.org/10.1016/j.asr.2014.11.020>, 2015.
- Yiğit, E. K. K. P., Georgieva, K., and Ward, W.: A review of vertical coupling in the Atmosphere–Ionosphere system: Effects of waves, sudden stratospheric warmings, space weather, and of solar activity, *J. Atmos. Solar-Terr. Phys.*, 141, 1–12, <https://doi.org/10.1016/j.jastp.2016.02.011>, 2016.
- Yuan, T., Schmidt, H., She, C. Y., Krueger, D. A., and Reising, S.: Seasonal variations of semidiurnal tidal perturbations in mesopause region temperature and zonal and meridional winds above Fort Collins, Colorado (40.6° N, 105.1° W), *J. Geophys. Res.*, 113, D20103, <https://doi.org/10.1029/2007JD009687>, 2008a.
- Yuan, T., She, C.-Y., Krueger, D. A., Sassi, F., Garcia, R., Roble, R. G., Liu, H.-L., and Schmidt, H.: Climatology of mesopause region temperature, zonal wind, and meridional wind over Fort Collins, Colorado (41° N, 105° W), and comparison with model simulations, *J. Geophys. Res.*, 113, D03105, <https://doi.org/10.1029/2007JD008697>, 2008b.

Appendix C Wilhelm et al. (2019b)

Wilhelm, S., Stober, G., Matthias, V., Jacobi, C., and Murphy, D. J.: Connection between the length of day and wind measurements in the mesosphere and lower thermosphere at mid- and high latitudes, *Ann. Geophys.*, 37, 1-14, <https://doi.org/10.5194/angeo-37-1-2019>, 2019.



Connection between the length of day and wind measurements in the mesosphere and lower thermosphere at mid- and high latitudes

Sven Wilhelm¹, Gunter Stober¹, Vivien Matthias², Christoph Jacobi³, and Damian J. Murphy⁴

¹Leibniz Institute of Atmospheric Physics, University of Rostock, Kühlungsborn, Germany

²Earth System Analysis – Research Domain 1, Potsdam Institute for Climate Impact Research, Potsdam, Germany

³Institute for Meteorology, Universität Leipzig, Leipzig, Germany

⁴Australian Antarctic Division, Kingston, Tasmania, Australia

Correspondence: Sven Wilhelm (wilhelm@iap-kborn.de)

Received: 24 May 2018 – Discussion started: 20 June 2018

Revised: 11 December 2018 – Accepted: 11 December 2018 – Published: 11 January 2019

Abstract. This work presents a connection between the density variation within the mesosphere and lower thermosphere (MLT) and changes in the intensity of solar radiation. On a seasonal timescale, these changes take place due to the revolution of the Earth around the Sun. While the Earth, during the northern-hemispheric (NH) winter, is closer to the Sun, the upper mesosphere expands due to an increased radiation intensity, which results in changes in density at these heights. These density variations, i.e., a vertical redistribution of atmospheric mass, have an effect on the rotation rate of Earth's upper atmosphere owing to angular momentum conservation. In order to test this effect, we applied a theoretical model, which shows a decrease in the atmospheric rotation speed of about $\sim 4 \text{ m s}^{-1}$ at a latitude of 45° in the case of a density change of 1 % between 70 and 100 km. To support this statement, we compare the wind variability obtained from meteor radar (MR) and Microwave Limb Sounder (MLS) satellite observations with fluctuations in the length of a day (LOD). Changes in the LOD on timescales of a year and less are primarily driven by tropospheric large-scale geophysical processes and their impact on the Earth's rotation. A global increase in lower-atmospheric eastward-directed winds leads, due to friction with the Earth's surface, to an acceleration of the Earth's rotation by up to a few milliseconds per rotation. The LOD shows an increase during northern winter and decreases during summer, which corresponds to changes in the MLT density due to the Earth–Sun movement. Within the MLT the mean zonal wind shows similar fluctuations to the LOD on annual scales as well as longer time series, which are connected to the seasonal wind regime as well as

to density changes excited by variations in the solar radiation. A direct correlation between the local measured winds and the LOD on shorter timescales cannot clearly be identified, due to stronger influences of other natural oscillations on the wind. Further, we show that, even after removing the seasonal and 11-year solar cycle variations, the mean zonal wind and the LOD are connected by analyzing long-term tendencies for the years 2005–2016.

1 Introduction

According to the first Kepler law, the Earth travels in a good approximation on an elliptical trajectory around the Sun. Within a year the distance between both celestial bodies changes. During the northern-hemispheric (NH) winter the range is approximately 3.29 % shorter than in the NH summer. Due to the inverse square law, where the intensity I of the radiation is inversely proportional to the Earth–Sun distance squared, this shorter distance between the Sun and the Earth during boreal winter leads to an increased heating of the mesosphere and lower thermosphere (MLT) resulting in an expansion of the MLT and thermosphere, compared to the annual mean. Another effect on the expansion–shrinking of the MLT is given by the variability of solar radiation due to the 11-year solar cycle effect. Figure 1 shows a scheme of the Earth–Sun constellation and the resulting effects, which will be explained in the following. Previous studies such as Walterscheid (1989), Marsh et al. (2007), Emmert (2015), and Lee et al. (2018) showed that solar cycle variations af-

fect the atmospheric density, temperature, chemical composition, and winds over the whole atmosphere, but in particular in the MTI (mesosphere–thermosphere–ionosphere) system. A model simulation by Marsh et al. (2007) showed responses to changes in the 11-year solar cycle for the whole atmosphere. For example, they showed that due to differences in the solar radiation between solar maximum and solar minimum temperature changes by over 100 K occur in the lower thermosphere. Further, they showed the occurrence of tropospheric wind and temperature changes due to changes in solar radiation. But they also mention that changes in the climatology due to solar radiation are too complex to be explained by simplified methods. Stober et al. (2014) showed that a solar cycle effect between 2002 and 2013 led to changes in the neutral density within the MLT region by up to 2.5%. Furthermore, satellite measurements showed on global scales a neutral density decrease by up to ~30% between solar maximum and solar minimum at about 400 km (Emmert et al., 2010). For the 2009–2010 winter season, Stober et al. (2012) showed a connection between the neutral density and the expansion–shrinking of the atmosphere by using meteor radar (MR) winds, lidar, and Microwave Limb Sounder (MLS) satellite temperature measurements. Further, they showed a strong anti-correlation of neutral air density and prevailing zonal winds. This indicates that an increase/decrease in the neutral density occurs almost simultaneously with a decrease/increase in zonal wind speed, respectively.

Changes in the thickness of the atmosphere, resulting from differences in the distance between the Earth and Sun as well as from solar cycle effects, go along with changes in the Earth's rotation speed. Based on the conservation of angular momentum L , the angular velocity ω for an altitude-defined atmospheric layer a , with the thickness $a_o - a_i$, can be estimated by

$$L = J\omega = \frac{2}{5} m \frac{a_o^5 - a_i^5}{a_o^3 - a_i^3} \omega, \quad (1)$$

where J is the moment of inertia for a spherical shell, which rotates about an axis through the center; a_i and a_o are the inner and outer radius of the spherical shell; and m is the atmospheric mass. On this occasion the atmospheric mass is calculated according to Trenberth and Guillemot (1994) by

$$m = \int_{r_0}^{\infty} \int_0^{2\pi} \int_{-\pi/2}^{\pi/2} \rho r^2 \cos \phi \, d\phi \, d\lambda \, dr, \quad (2)$$

where $\rho = \rho(\lambda, \phi, r)$ is the density of air at longitude λ and latitude ϕ , and r is the distance from the Earth's center, while $r = r_0$ at the surface of the Earth. In a good approximation the Earth's surface can be described as an ellipsoid $r_0^2 = a^2(1 - 2\alpha \sin^2 \phi)$, where a is the equatorial radius, $\alpha = (a^2 - b^2)/2a^2$ is related to the flattening, and b is

the polar radius. With respect to the height above the surface z , this results in $r^2 = (a + z)^2(1 - 2\alpha \sin^2 \phi)$ and $dr = (1 - 2\alpha \sin^2 \phi)^{1/2} dz$. Further, under the assumption that $\rho = \rho_1(r)\rho_2(\lambda, \phi)$, the atmospheric mass can be derived by

$$m = \int_0^{2\pi} \int_{-\pi/2}^{\pi/2} \left[\int_0^{\infty} \rho_1(z)(a+z)^2 dz \right] \rho_2(\lambda, \phi) (1 - 2\alpha \sin^2 \phi)^{3/2} \cos \phi \, d\phi \, d\lambda. \quad (3)$$

The integral with respect to z and the relation to the measurements of the surface pressure p_s can be estimated by solving

$$p_s = \int_0^{\infty} \rho_1(z)g(z)dr, \quad (4)$$

where g is the acceleration due to gravity. Considering that g is a function of height and latitude, the total atmospheric mass can be written in numerical terms as $m = 5.22371 \times 10^{15} \bar{p}_s$, where m is given in kilograms and \bar{p}_s is given in hectopascal, for standard gravity at 45° latitude. More detailed information about the estimation of the total mass of the atmosphere can be found in Trenberth and Guillemot (1994). According to Trenberth and Smith (2004) the total mean mass of the atmosphere is 5.148×10^{18} kg and varies slightly on annual scales mainly due to the amount of available water vapor.

A method to measure variations in the rotation speed of the solid Earth is estimating the time the Earth needs for a full rotation. In the following, we define the crust, mantle, and core of the Earth as solid Earth. To estimate the percentage of the atmospheric rotation velocity from the solid Earth rotation velocity, their rotation rate and their variations are necessary. The time the Earth needs for a full rotation is not constant. The rate of rotation and the orientation of the Earth's axis varies in time and space. Perturbations in the Earth's rotation rate are caused either by external forces, such as the influence of celestial bodies, or by internal torques, which are large-scale geophysical processes (Brzezinski et al., 2001). These internal torques are a combination of relative movements and mass reallocation of Earth's core, mantle, crust, oceans tides, and the atmosphere. Geographical differences in wind pattern and oceans cause shifts in the air and in the water masses. Earthquakes displacing the Earth's mantle might also influence the Earth's rotation on longer timescales (Carter and Robertson, 1986).

On timescales less than a year the dominant geophysical process to influence the duration of the Earth's rotation is the atmosphere (Volland, 1988). Every large-scale momentum exchange in the Earth's atmosphere on the Earth's surface increases or decreases the Earth's surface rotation, due to the law of conservation of total angular momentum within its system. The total angular momentum of the Earth's atmo-

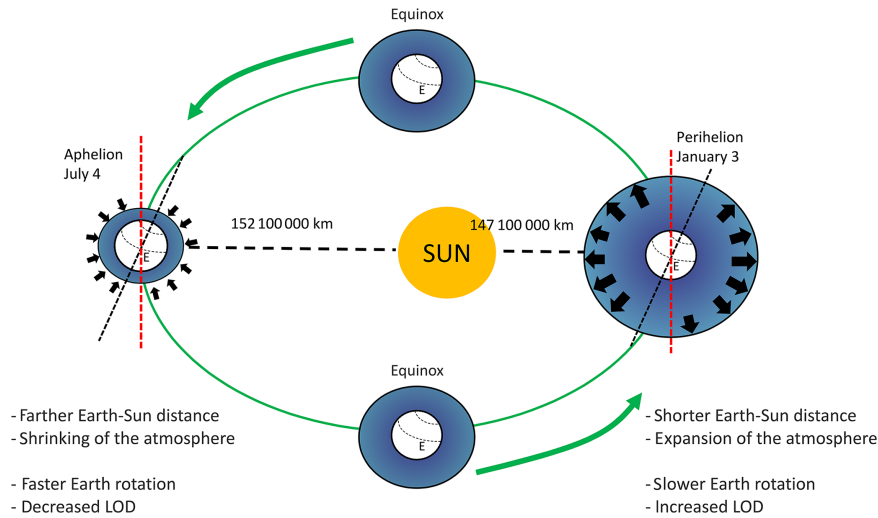


Figure 1. Schema of Earth and Sun correlation and the resulting effects on the thickness of the atmosphere and the Earth’s rotation velocity.

sphere M can be approximately written as

$$M = \int_v \rho_{\text{apc}} L_{\text{apc}} dV = \int_v \rho_{\text{apc}} r \times (u_{\text{rel}} + \omega \times r) dV, \quad (5)$$

where L_{apc} is the angular momentum of an air parcel of unit mass, ρ_{apc} the density of the air parcel, u_{rel} the relative velocity, and $\omega \times r$ the velocity due to the rotation of the Earth (Madden and Speth, 1995).

The total angular momentum and the velocities can be split into two parts. The mass part M_ω represents the value the angular momentum would take if the atmosphere were vertically and horizontally stationary relative to the ground, and the relative part M_r describes the part of the atmosphere angular momentum that is due to the motion of the atmosphere relative to the Earth’s rotation. Following Madden and Speth (1995), Egger et al. (2007), and Driscoll (2010) these parts of angular momentum can be written as

$$M = M_\omega + M_r = \frac{r^4 \omega}{g} \int_0^{2\pi} \int_{-\pi/2}^{\pi/2} p_{\text{sfc}} \cos^3 \theta d\theta d\lambda + \frac{r^3}{g} \int_0^{1000} \int_0^{2\pi} \int_{-\pi/2}^{\pi/2} u_{\text{rel}} \cos^2 \theta d\theta d\lambda dp. \quad (6)$$

Thus, changes in the atmospheric angular momentum depend on the sum of different torques $dM/dt = T_F + T_M + \text{others}$. Here T_F is the friction torque, T_M is the mountain torque, and others torques include, for example, the gravity wave torque, which is small compared to the other two mentioned. The friction torque is exerted on the Earth’s surface mainly due to frictional forces between the wind and the surface. If eastward-directed surface winds are prevailing on

a global scale, this torque leads to an increase in the rotation rate due to a transfer of angular momentum from the atmosphere to the Earth’s surface. The mountain torque is based on the surface pressure and orography, and it is the torque which is exerted on the Earth’s surface due to a difference in pressure on two sides of a mountain. Both torques vary according to their global location and reach values in the range of 10^{19} Nm (Egger et al., 2007; Driscoll, 2010; de Viron and Dickey, 2014). The dominant exchange of the angular momentum between the atmosphere and Earth takes place in the atmospheric boundary layer, which, depending on the orography and latitude, has a typical thickness of about 1 km at midlatitudes (Volland, 1988).

Already in the 1960s and 1970s scientists showed that fluctuations in the orientation of the Earth’s rotation axis, on seasonal timescales, are associated with changes in the east–west tropospheric wind on a global scale and therefore accompanied with a transfer of angular momentum between the Earth’s crust and the atmosphere (Munk and MacDonald, 1961; Lambeck, 1978). Changes in the speed of the Earth’s rotation axis can be seen in fluctuations in the duration around a day. These fluctuations have been measured since the 1960s using the very long baseline interferometry (VLBI) technique. The fluctuation in the day length is the difference between the astronomically determined duration of a full day $2\pi/D$ and the standard 86 400 s, whereby D is the angular velocity (Aoki et al., 1981). Henceforth, we use the acronym LOD for the fluctuations in the length of day. The LOD can be written as

$$\text{LOD}(t) = \frac{2\pi}{D} - 86\,400 \text{ s}. \quad (7)$$

Within the estimation of the LOD the sidereal time gets converted into solar time, by taking into account the Earth’s position, nutation, precession, and motion with respect to

the stars. Detailed information about the transformation from sidereal time into solar time can be found in Aoki et al. (e.g., 1981); Schnell (e.g., 2006).

Carter and Robertson (1986) studied the influence of geophysical processes of the atmosphere on the duration of a day. They showed that, when the globally averaged mean winds from east to west increase, the rotation rate of the Earth decreases and the day gets longer. Rosen and Salstein (1991) showed that the effect of the wind on the LOD decreases with heights, by showing that winds in the atmospheric layer between 1000 and 10 hPa contribute 0.5 ms, winds from 10 to 1 hPa contribute 0.03 ms, and winds above 1 hPa contribute less than 4 μ s to the interannual LOD budget. The impact of large-scale geophysical processes like El Niño (e.g., Dickey et al., 1994) and the stratospheric quasi-biennial oscillation (QBO) can also be seen in the LOD (e.g., Volland, 1988; Eubanks et al., 1988).

On short timescales a change in the Earth rotation can lead to an uneven heating of the Earth's surface, which results in temperature differences between the surface and the atmosphere above. This can further cause convection currents, which leads to pressure differences in the atmosphere and results in a different wind formation, which can influence the day length. The influence of the solar radiation is stronger for higher altitudes and also for longer time series. An increase in the solar radiation, which can be caused due to a slowing of the Earth's rotation, leads to an expansion of the higher atmosphere, which further results, due to the conversion of angular momentum, in a slower rotation of the atmosphere. What further needs to be considered is, for example, the influence of volcanic eruptions, which influence the Earth's rotation as well as the atmospheric chemistry and temperature (e.g., She et al., 2015). Changes in these parameters can further lead to changes in the neutral density.

Within this study, we focus on heights between 60 and 100 km. These heights are sensitive enough to density changes due to the changes in the intensity of solar radiation. After we describe the data we used in this study in Sect. 2, we show results and discuss the theoretical change in the rotation speed due to an expanding–shrinking atmosphere in Sect. 3. We will show that due to the expansion–shrinking effect, even under the assumption of equal density distribution between the Northern and Southern Hemisphere (SH), differences in the prevailing wind occur. Furthermore, we will show a connection between the LOD and the prevailing wind by showing correlations in the MLT region by using MR and MLS data for one polar and two midlatitude locations. We use the LOD data to show how deep the influence of solar radiation penetrates into the atmosphere. The conclusions are found in Sect. 4.

2 Data

The wind data we use in this study are derived from MR and MLS satellite measurements. The MRs are located at the northern high-latitude station Andenes (32.5 MHz; 69.3° N, 16.0° E; Norway), the midlatitude stations Juliusruh (32.5 MHz; 54.6° N, 13.4° E; Germany) and Collm (36.2 MHz; 51.3° N, 13.0° E; Germany) on the Northern Hemisphere, and the southern high-latitude station Davis (33.2 MHz, 68.6° S, 78.0° E, Antarctic). The radars cover an altitude range between 75 and 110 km and the obtained winds have an hourly temporal resolution and a vertical altitude resolution of 2 km in the applied analysis. At 90 km altitude, the observed volume of each radar has a diameter of approximately \sim 400 km, and the mean wind above each station is a weighted average over this volume. In the case of the Andenes, Davis, and Collm, MR data are available between 2005 and 2016 and for Juliusruh since 2008. We focus on an altitude range between 78 and 100 km where we obtain continuous measurements. The statistical uncertainties of winds are obtained from a fitting procedure by taking into account the number of detected meteors per altitude and time bin, as well as a full nonlinear error propagation of the radial wind errors. Therefore the resulting uncertainties for the hourly winds vary in a range between 2 and 6 m s^{-1} with larger errors at the upper and lower part of the meteor layer. More information about the all-sky meteor radars and the wind estimation method used can be found in Hocking et al. (2001), Holdsworth et al. (2004), and Stober et al. (2017). For this research, we focus primarily on the zonal wind component, because a connection between winds and changes in day length will be mainly seen in the main rotation direction of the Earth.

In addition to local radar observations, we use satellite data from the Microwave Limb Sounder to extend the vertical coverage. MLS onboard the Aura satellite (Waters et al., 2006; Livesey et al., 2015) has a global coverage from 82° N to 82° S and an useful height range from approximately 11 to 90 km (261 to 0.001 hPa). The vertical resolution varies between \sim 4 km in the stratosphere and \sim 14 km at the mesopause (Livesey et al., 2007). The geometric heights are approximately estimated from pressure levels as described in Matthias et al. (2013): $h = -7 \cdot \ln(p/1000)$, where h is the altitude in km and p the pressure in hPa. Furthermore, we are aware about a difference between the geometric and geopotential heights, which increase especially above 80 km. Therefore, we focus in this work on the height range between 60 and 80 km (if not otherwise specified) to investigate a connection between the LOD and the density depending on zonal wind within these heights. Daily quasi-geostrophic winds for the years between 2005 and 2016 are derived from MLS geopotential height observations. For this study we use three different horizontal grids which are located around Andenes (70° N and 0–20° E) and around Juliusruh and Collm (50–60° N, 0–20° E), which are further referred to as north-

ern high- and midlatitude stations, respectively. For the SH we use a horizontal grid around Davis (70° S, 60–80° E).

Further we use in this study combined data from the international Earth Rotation and Reference System Service (IERS, 2017). The use of interferometry between several stations, which observe radio sources, leads to fundamental geodetic information such as changes in the Earth's spinning or in the Earth orientation (Rothacher, 2002; Altamimi et al., 2007; Boeckmann, 2010). Based on this information the mean rotation rate and the astronomical duration of the day were computed according to Eq. (6) (Aoki et al., 1981). The IERS provides uncertainties for the day length measurements, which most of the time vary by $\sim 5\%$. More information about the data provided by IERS and their algorithm to estimate the duration of a day can be found in Bizouard et al. (2017).

3 Results and discussion

3.1 LOD and neutral air density at the MLT

Figure 2 shows composites of zonal winds from MR measurements at Andenes, Juliusruh, Collm, and Davis. These data are estimated by using a mean wind adaptive spectral filter (Stober et al., 2017). It uses a 1-day sliding window, which mainly removes the impact of short-term variations, such as atmospheric tides and gravity waves. All three NH stations show almost similar wind patterns, with typical mesospheric eastward-directed winds during the winter, with mean values of up to 10 m s^{-1} , and a wind reversal during spring. The spring wind reversal occurs earlier at midlatitudes than at polar latitudes. During the summer considerable vertical wind shear is present with westward-directed winds below 90 km for Andenes, below 88 km for Juliusruh, and below 85 km for Collm. Above these heights a strong eastward jet occurs. The westward and the eastward jets reach wind values of up to 40 m s^{-1} at all three locations. These annual wind climatologies are consistent with previous studies, e.g., Manson et al. (2004), Hoffmann et al. (2010), and Jacobi (2012). Compared to Andenes a nearly opposite wind pattern can be seen for Davis. A dominant eastward-directed wind occurs between March and September for the complete observation range. Between September and March a vertical wind shear occurs, which reaches heights above 100 km around October. Compared to the NH stations the summer vertical wind shear remains mainly below 90 km.

Besides the radar data, we additionally use MLS data within this study to extend the vertical coverage down to 60 km. In Fig. 3 the zonal wind is shown for the high-latitude location of Andenes, for middle latitudes at Collm, and for the southern latitude location Davis. The altitude ranges between ~ 60 and ~ 90 km geopotential height. A comparison of the MLS composite winds with MR composite winds results in a qualitatively good agreement for the seasonal

amplitudes and phases. Both NH locations show eastward-directed winds between September and April for nearly all altitudes, with values of up to 40 m s^{-1} for the high-latitude area and up to 60 m s^{-1} for the midlatitudes. During summer westward-directed wind dominates below 95 km and reaches values of up to 30 m s^{-1} for the high latitudes. For the middle latitude, below 90 km, the wind reaches values of up to 50 m s^{-1} . A similar pattern of an eastward-directed wind occurs in both cases during summer above 90 km geometric height. The SH location also shows a similar wind pattern to the observed MR data. In the following discussion we will focus on the MLS altitude range 60–80 km and use the MR data for the altitudes between 80 and 100 km.

According to previous studies such as Emmert et al. (2004) and Stober et al. (2012), a connection exists between the thickness of an atmospheric layer and the density fluctuation within that layer. Stober et al. (2012) explained the occurrence of this connection by showing variations in the neutral density, based on MLS and MR observations, together with changes in the MLT geometric height. Furthermore they showed a strong anti-correlation between the simultaneous occurrence of the zonal wind and the density change within the mesosphere.

To underline this statement, we show in the following part the connection between the expanding MLT and the atmospheric rotation speed. Figure 4 shows, as an example, the theoretical variation in the atmospheric rotation velocity with height due to a density increase up to 1% between 70 and 100 km. The calculation is done in 2 km height layers and for the latitude of 45°. Different latitudes lead to slightly different values of g , which is used in Eq. (4). The density increase takes place for longer timescales during a solar maximum (e.g., Emmert et al., 2010) and on annual timescales during the winter, when the Earth–Sun distance is smaller. Both cases influence the temperature within this atmospheric layer as well as their expansion compared to the annual mean. Overall the density variation during an 11-year solar cycle is stronger than the variation caused by the changes in the Earth–Sun distance. According to Eqs. (1)–(4), we estimated for three different cases (linear, red; exponential, green; and a Gaussian-shaped, blue, density increase) the resulting theoretical change in the rotation speed within these heights, with the solid Earth rotation speed (black) as background flow. Based on the conserved quantity of the angular momentum within a narrow atmospheric layer (2 km vertical) this sums up, according to each case, to a decrease in the rotation speed by up to $\sim 2\text{--}4\text{ m s}^{-1}$, with the strongest variation within the Gaussian-shaped curve. These results fit to the observations by Stober et al. (2012) and show the dependence of the rotation speed within an atmospheric layer due to changes in the neutral density. However, we are not able to extract a specific wind value only based on wind measurements.

Based on ERA40 data, Trenberth and Smith (2004) showed that the global mean of the surface pressure is nearly constant, and surface pressure anomalies at the Northern and

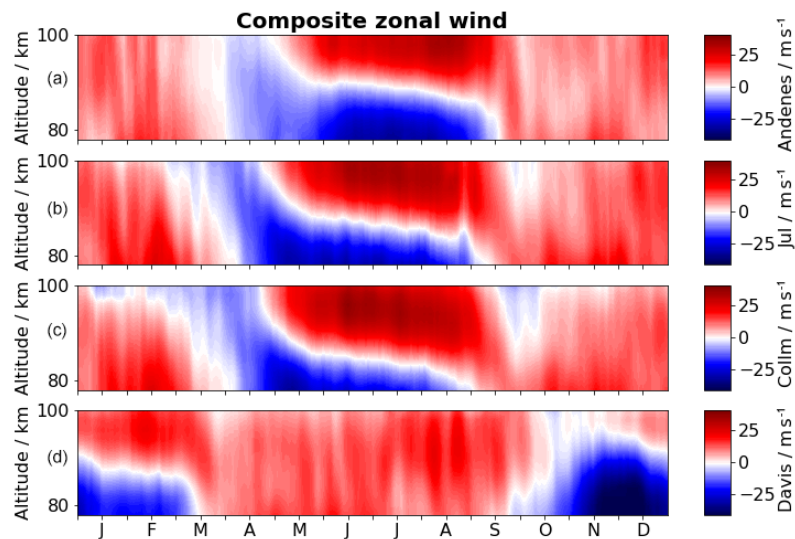


Figure 2. Composites of zonal wind for the Northern Hemisphere stations Andenes (a), Juliusruh (b), and Collm (c). (d) shows the southern-hemispheric station of Davis. The composite for Andenes, Collm, and Davis includes 12 years of meteor radar data and that of Juliusruh includes 9 years. Positive values correspond to eastward-directed winds and negative to westward-directed winds.

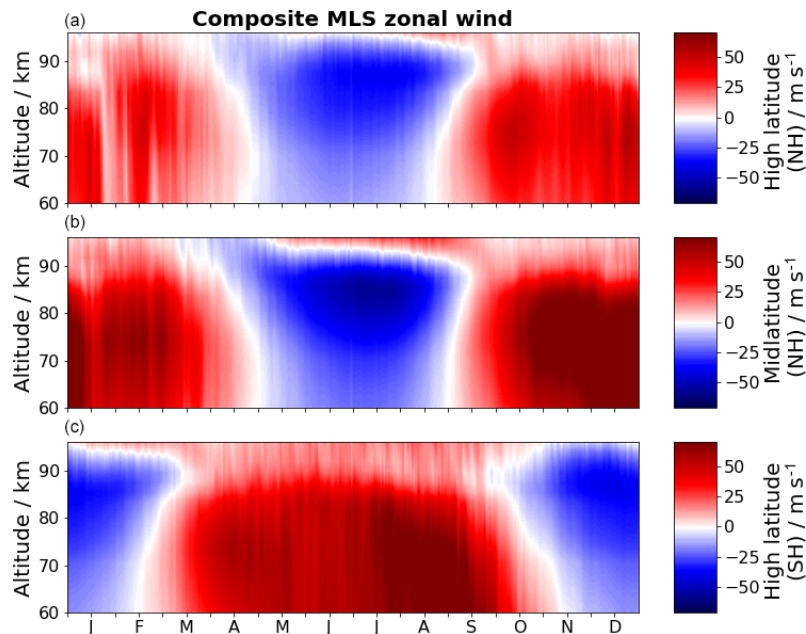


Figure 3. Composite of zonal wind for the high-latitude location (a) and midlatitude location (b). The composite of both figures includes 12 years of wind data derived from MLS geopotential height data. Positive values corresponds to eastward-directed winds and negative to westward-directed winds. The altitude is given in geopotential height.

the Southern Hemisphere are nearly identical, but the fluctuations are opposite in sign. These anomalies are mainly due to the changing amount of available water vapor in the atmosphere. Under the assumption of opposite surface pressure anomalies within both hemispheres and therefore by neglecting other factors such as different gravity wave forcing

between the hemispheres, we assume, on annual scales, similar pressure values within the MLT region. Therefore the prevailing wind within the MLT region should be similar in magnitude between Andenes and Davis, which are located at the same latitude in the Northern and Southern Hemisphere. To underline the influence of the intensity of the solar radi-

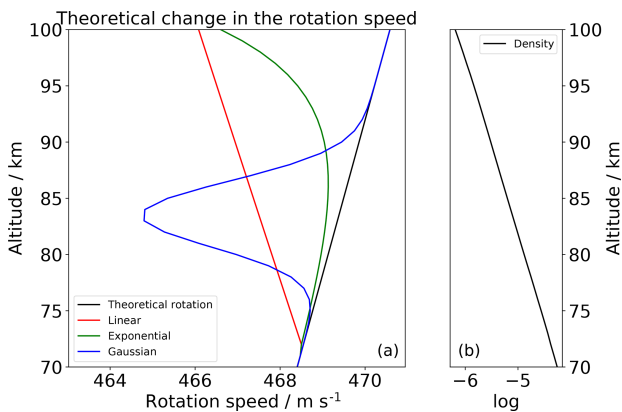


Figure 4. Theoretical change in the rotation speed (left side) for a rigid atmospheric layer. In black we show the theoretical rotation speed of the Earth’s atmosphere and in colors the change due to a density increase of 1 % according the legend. On the right side the density progress is shown for specific altitudes.

ation on the density and also on the amplitude of the zonal wind, we compare the evolution of the seasonal mean wind measurements from the NH station Andenes (69.3° N) and SH station Davis (68.3° S). Figure 5 shows, for both stations, the winter and summer mean wind for the altitudes at 88 and 96 km. The northern winter includes the mean of the months of December, January, and February and the southern winter the months June, July, and August. The northern winter period comes along with the perihelion, which is the point where the Earth comes nearest to the Sun. At the perihelion, the intensity of the solar radiation on the upper atmosphere is stronger during the aphelion. While during the winter season the wind values are higher over Davis for both altitudes, they are higher over Andenes during the summer season, especially at 96 km, with values of up to 10–20 m s⁻¹. Both seasonal wind differences are consistent with the change in the average density within the upper mesosphere, resulting from the different distance between the Earth and Sun and leading to the variation of the averaged zonal wind, as shown in Stober et al. (2012). We have to note that others factors exists, which are more dominant for the wind differences between both locations at these altitudes. Other physical processes also have a strong effect on the hemispheric wind differences, e.g., the topography, chemical composition of the atmosphere (Marsh et al., 2007; Lee et al., 2018), and the occurrence and propagation of gravity waves. These waves are the main drivers of the atmospheric wind circulation and therefore also influence the local wind differences at both hemispheres. Furthermore, gravity waves lead, compared to the annual mean, to a colder summer mesosphere and a warmer winter mesosphere (e.g., Lübken et al., 2014). These temperature differences also fit well to the atmospheric expansion–shrinking. Unfortunately, we are not able to estimate a precise value on how strong the connection is between

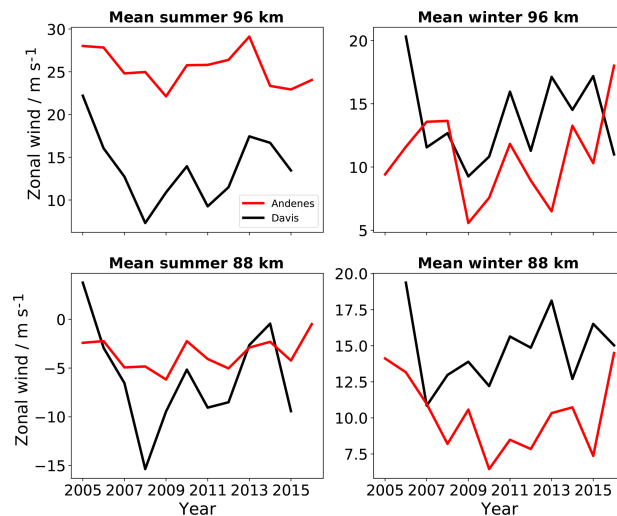


Figure 5. Zonal wind amplitudes for the winter and summer season at 96 and 88 km for Andenes and Davis.

mean zonal wind and the LOD based only on wind measurements. For a more detailed understanding of these phenomena global density observations would be required.

3.2 Correlation of mean winds and LOD

In the following we want to show that the LOD (fluctuations in the length of a day) correlates with the prevailing wind from the four stations. If the Earth’s rotation is constant the LOD should be zero; however, small wobbles of the Earth’s rotation between the days cause tiny fluctuations in the day length. These have to be compensated for by a momentum transfer between the different parts of the Earth including the atmosphere. As the atmosphere is slaved to the Earth crust, because the atmospheric momentum and mass are much smaller than that of the Earth core, the atmosphere has to respond to changes in the rotation velocity. So far we use the LOD explicitly as reference for the changes in the rotation speed, which can be seen in the zonal wind, as well as to verify up to which height the solar-driven density effect is dominant. Therefore, Figs. 6 and 7 show wind values for Andenes, Collm, and Davis at different altitudes and the LOD by using the same filtering method as done for the winds. Two different altitudes in the MLT are considered from the MR winds for all locations: (1) 80 km, where within a year a change between eastward- and westward-directed wind occurs; and (2) 96 km, which is the altitude where the wind, during each hemispheric summer, shows the opposite direction compared to at 80 km (see Fig. 2). Positive wind values correspond to eastward-directed winds and positive LOD values correspond to a longer duration of the day. If not explicitly mentioned, the results of the two midlatitude stations are nearly identical. Therefore we only show the results for the location around Collm.

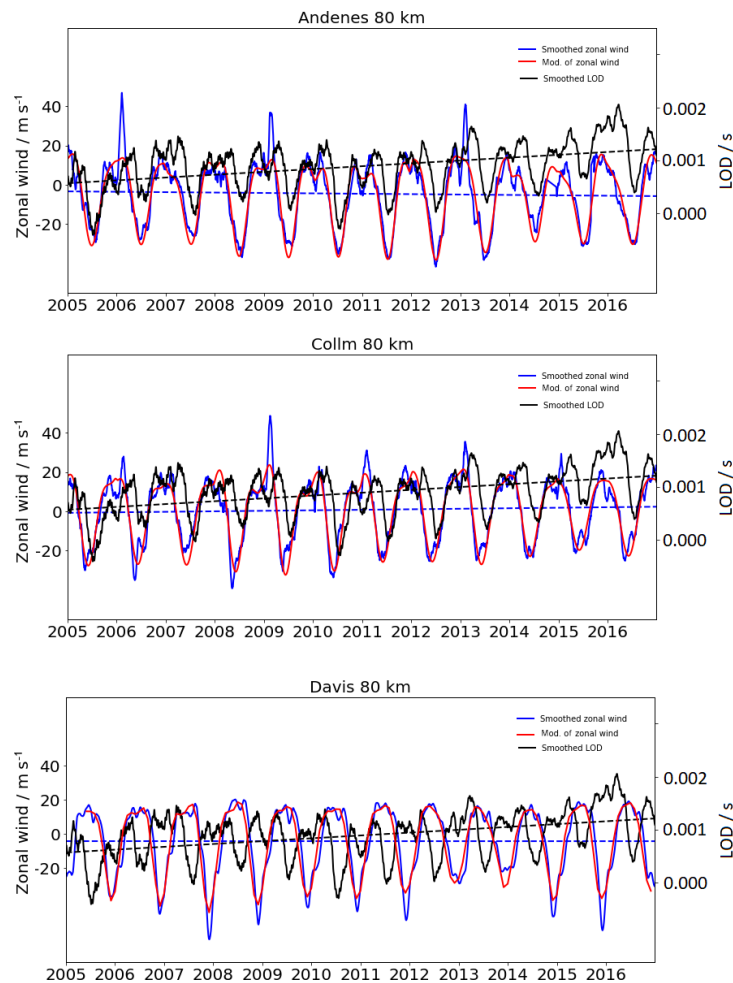


Figure 6. Smoothed zonal wind (blue) values based on meteor radar wind data at 80 km and smoothed LOD (black) values. The modulation of the smoothed zonal wind is displayed in red after removing the impact of the solar cycle. All curves are done by smoothing over several days, without removing the day-to-day variations, to show the seasonal pattern of the parameters. The dashed lines correspond to the tendency of the wind and LOD based on linear regression.

At 80 km (Fig. 6) the oscillation pattern of the smoothed zonal wind (blue) and the smoothed LOD (black) are similar for Andenes. According to previous studies the LOD consists of superpositions of several periods, such as 0.5 years, 1 year (see also Vondrák and Burša, 1977), 2–3 years (Bufet, 1996), 5.9 years (Abraca del Rio et al., 1999), and others (e.g., Munk and MacDonald, 1961; Holme and de Viron, 2013). According to Abarca del Rio et al. (2003) an accurate estimation of the impact of the solar radiation is quite complicated, due to the fact that internal oscillations in the climate system show variations with the same frequency as the 11-year solar cycle. Further, Gray et al. (2010) support this statement and mention that the problem is further complicated due to the small influence of the solar forcing on the climate. Nevertheless, Chaponov and Gambis (2008) showed that, based on a decomposition of the LOD, the solar activity

(10.47 years) is included. Also the zonal wind includes a superposition of several periods such as the solar cycle, diurnal and semidiurnal tides, and more (e.g., Emmert et al., 2010; Hoffmann et al., 2010). Therefore, we additionally show with the red line a smoothed zonal wind after removing variations due to the 11-year solar cycle. The influence of the solar cycle on the daily zonal wind is relatively small; therefore the smoothness of the red line is enhanced for better visualization. Changes in the LOD are sluggish compared to variations in the wind, due to the amount of momentum which is needed to influence the Earth's rotation speed. According to Dickey et al. (1994), a direct effect between the stratospheric and tropospheric zonal wind and the day length exists on annual timescales due to long-term geophysical effects, such as QBO and El Niño. They found that the stratosphere cannot be neglected in the Earth's angular momentum. Around 20 % of

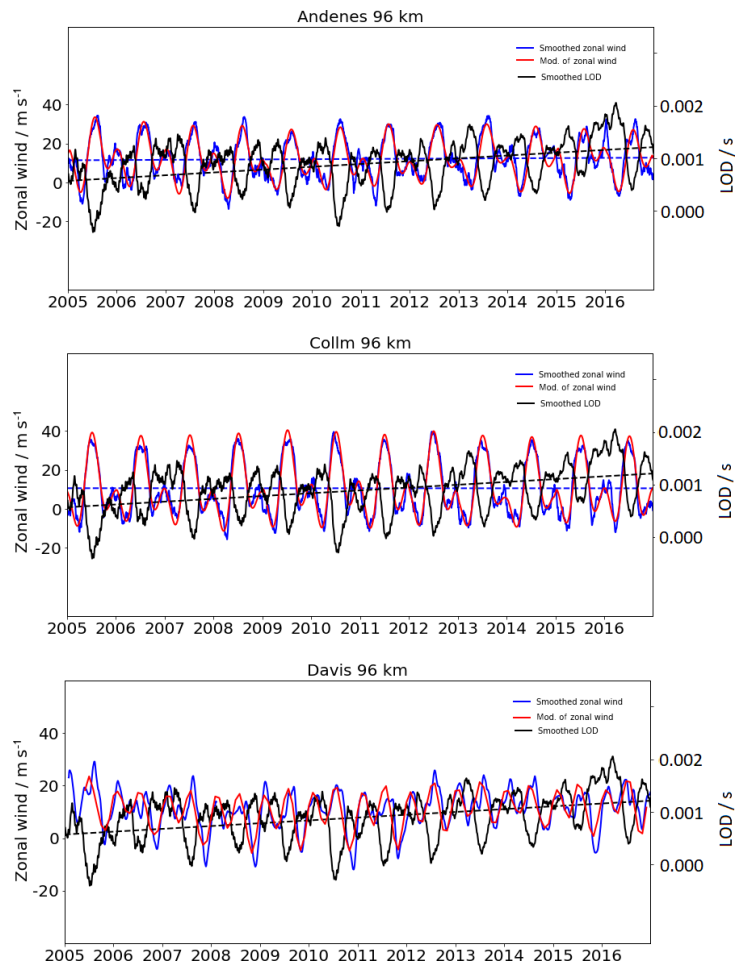


Figure 7. Same as Fig. 6, but for 96 km.

the LOD relative to the atmosphere below 100 hPa belongs to the impact of the stratosphere. Furthermore, they mentioned a small lag (10–20 days) between the LOD and variations in the angular momentum, but the lag does not appear to be statistically significant. Therefore only comparisons on seasonal and longer timescales are useful to consider. All parameters which are displayed in Fig. 6 show a seasonal pattern. First we describe the results for the NH stations. For the NH the zonal wind and the LOD show decreasing values during summer and increasing values during winter. Beside the striking seasonality, short time fluctuations within a year are observable during the winter in the zonal wind for some years. During the winter of 2010 and 2011, and on even shorter timescales such as a few months during the winter 2006, 2014, and 2015, decreases in the LOD together with decreases in the zonal wind are visible. The LOD varies between -1 and 4 ms. The LOD oscillation shows seasonal variations of a fluctuation with shorter day lengths during NH summer and longer day lengths during winter, which fits to

the density increase and decrease in the MLT as described above. For the midlatitude station the oscillation patterns in the LOD and the wind are qualitatively similar, but shifted in time. The wind peaks occur earlier in the year than the LOD peaks, which goes along with the earlier wind transition at midlatitudes that can be seen in Fig. 2. For Davis a time shift of approximately 6 months occurs between the zonal wind and the LOD, due to the opposite seasonal wind pattern.

In the summer wind transition altitude, a time shift occurs between both parameters. The altitude of the wind transition in these cases is defined as the height between the above-located eastward and the below-located westward wind during summer. At these heights the wind and the LOD are almost uncorrelated. Above the summer wind transition altitude the oscillation patterns between the LOD and the winds are quite opposite to those for 80 km altitude, with a 180° shift between both parameters, which can be seen in Fig. 7. The phase shift, which is pronounced during the summer, obviously results from the opposite wind regime compared to

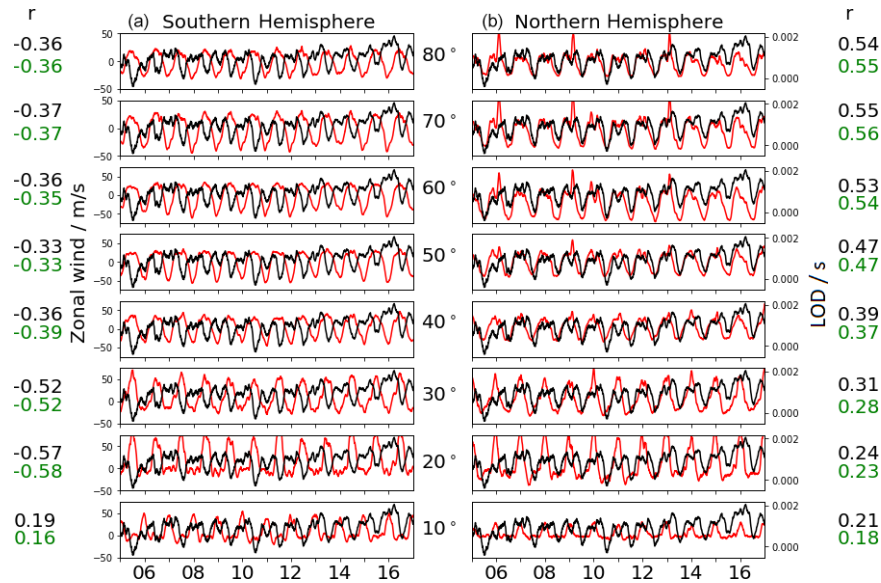


Figure 8. Zonal MLS wind (red) and LOD (black) at ~ 80 km geometric height for $0\text{--}20^\circ$ E. The left part shows the values for the Southern Hemisphere and the right for the Northern Hemisphere for every 10° latitude. The black correlation coefficients (r) are estimated for the mean between 0 and 20° E, and the green coefficients correspond to the global average over all longitudes.

Table 1. Correlation coefficients between the zonal wind and the LOD. Positive values corresponds to the occurrence of an eastward-directed mean zonal wind together with a positive fluctuation in the LOD.

Altitude (km)	80	82	84	86	88	90	92	94	96	98
Andenes	0.57	0.56	0.52	0.42	0.21	-0.13	-0.45	-0.61	-0.67	-0.69
Juliusruh	0.43	0.36	0.23	0.04	-0.23	-0.48	-0.62	-0.67	-0.68	-0.68
Collm	0.3	0.19	-0.01	-0.3	-0.54	-0.65	-0.68	-0.68	-0.66	-0.64
Davis	-0.37	-0.37	-0.38	-0.39	-0.41	-0.42	-0.41	-0.38	-0.35	-0.32

the 80 km altitude. Nevertheless, above the transition height, changes in the density, due to the intensity of the solar radiation, are more pronounced than at lower heights. Therefore the existing seasonal wind pattern fits well to the atmospheric density increase and decrease at these layers.

Additionally, we show in Table 1 correlation coefficients for the four locations for the altitudes between 80 and 98 km. Positive correlation values correspond to the occurrence of an eastward-directed wind together with an increased LOD. The values of the NH follow a similar pattern, with positive coefficients below the vertical transition height and negative ones above. Davis shows a different pattern, with overall negative correlation coefficients. This is owing to the opposite zonal wind pattern compared to the NH. Theoretically, a time shift of ~ 6 months would lead to a similar correlation pattern to that in the NH.

Figure 8 shows the mean zonal wind at ~ 80 km geometric height, based on MLS data, and the LOD. These mean zonal winds include wind values within the longitude grid between 0 and 20° E, which is comparable to the NH stations. The figure is divided in 10° latitude steps centered at lati-

tudes from 80 to 10° S/N. Each latitude grid includes values for $\pm 6^\circ$. For the MLS observations the comparisons between the wind and the LOD are similar to the 80 km meteor results at the respective latitudes. Furthermore, the occurrence of a time shift of 6 months between both polar hemispheres can be seen. A 180° phase shift would lead to the wind–LOD pattern of the opposite hemisphere. Furthermore, the strongest correlation between both parameters can be seen at northern polar latitudes. Due to an increase in the difference between the geometric and geopotential heights, we do not show comparisons for higher altitudes. We added correlation coefficients (black) between the mean zonal wind and the LOD for each latitude. A correlation increase towards the northern high latitudes is visible. The same would be seen if a 180° phase shift is added to the time series. Additionally, we present global correlations (green) by averaging mean zonal wind data over all longitudes, whereby possible stationary planetary waves are filtered. The global correlation coefficients are nearly similar to the values for previous average winds between 0 and 20° E. The shape of the curves between

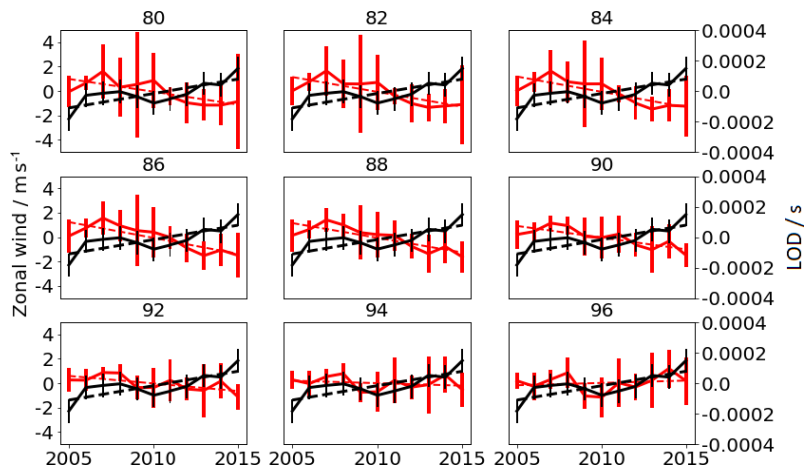


Figure 9. Annual mean values for the LOD (black) and the zonal wind (red), for the station Collm, after removing seasonal variations and the solar cycle for the altitudes between 80 and 100 km. The error bars correspond to the standard deviation. The dashed lines represents the tendency.

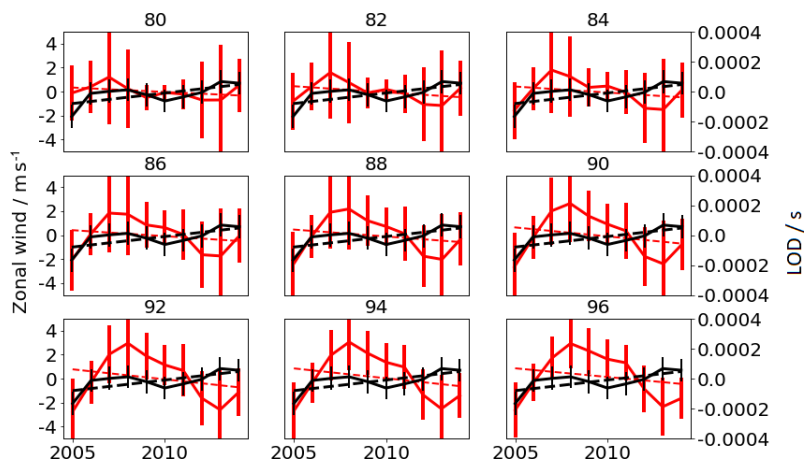


Figure 10. Same as Fig. 9, but for Davis.

the global average winds is also nearly equal; therefore we did not add them in the figure.

In Figs. 9 and 10, long-term changes in annual LOD (black) and annual mean zonal winds (red) are shown for Collm and for Davis. At this point, we have to mention that the tendency over a long time series is not linear in time. Parameters which influence the tendency of the wind and the LOD also vary over time. Such changes are often approximated by a piecewise linear trend model (e.g., Tomé and Miranda, 2004; Merzlyakov et al., 2009; Jacobi et al., 2011), where different linear fit tendencies are estimated for different time periods. Nevertheless, due to the length of the available data series we decided not to use a piecewise linear trend model. The wind values exclude seasonal and solar cycle variations and the LOD excludes the seasonal variations. As an example for the location of Collm (Fig. 9), the

altitudes between 80 and 96 km are displayed. The error bars correspond to the annual variance for each height and the dotted lines show the long-term tendency for each parameter. Figure 9 shows that a long-term increase in the LOD occurs together with a long-term decrease in the zonal wind. Above 94 km the tendency reverses into a slightly positive wind. This reversal can be explained by the stronger influence due to gravity wave filtering, which has to be considered and cannot be excluded by filtering the data. The tendencies of an increased value for the LOD and a decreased value for the mean zonal wind can be seen for all midlatitude locations and also for Davis (see Fig. 10). Andenes shows for all altitudes an increased tendency in the zonal wind (not shown). The results indicate that the connection between the LOD and the wind is more pronounced at lower latitudes and is simply explainable by the rotation velocity, which is

higher at the middle latitude stations than at the polar latitudes like at Andenes and Davis. The results of an increase in the LOD and a decrease in zonal wind agree with the relation between fluctuations in the neutral density and the zonal wind, as shown in Stober et al. (2012).

4 Conclusions

Within this work we show that the mesospheric winds are affected by an expansion–shrinking of the upper atmosphere that takes place due to changes in the intensity of the solar radiation, which affects the density within the atmosphere. A reason for this, besides the solar cycle effect, is the annual movement of the Earth around the Sun, which leads to a shorter distance between both celestial bodies during the NH winter and a longer distance during summer. This leads to a shrinking/expansion of the atmosphere during the NH summer/winter. This shrinking effect mainly takes place in the upper atmosphere, where the amount of mass is small enough to be sensitive enough to changes to the intensity of solar radiation, as well as temperature changes. According to Stober et al. (2012) an increase in the neutral density together with a decrease in the zonal wind in the MLT region occurs. Based on these findings we showed that a theoretical density increase of 1 % between 70 and 100 km leads to a decrease in the atmospheric rotation speed, within a defined layer, of up to 4 m s^{-1} . The influence of the Earth–Sun distance on the wind speed was further investigated using winds from four stations in total, whereby two stations are located at similar high latitudes for the Northern and Southern Hemisphere. The other two meteor radar systems are located at the northern midlatitudes. Based on summer and winter mean wind, we found that during the perihelion, where the MLT expands, a decrease in the zonal wind speed for the respective location occurs together with an increase in the LOD. During the opposite aphelion, an increase in the zonal wind occurs beside a decrease in the day length.

Further, we showed that even after removing the seasonal and the 11-year solar cycle variations the zonal wind and the LOD (fluctuations in the length of a day) are connected. We showed on the basis of annual timescales that an increase in the LOD occurs together with a stronger pronounced westward-directed wind for the middle latitude locations. This effect is weaker at the polar station and is, on the one hand, due to a smaller radius, which affects the rotation speed of the atmospheric layer. On the other hand, there are further natural factors, such as the gravity wave drag, that strongly influence these tendencies. Further, we were only able to investigate the connection between these parameters on timescales which are at least 1 year. On shorter timescales a connection between the LOD and the winds cannot be figured out; the LOD consists of oscillations with at least a 6-month period and with the currently available data we are not able to fully resolve the superpositions of both param-

eters. Future work remains necessary to fully understand these effects when global density data measurements are available. Additionally, in future work the estimation of a time lag between the LOD and the winds needs to be considered.

We want to mention that based on our findings a connection between the zonal wind and the LOD exists, which we explain by the variation of the available atmospheric density. Furthermore, we only compare global LOD data with local measurements, and within the MLT stronger geophysical effects which drive the wind regime at these altitudes exist. Within this work we only want to point out this effect, and for closer investigations we need global longtime density data.

Data availability. The Andenes and Juliusruh radar data are available upon request from Gunter Stober (stober@iap-kborn.de). The Collm radar data are available upon request from Christoph Jacobi (jacobi@rz.uni-leipzig.de). The Davis radar data are available upon request from Damian Murphy (damian.murphy@aad.gov.au). The Microwave Limb Sounder data are available at <https://mls.jpl.nasa.gov/> (Matthias, 2018).

Author contributions. SW wrote the manuscript with input from all authors. Furthermore, all co-authors contributed to the data interpretation. GS provided the high-resolution meteor wind data analysis for all stations and ensured the operation of the Andenes and Juliusruh meteor radar. VM provided the wind analysis used for the Microwave Limb Sounder data. CJ ensured the operation of the Collm meteor radar and DM the Davis meteor radar.

Competing interests. The authors declare that they have no conflict of interest. Christoph Jacobi is one of the Editors in Chief of *Annales Geophysicae*.

Acknowledgements. This work was supported by the WATILA project (SAW-2015-IAP-1 383). The operation of the Davis meteor radar was supported through Australian Antarctic Science projects 2668 and 4025. We thank IERS for providing the LOD data used, which can be found under <https://datacenter.iers.org> (last access: 4 April 2017). Furthermore we acknowledge the IAP technicians for the technical support and Jorge L. Chau for discussions at an early stage of the work.

The publication of this article was funded by the Open Access Fund of the Leibniz Association.

Edited by: Andrew J. Kavanagh

Reviewed by: Chris Meek and one anonymous referee

References

Abarca del Rio, R., Gambis, D., Salstein, D., Nelson, P., and Dai, A.: Solar activity and earth rotation variability, *J. Geodyn.*,

- 36, 423–443, [https://doi.org/10.1016/S0264-3707\(03\)00060-7](https://doi.org/10.1016/S0264-3707(03)00060-7), 2003.
- Abraca del Rio, R., Gambis, D., and Salstein, D.: Interannual signal in length of day and atmospheric angular momentum, *Ann. Geophys.*, 18, 347–364, <https://doi.org/10.1007/s00585-000-0347-9>, 1999.
- Altamimi, Z., Collilieux, X., Legrand, J., Garayt, B., and Boucher, C.: ITRF2005: A new release of the International Terrestrial Reference Frame based on time series of station positions and Earth Orientation Parameters, *J. Geophys. Res.*, 112, B09401, <https://doi.org/10.1029/2007JB004949>, 2007.
- Aoki, S., Guinot, B., Kaplan, G., Kinoshita, H., McCarthy, D., and Seidelmann, P.: The new Definition of Universal Time, *Astron. Astrophys.*, 105, 359–361, 1981.
- Bizouard, C., Lambert, S., Becker, O., and Richard, J.: Combined solution C04 for Earth Rotation Parameter consistent with International Terrestrial Reference Frame 2014, available at: <https://hpiers.obspm.fr/iers/eop/eopc04/C04.guide.pdf>, last access: 26 July 2017.
- Boeckmann, S.: Robust determination of station positions and Earth orientation parameters by VLBI intra-technique combination, Ph.D. thesis, Friedrich-Wilhelms-University, available at: http://hss.ulb.uni-bonn.de/diss_online (last access: 13 July 2017), 2010.
- Brzezinski, A., Bizouard, C., and Petrov, S.: Influence of the atmosphere on earth rotation: what can be learned from the recent atmospheric angular momentum estimates?, *Surv. Geophys.*, 23, 33–69, <https://doi.org/10.1023/A:1014847319391>, 2001.
- Buffet, B. A.: Gravitational oscillations in the length of day, *Geophys. Res. Lett.*, 23, 2279–2282, 1996.
- Carter, W. E. and Robertson, D. S.: Studying the Earth by Very-Long-Baseline Interferometry, *Sci. Am.*, 255, 46–54, 1986.
- Chapanov, Y. and Gambis, D.: Correlation between the solar activity cycle and the Earth rotation, available at: https://syrtex.obspm.fr/jsr/journees2007/pdf/s4_18_Chapanov.pdf (last access: 2 August 2018), 2008.
- de Viron, O. and Dickey, J. O.: The two types of El Niño and their impacts on the length of day, *Geophys. Res. Lett.*, 41, 3407–3412, <https://doi.org/10.1002/2014GL059948>, 2014.
- Dickey, J. O., Marcus, S. L., Hide, R., Eubanks, T. M., and Boggs, D. H.: Angular momentum exchange among the solid Earth, atmosphere, and oceans: A case study of the 1982–1983 El Niño event, *J. Geophys. Res.*, 99, 23921–23937, 1994.
- Driscoll, S.: The Earth's Atmospheric Angular Momentum budget and its representation in reanalysis observation data and climate models, Ph.D. thesis, University of Reading, 2010.
- Egger, J., Weickmann, K., and Hoinka, K.-P.: Angular momentum in the global atmospheric circulation, *Rev. Geophys.*, 45, RG4007, <https://doi.org/10.1029/2006RG000213>, 2007.
- Emmert, J. T.: Altitude and solar activity dependence of 1967–2005 thermospheric density trends derived from orbital drag, *J. Geophys. Res.-Space*, 120, 2940–2950, <https://doi.org/10.1002/2015JA021047>, 2015.
- Emmert, J. T., Lean, J. L., and Picone, J. M.: Record-low thermospheric density during the 2008 solar minimum, *Geophys. Res. Lett.*, 37, L12102, <https://doi.org/10.1029/2010GL043671>, 2010.
- Emmert, J. T., Picone, J. M., Lean, J. L., and Knowles, S. H.: Global change in the thermosphere: Compelling evidence of a secular decrease in density, *J. Geophys. Res.*, 109, 1–12, <https://doi.org/10.1029/2003JA010176>, 2004.
- Eubanks, T., Steppe, J., and Dickey, J.: The Earth's Rotation and Reference Frame for Geodesy and Geodynamics, chap.: The atmospheric excitation of rapid polar motions, Springer, 1988.
- Gray, L. J., Beer, J., Geller, M., Haigh, J. D., Lockwood, M., Matthes, K., Cubasch, U., Fleitmann, D., Harrison, G., Hood, L., Luterbacher, J., Meehl, G. A., Shindell, D., van Geel, B., and White, W.: Solar influence on climate, *Rev. Geophys.*, 48, 1–53, <https://doi.org/10.1029/2009RG000282>, 2010.
- Hocking, W. K., Fuller, B., and Vandeppeer, B.: Realtime determination of meteor-related parameters utilizing modern digital technology, *J. Atmos. Sol.-Terr. Phys.*, 69, 155–169, [https://doi.org/10.1016/S1364-6826\(00\)00138-3](https://doi.org/10.1016/S1364-6826(00)00138-3), 2001.
- Hoffmann, P., Becker, E., Singer, W., and Placke, M.: Seasonal variation of mesospheric waves at northern middle and high latitudes, *J. Atmos. Sol.-Terr. Phys.*, 72, 1068–1079, <https://doi.org/10.1016/j.jastp.2010.07.002>, 2010.
- Holdsworth, D. A., Tsutsumi, M., Reid, I. M., Nakamura, T., and Tsuda, T.: Interferometric meteor radar phase calibration using meteor echoes, *Radio Sci.*, 39, 1–12, <https://doi.org/10.1029/2003RS003026>, 2004.
- Holme, R. and de Viron, O.: Characterization and implications of intradecadal variations in length of day, *Nature*, 499, 202–204, <https://doi.org/10.1038/nature12282>, 2013.
- IERS: Earth orientation data, https://datacenter.iers.org/data/latestVersion/224_EOP_C04_14.62-NOW.IAU2000A224.txt, last access: 4 April 2017.
- Jacobi, C.: 6 year mean prevailing winds and tides measured by VHF meteor radar over Collm (51.3° N, 13.0° E), *J. Atmos. Sol.-Terr. Phys.*, 78/79, 8–18, <https://doi.org/10.1016/j.jastp.2011.04.010>, 2012.
- Jacobi, C., Hoffmann, P., Liu, R. Q., Merzlyakov, E. G., Portnyagin, Yu. I., Manson, A. H., and Meek, C. E.: Long-term trends, their changes, and interannual variability of Northern Hemisphere midlatitude MLT winds, *J. Atmos. Sol.-Terr. Phys.*, 75/76, 81–91, <https://doi.org/10.1016/j.jastp.2011.03.016>, 2011.
- Lambeck, K.: Progress in geophysical aspects of the rotation of the Earth, in: Ninth Geodesy and Solid Earth and Ocean Physics Research Conference, 1–11, 1978.
- Lee, J. N., Wu, D., L. R. A., and Fontenla, J.: Solar cycle variations in mesospheric carbon monoxide, *J. Atmos. Sol.-Terr. Phys.*, 170, 21–34, <https://doi.org/10.1016/j.jastp.2018.02.001>, 2018.
- Livesey, N. J., Read, W. G., Lambert, A., Cofield, R., E., Cuddy, D., T., Froidevaux, L., Fuller, R., A., Jarnot, R., F., Jiang, J., H., Jiang, Y., B., Knosp, B., W., Kovalenko, L., J., Pickett, H., M., Pumphrey, H., C., Santee, M., L., Schwartz, M., J., Stek, P., C., Wagner, P., A., Waters, J., W., and Wu, D., L.: EOS MLS Version 2.2 Level 2 Data Quality and Description Document., Technical Report Version 2.2 D-33509, Jet Propulsion Lab., California Institute of Technology, Pasadena, California 91198-8099, 2007.
- Livesey, N., Santee, M. L., and Manney, G.: A Match-based approach to the estimation of polar stratospheric ozone loss using Aura Microwave Limb Sounder observations, *Atmos. Chem. Phys.*, 15, 9945–9963, <https://doi.org/10.5194/acp-15-9945-2015>, 2015.
- Lübken, F.-J., Höffner, J., Kaifler, B., and Morris, R., J.: Winter/summer mesopause temperature transition at Davis

- (69° S) in 2011/2012, *Geophys. Res. Lett.*, 41, 5233–5238, <https://doi.org/10.1002/2014GL060777>, 2014.
- Madden, R., A. and Speth, P.: Estimates of atmospheric angular momentum, friction, and mountain torques during 1987–1988, *J. Atmos. Sci.*, 52, 3681–3694, 1995.
- Manson, A. H., Meek, C. E., Hall, C. M., Nozawa, S., Mitchell, N. J., Pancheva, D., Singer, W., and Hoffmann, P.: Mesopause dynamics from the scandinavian triangle of radars within the PSMOS-DATAR Project, *Ann. Geophys.*, 22, 367–386, <https://doi.org/10.5194/angeo-22-367-2004>, 2004.
- Marsh, D., R., Garcia, R., R., Kinnison, D., E., Boville, B., A., Sassi, F., Solomon, S., C., and Matthes, K.: Modeling the whole atmosphere response to solar cycle changes in radiative and geomagnetic forcing, *J. Geophys. Res.*, 112, 1–20, <https://doi.org/10.1029/2006JD008306>, 2007.
- Matthias, V., Hoffmann, P., Manson, A., Meek, C., Stober, G., Brown, P., and Rapp, M.: The impact of planetary waves on the latitudinal displacement of sudden stratospheric warmings, *Ann. Geophys.*, 31, 1397–1415, <https://doi.org/10.5194/angeo-31-1397-2013>, 2013.
- Matthias, V.: MLS/Aura Level 2 Geopotential Height V004, available at: <https://mls.jpl.nasa.gov/>, last access: 2 January 2018.
- Merzlyakov, E., G., Jacobi, C., Portnyagin, Yu., I., and Solovjova, T., V.: Structural changes in trend parameters of the MLT winds based on wind measurements at Obninsk (55° N, 37° E) and Collm (52° N, 15° E), *J. Atmos. Sol.-Terr. Phys.*, 71, 1547–1557, <https://doi.org/10.1016/j.jastp.2009.05.013>, 2009.
- Munk, W. H. and MacDonald, G. J. F.: *The Rotation of the Earth. A Geophysical Discussion*, vol. 98, Cambridge University Press, <https://doi.org/10.1017/S0016756800060726>, 1961.
- Rosen, R. D. and Salstein, D.: Comment on “A Seasonal budget of the Earth’s axial angular momentum” by Naito and Kikuchi, *Geophys. Res. Lett.*, 18, 8033–8041, <https://doi.org/10.1029/91GL02312>, 1991.
- Rothacher, M.: Proceedings of the IERS Workshop on Combination Research and Global Geophysical Fluids, Bavarian Academy of Sciences, Munich, Germany, chap.: Towards a Rigorous Combination of Space Geodetic Techniques, International Earth Rotation and Reference Systems Service (IERS), IERS Technical Note, No. 30, Verlag des Bundesamtes für Kartographie und Geodäsie, ISBN 3-89888-877-0, 18–21, 2002.
- Schnell, D.: Quality aspects of short duration VLBI observations for UT1 determinations, Rheinischen Friedrich-Wilhelms-Universität zu Bonn, available at: <http://hss.ulb.uni-bonn.de/2006/0918/0918.htm> (last access: 22 November 2018), 2006.
- She, C., Krueger, D., A., and Yuan, T.: Long-term midlatitude mesopause region temperature trend deduced from quarter century (1990–2014) NA lidar observations, *Ann. Geophys.*, 33, 363–369, <https://doi.org/10.5194/angeocom-33-363-2015>, 2015.
- Stober, G., Jacobi, C., Matthias, V., Hoffmann, P., and Gerding, M.: Neutral air density variations during strong planetary wave activity in the mesopause region derived from meteor radar observations, *J. Atmos. Sol.-Terr. Phys.*, 74, 55–63, <https://doi.org/10.1016/j.jastp.2011.10.007>, 2012.
- Stober, G., Matthias, V., Brown, P., and Chau, J. L.: Neutral density variation from specular meteor echo observations spanning one solar cycle, *Geophys. Res. Lett.*, 41, 6919–6925, <https://doi.org/10.1002/2014GL061273>, 2014.
- Stober, G., Matthias, V., Jacobi, C., Wilhelm, S., J., H., and Chau, J. L.: Exceptionally strong summer-like zonal wind reversal in the upper mesosphere during winter 2015/16, *Ann. Geophys.*, 35, 711–720, <https://doi.org/10.5194/angeo-35-711-2017>, 2017.
- Tomé, A., R. and Miranda, P., M. A.: Piecewise linear fitting and trend changing points of climate parameters, *Geophys. Res. Lett.*, 31, 1–4, <https://doi.org/10.1029/2003GL019100>, 2004.
- Trenberth, K., E. and Guillemot, C., J.: The total mass of the atmosphere, *J. Geophys. Res.-Atmos.*, 99, 23079–23088, <https://doi.org/10.1029/94JD02043>, 1994.
- Trenberth, K., E. and Smith, L.: The Mass of the Atmosphere: A Constraint on Global Analyses, *J. Clim.*, 18, 864–875, <https://doi.org/10.1175/JCLI-3299.1>, 2004.
- Volland, H.: Atmospheric effects on the Earth’s rotation, Proceedings of a Workshop held at the Center for Interdisciplinary Research (ZiF), in: *Earth’s Rotation from Eons to Days*, edited by: Brosche, P. and Suendermann, J., Springer-Verlag, 127–140, 1988.
- Vondrák, J. and Burša, M.: The rotation of the earth between 1955.5 and 1976.5, *Stud. Geophys. Geod.*, 21, 107–117, <https://doi.org/10.1007/BF01634821>, 1977.
- Walterscheid, R., L.: Solar Cycle effects on the upper atmosphere: Implications for Satellite Drag, *J. Spacecraft Rockets*, 26, 439–444, <https://doi.org/10.2514/3.26089>, 1989.
- Waters, J. W., Froidevaux, L., Harwood, R. S., Jarnot, R. F., Pickett, H. M., Read, W. G., Siegel, P. H., Cofield, R. E., Filipiak, M. J., Flower, D. A., Holden, J. R., Lau, G. K., Livesey, N. J., Manney, G. L., Pumphrey, H. C., Santee, M. L., Wu, D. L., Cuddy, D. T., Lay, R. R., Loo, M. S., Perun, V. S., Schwartz, M. J., Stek, P. C., Thurstans, R. P., Boyles, M. A., Chandra, K. M., Chavez, M. C., Chen, G.-S., Chudasama, B. V., Dodge, R., Fuller, R. A., Girard, M. A., Jiang, J. H., Jiang, Y., Knosp, B. W., LaBelle, R. C., Lam, J. C., Lee, K. A., Miller, D., Oswald, J. E., Patel, N. C., Pukala, D. M., Quintero, O., Scaff, D. M., Snyder, W. V., Tope, M. C., Wagner, P. A., and Walch, M. J.: The Earth observing system microwave limb sounder (EOS MLS) on the aura Satellite, *IEEE T. Geosci. Remote*, 44, 1075–1092, <https://doi.org/10.1109/TGRS.2006.873771>, 2006.

Acknowledgements

First and foremost, I would like to thank my head of department, Prof. Dr. Jorge L. Chau, who gave me the opportunity to do my PhD at the Institute of Atmospheric Physics. In the same breath, I too would like to thank my supervisor Dr. Gunter Stober, without his ideas, support and cooperation I would not have gotten this work done. Furthermore, I thank all colleagues from the IAP, especially from the radar department, for distributing to the scientific exchange, the general cooperation, and the pleasant working atmosphere. Special thank goes to my (former) colleagues Fran- cie Schmidt, Carsten Schult, Heiner Asmus, Lena Schoon, Arvid Langenbach, Svenja Sommer, Vivien Matthias, Kathrin Baumgarten, Tristan Staszak, and Jens Söder, for work and non-work related discussions, which made the time at the IAP more amusing. I also want to thank the technical staff of the radar department for build and maintain the radar systems and the IT staff for their effort. Last but not least, I have to thank the project management of the projects WaTiLa (SAW-2015-IAP-1 383) und PACOG (DFG, project no. LU1174).

Curriculum Vitae

Personal Data

- Name: Wilhelm, Sven
- Date of Birth: 09.03.1982
- Place of Birth: Berlin

Scientific career

- since 06/2014 PhD student at the Leibniz-Institut of Atmospheric Physics at the University of Rostock,
Advisor: Prof. Dr. Jorge L. Chau
- 11/2011-11/2013 Master of Science in Meteorology, Free University Berlin Master thesis: Modeling crop yield reduction due to ozone with LOTOS-EUROS,
Advisor: Prof. Dr. Peter Builtjes
- 10/2008-11/2011 Bachelor of Science in Meteorology, Free University Berlin Bachelor thesis: Auswirkung einer Methan-störung auf die Stratosphäre und das Klima - eine Studie mit dem EMAC Klima-Chemie-Modell,
Advisor: Prof. Dr. Ulrike Langematz
- 07/2001 Abitur, Paulus Praetorius Gymnasium, Bernau

Work career

- 03/2006-03/2008 Salesman for SNT Deutschland AG
- 09/2003-01/2006 Training to Salesman for office communication at Deutsche Telekom AG

List of Publications

- R. S. Lieberman, D. M. Riggan, V. Nguyen, S. E. Palo, D. E. Siskind, N. J. Mitchell, G. Stober, S. Wilhelm und N. J. Livesey, Global observations of 2 day wave coupling to the diurnal tide in a high-altitude forecast-assimilation system, *J. Geophys. Res.*, 122, 4135-4149, doi:10.1002/2016JD025144, 2017.
- G. Stober, V. Matthias, C. Jacobi, S. Wilhelm, J. Höffner und J. L. Chau, Exceptionally strong summer-like zonal wind reversal in the upper mesosphere during winter 2015/16, *Ann. Geophys.*, 35, 711-720, doi:10.5194/angeo-35-711-2017, 2017.
- S. Wilhelm, G. Stober und J. L. Chau, A comparison of 11 year mesospheric and lower thermospheric winds determined by a meteor and MF radar at 69N, *Ann. Geophys.*, 35, 893-906, doi:10.5194/angeo-35-893-2017, 2017.
- G. Stober, J. L. Chau, J. Vierinen, C. Jacobi und S. Wilhelm, Retrieving horizontally resolved wind fields using multi-static meteor radar observations, *Atmos. Meas. Tech.*, 11, 4891-4907, doi:10.5194/amt-11-4891-2018, 2018.
- S. Wilhelm, G. Stober, V. Matthias, C. Jacobi und D. J. Murphy, Connection between the length of day and wind measurements in the mesosphere and lower thermosphere at mid- and high latitudes, *Ann. Geophys.*, doi:10.5194/angeo-37-1-2019, 2019.
- S. Wilhelm, G. Stober, and P. Brown, Climatologies and long-term changes of mesospheric wind and wave measurements based on radar observations at high and mid-latitudes, *Ann. Geophys.*, <https://doi.org/10.5194/angeo-2019-51>, under review.

Erklärung über den Eigenanteil an den Manuskripten

Diese kumulative Dissertation ist eine Zusammenfassung aus insgesamt drei Veröffentlichungen, wobei Herr Wilhelm bei drei Veröffentlichungen Erstautor ist. Im Folgenden wird der Arbeitsanteil von Herrn Wilhelm an den Veröffentlichungen aufgezeigt.

In Wilhelm et al. 2017 wurde ein Vergleich zwischen zwei Radargeräten durchgeführt. Bei diesem handelt es sich einerseits um das Mittelfrequenzsystem SAURA und andererseits um ein Spiegelmeteorradar. Die hierfür verwendeten Winde wurden durch Dr. Stober entwickelt. Herr Wilhelm hat den statistischen Vergleich beider Systeme, sowie die graphische Darstellung durchgeführt. Ebenfalls wurde der Text von Herrn Wilhelm verfasst, in welchen Diskussionen mit den Co-Autoren eingehen.

In Wilhelm et al. 2019a wurden Langzeitbeobachtungen und daraus resultierend Tendenzen von Winden, Gezeiten, sowie der kinetischen Energie von Schwerewellen und planetare Wellen für die Jahre 2002 – 2018 an 3 verschiedenen Standorten untersucht. Die verwendeten Winde stammen von Dr. Stober. Die Tendenzberechnungen und die daraus resultierenden Bilder wurden in Kooperation zwischen Dr. Stober und Herrn Wilhelm erarbeitet. Der endgültige Text wurde Großteils durch Herrn Wilhelm erstellt und anschließend mithilfe der Co-Autoren diskutiert und überarbeitet.

Wilhelm et al. 2019b beinhaltet Langzeitbeobachtungen von Winden in der Mesosphäre und unteren Thermosphäre und deren Verbindung zu einer saisonalen Änderung der atmosphärischen Dichte bzw. der Fluktuation der Tageslänge. Die Idee hierfür stammt von Dr. Stober, welcher zusätzlich die erforderlichen Winddaten zur Verfügung gestellt hat. Dr. Matthias hat die aufgearbeiteten MLS Daten zur Verfügung gestellt. Die Untersuchung der Verbindung dieser Parameter, sowie der Text und die graphische Darstellung stammen von Herrn Wilhelm. Die Co-Autoren lieferten Diskussionsgrundlagen und unterstützten bei der Bearbeitung des Manuskriptes.

Selbstständigkeitserklärung

Hiermit versichere ich an Eides statt, die vorgelegte Arbeit selbstständig und ohne fremde Hilfe verfasst, keine außer den von mir angegebenen Hilfsmitteln und Quellen dazu verwendet und die den benutzten Werken inhaltlich und wörtlich entnommenen Stellen als solche kenntlich gemacht zu haben.

Die Arbeit wurde bisher weder im Inland noch im Ausland in gleicher oder ähnlicher Form einer anderen Prüfungsbehörde vorgelegt. Weiterhin erkläre ich, dass ich ein Verfahren zur Erlangung des Doktorgrades an keiner anderen wissenschaftlichen Einrichtung beantragt habe.

Kühlungsborn, den 20. Juni 2019

(Sven Wilhelm)

,